High-Peak-Power Fiber-Laser Technology for Laser-Produced-Plasma Extreme-Ultraviolet Lithography

by

Kai-Chung Hou

A dissertation submitted in partial fulfillment
of the requirements for the degree of
Doctor of Philosophy
(Electrical Engineering)
in The University of Michigan
2008

Doctoral Committee:

Associate Professor Almantas Galvanuaskas , Chair
Professor Karl M. Krushelnick
Professor Herbert G. Winful
Adjunct Associate Professor John A. Nees

Dedicated to my parents and my brother for their love, support and patience, and in the memory of my grandmother.

ACKNOWLEDGEMENTS

I never imagined that I could come so far without the generous and endless assistance of many people. It is my privilege to express my gratitude to them for helping me throughout the toughest years of my life. First, I would like to thank my academic advisor Professor Almantas Galvanauskas for being a great mentor, guide and supporter throughout my PhD studies. His passionate and persistent attitude toward the research had inspired and motivated me in my work and also helped me through many bottlenecks. His patience and understanding of my circumstances help me through many challenges I encountered. Without his academic guidance and assistance, it would have been impossible for me to complete my projects, goals, and finally my degree.

I would also like to thank my committee members, Professor Herbert Windful Professor Karl Krushelnick, and John Nees for taking time out from their busy schedules to evaluate my research work and participate in my dissertation proposal and final oral defense. Without their patience and efforts, it would not be possible for me have a chance to complete my dissertation. Special thanks to Dr. Quoquing Chang, who had been a great friend, mentor, teacher and master, assisting graciously on my research in many aspects, career, and my attitude toward life.

Many collaborated work is done in this dissertation. I would also like thank thank my many collaborators: Dr. Aghapi Mordovanakis, Dr. Bixue Hou, and John Nees for their work on the EUV target chamber, EUV spectrometer, EUV photodiode, diagnostics on the emission and analysis on the EUV emission. I can't over express my gratitude to members in th Laser Plasma Lab at the University of Central Florida: Dr. Simi George, Dr. Kazutoshi Takenoshita, and Dr. Martin Richardson for providing droplet targets, vacuum chamber, flat-flied spectrometer and Flying Circus II EUV photodiode and their work on the above mentioned apparatus, the calibration on EUV spectrometer and the of the EUV conversion efficiency.

Special thanks to Dr. Bruno Lafontaine of AMD, who had been a great supporter for all our EUV projects and provided me assistance and career guidance. None of the EUV work could be realized without his generosity and belief in us. I would also like to thank M. Craig Swan, Dr. Guoqing Chang, Matt Rever, and Shaw Lacy for their rigorous efforts on helping me on the writing of this dissertation and proof-reading the draft of this dissertation.

I was honored to work with so many talented and skilled group members: M. Craig Swan, Dr. Kai-Hsiu Liao, Dr. Guoching Chang, Xiuquan Ma, Dr. Chi-Hung Liu, Dr. Ming-Yuan Cheng, and Dr. Shenghong Huang. I would also like to thank all my friends in Michigan: Gilda Kao, Kaai Liao, Chia-Fei Kao, Nei-Moe Hou, Shao-Ning Yu, Yi-Hao Chen, Hsun-Yi Chen, Hsien-Kai Hsiao, Nai-Kuan Yang, Jamie Wu, Andy Tsai and many many others. It's hard to picture how I would have survived all the cold winters without their warm friendships.

Finally, I want to express my deepest gratitude to my parents and brother. You gave me the hope and support that took me through all the difficulties in my life. None of my work could have been completed without your endless love and patience.

TABLE OF CONTENTS

CHAPTER

LIST OF TABLES

Table

LIST OF FIGURES

<u>**Figure**</u>

CHAPTER I

Introduction

Demands on light sources in the extreme-ultraviolet (EUV) and the soft-X-ray region have been growing in recent years due to potential applications on element-specific spectroscopy, high-resolution microscopy, and surface analysis [4]. The relative transparency of the "water window" in the soft-X-ray region enable solutions for high-resolution imaging in biological and medical sciences[5]. Moreover, the search for a high power light source at shorter wavelengths for the next-generation of lithography steppers is the main driving force to the rapid development of a EUV light source in recent years [6, 7, 8, 9, 10].

1.1 Lithography: the Driving Force for the Semiconductor Technology

Stimulated by increasing demands on computation power and dense storage, progressive development in the lithography steppers stimulated the manufacturing technology in the semiconductor industry. The Moore's Law predicts that number of devices on a chip doubles every 18 months. In other words, logarithmic growth occurs in the process speed and memory size as shown in Figure 1.1. In order to keep up this growth rate, the critical dimensions for use in high-volume manufacturing are anticipated to decrease on a schedule of 0.71× reductions every three years [11].

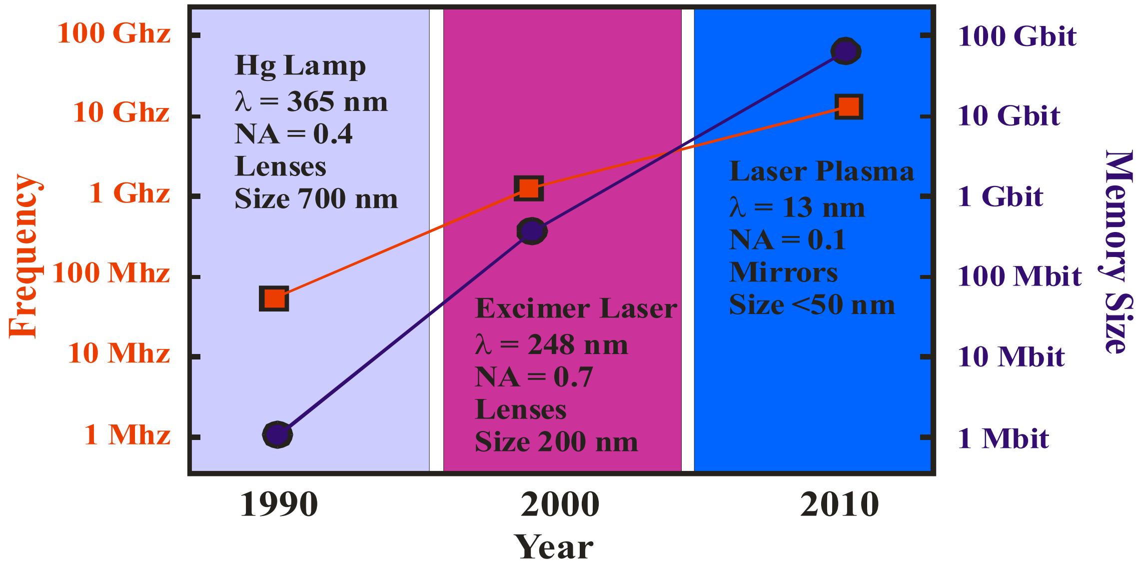

Figure 1.1: Over the last few decades, the demand on powerful computing and dense storage required a new generation of lithography stepper using much shorter wavelength.

Resolution (RES) of critical dimension can be related to the other parameters of exposure tools by,

$$RES = K_1 \frac{\lambda}{N.A.} \tag{1.1}$$

where the constant K_1 is determined empirically by the resist and the etching process during the manufacturing of integrated circuits [12], typically in the range from 0.4 to 0.8 [13], λ is the wavelength of the light source and NA is the numerical aperture typically in the range from 0.2 to 0.8 [13]. Equation 1.1 predicts that one can improve the resolution of critical dimension by choosing a shorter wavelength source (smaller λ), improvement in projection optics (higher NA), and control on process and better contrast resist (lower K_1).

However, higher NA precipitates more stringent requirements on the manufacturing processes as another associate parameter, depth of focus (DOF), which is given by,

$$DOF = \frac{K_2\lambda}{(NA)^2} \tag{1.2}$$

where K_2 is also empirically determined. DOF gives a longitudinal measure of the distance over which the image is in proper focus and shows that an increase in NA will decrease DOF. This will lead to decrease in the process window, requiring constant monitoring. Finer adjustment of the final lens-to-wafer separation is also required in order to maintain highest resolution.

One of the major advancements in the higher-resolution lithography was driven by the decreasing wavelength in light source as shown in Figure 1.1 In the early 1980's to mid 1990's, the lithography tools utilized mercury (Hg) arc lamps, filtered for different spectral lines (g-lines at 435 nm and i-line at 365 nm) [13]. In the early 1990's, excimer laser sources with wavelength at 248-nm krypton fluoride (KrF) and 193-nm argon fluoride (ArF) took over and remain the leading light sources for high volume manufacturing (HVM) lithography stepper to date. In addition to shorter wavelength, excimer laser sources also have much narrower line-widths than the mercury emission band at 248nm, which is beneficial for controlling chromatic aberrations in the largely refractive optics.

During the early days in lithography technologies, it was believed that the physical limitation of the smallest feature size reachable by a certain light source is one half of the wavelength [10], nonetheless, recent advancement on immersion lithography (reduce the smallest feature by a large index fluid), high contrast resists and optical proximity effect correction [14] had pushed the smallest feature size to a 45nm node using a 193-nm ArF laser(less than one-fourth of the wavelength of the ArF excimer laser)

However, for a process beyond 32-nm pitch, 193-nm water immersion process is limited by NA to resolve this pitch, unless narrow pitches are split into larger ones by double pattering or exposure, corresponding to a doubled manufacturing cost [11].

1.2 Beyond 193-nm Lithography

Alternative lithography technologies using different light sources that had been developed over the years includes 157-nm (F_2) optical lithography [15, 8, 16, 17] X-ray proximity printing (XPL) [18, 8, 19], electron beam projection techniques (EPL) [18, 7], ion beam writing [18, 7, 8], nanoimprinting [20, 7, 21, 22], and extreme ultraviolet lithography (EUVL) [7, 8, 9] based on multilayer coated reflective optics.

The issues of concern for 157-nm optical lithography are the availability of viable resist and the absorption of SiO_2. The optics has to be made from CaF_2, which projects the cost to be doubled in projection optics. However, the predominant reason for the discontinuation of 157-nm optical-lithography program is the extension of 193-nm optical-lithography with immersion and the fact that EUV lithography will likely to be ready as the successor of 193-nm process.

X-ray proximity lithography (XPL) is a relatively mature technology compared to optical lithography which utilizes nominal 0.7 nm to 1.2 nm wavelength radiation (1.0 keV to 1.8 keV photon energy) from relatively broadband-bending-magnet synchrotron-radiation with relatively simple beamline optics [19]. However, XPL is an 1:1 imaging lithography (compared to 1:4 reduction optics used in optical lithography, including EUV lithography) and the improvement in UV and DUV optical-lithography had postponed the need for this type of post-optical advanced lithography.

Electron projection lithography (EPL) suffers from mask heating and subsequent overlay errors which prevents EPL from being widely used. Instead, it is now generally used to fabricate the mask for DUV or EUV lithography.

Nano-imprinting (NIP) replicates the pattern on the substrate from a master pattern by molding or stamping, which is similar to the current process replicating compact discs [20, 7, 21, 22]. A feature size smaller than 10 nm has been obtained using nanoimprinting, however, the cost of such a method is much higher than using EUV lithography, due to the expensive master pattern and high requirement of level-to-level alignment accuracy (typically one-third of the minimum feature size)

By the year of 2003, work on proximity x-ray lithography, electron projection lithography and ion projection lithography was either completely terminated or greatly reduced. Development of EUV lithography is a relatively late-comer among the possible candidates for next generation lithography, yet, EUV is the leading technology promising the high throughput and cost effective solution as the next generation of lithography steppers.

1.3 Extreme Ultraviolet as the Source for Next Generation Lithography

The efficient high-power EUV light source is presently considered a strong contender for high-volume semiconductor manufacturing at the 32-nm node around 2010-2013. One important physical limitation on shorter wavelengths is that the optical materials and approximate transmission limit of fused silica (pure SiO_2) is around 200 nm and transmission optics will no longer be efficient in the vacuum ultraviolet (VUV) region where air and all materials become absorbing. Therefore, reflective optics using multilayer mirrors become the optics-of-choice for wavelengths shorter than 200 nm where a vacuum environment will be required for EUV lithography.

1.3.1 Mo/Si Multilayer Mirrors: the Key Enabling Technology for EUV Lithography

EUV lithography will not be realized without the invention of Mo/Si multilayer interference mirrors. A multilayer interference mirror, typically consists of two materials of high and low atomic number (Z) in order to maximize the difference in electron density. Mo (molybdenum, Z=42) / Si (silicon, Z=14) and Mo/Be (beryllium, Z=4) multilayer, first perfected by Barbee, achieve reflectivity of the order of 70 % . The coatings of these multilayer mirrors are largely amorphous typically on a Si substrate and reflection conforms to Bragg's law for a periodicity equal to the thickness of one bilayer pair in the order of few nm (or tens of atomic mono layers).

Spectral bandpass is in the order of 1/N, where N is the number of layer pairs and is typically between 30 and 50 for high reflectivity. For normal incidence reflection filters, individual filters are each about $\lambda/4$ thick, or in the order of few nanometers. Off-normal incidence can be made possible by changing the thickness of layers according to Bragg's Law,

$$d = \lambda/2 sin\delta \tag{1.3}$$

One great advantage of multilayer coating is its adaptability to curved surfaces, enabling their use on complex designs of collector optics.

1.3.2 Advantages of EUV Lithography

The solution using a EUV light source provides significant reduction in wavelength (11-13nm for EUV versus 193-248nm for DUV), allowing for a small feature-size ($\approx$ tens of nm) with a relatively smaller numerical aperture and large depth-of-focus. Additional advantages include:

1. EUVL is an optical lithography to which all the experiences learned by the semiconductor industry on previous exposure tools can still be applied.

Type of lithography	Extreme Ultraviolet	ArF DUV
Wavelength	$\lambda = 13.5nm$	$\lambda = 193nm$
Collector optics	reflective optics	refractive optics
Reticles	reflective	transmitting
Environment	vacuum environment	nitrogen purged environment

Table 1.1: Major differences between EUV and 193 nm Lithography

2. It is expendable due to the $\approx$ 15 times reduction in the wavelength. With a conservative estimation of K_1=0.4 and NA=0.25, it can already pattern 22-nm half-pitch features.

3. PXL and nanoimprint suffers from an inability to fabricate an accurate reticle with the same feature size as the final pattern, while EUV lithography is also a reduction technology where the reticles are 4× larger than the final pattern.

4. Fabrication for the membrane reticle used in PXL, IPL, EPL have proved to be challenging while a rigid, low-thermal-expansion glass reticle can still be applied to EUV.

5. Cost of ownership is comparable to 193nm immersion lithography, and has the potential to be lower [23].

6. Due to the much shorter wavelength, EUV masks are likely to be less complex than 193-nm masks.

Table 1.1 shows the major differences between EUV and 193 nm lithography.

However, one of the most difficult challenges remains to be the development of a high power feasible EUV source, along with finding the suitable resist and development of the efficient collector.

Wavelength	13.5 nm
In-band EUV Power at IF	180 W
Repetition Frequency	>7 kHz
Integrated Energy Stability	$\pm 0.3\%, 3\sigma$ over 50 pulses
Source cleanliness	$\geqslant$ 30,000 hours
Etendue of Source Output	max 1-3.3 mm^2sr
Spectral Purity	
130-400[nm](DUV/UV)	$\leqslant$ 7.5% (Design dependent)
$\geqslant$ 400 nm (IR Vis) at Wafer	$\leqslant$ 0.1% (Design dependent)

Table 1.2: Joint requirement of light sources for EUV lithography by ASML, Canon, Nikon

1.3.3 Requirements and Development of EUV Light Source

The initial production of semiconductor chips using EUV lithography is targeted for the year 2009 at a 32-nm half-pitch resolution. In order to expose 100 wafers per hour, the power required at the intermediate focus is 180 W for the first generation of the production tool. The joint requirement by the semiconductor tool manufacturers for the EUV source is summarized in Table 1.2

EUV radiation can be produced by an electromagnetic pinch (discharge produced plasma source or DPP source) or by laser heating (laser-produced plasma source or LPP source). However, due to the intrinsic differences between DPP and LPP sources, the source power required for DPP and LPP differs significantly. DPP generally has a larger source size, meaning a lower brightness that allows a smaller collector angle. Moreover, the debris generated from a current DPP source is not as controllable as that from an LPP source, therefore, a more sophisticated debris mitigation scheme must be applied to DPP sources to maintain the collector lifetime as stated in Table 1.2. Table 1.3 summarized the estimated required powers for

Source Type	Discharge Produced Plasma(DPP)	Laser Produced Plasma(LPP)
Required EUV Power at intermediate focus (IF)	180 W	180 W
Collector solid Angle (sr.)	π	2π
Integral Reflectivity of Collector	55%	50%
Gas Absorption	10%	10%
Debris mitigation transmission	90%	100%
Spectral Purity Filter	90%	90%
Required EUV at source	898W	444W

Table 1.3: The power requirement at the source extracted from the different collector requirement for laser produced plasma (LPP) and discharge produced plasma (DPP)

the commercialized lithography stepper using the DPP and the LPP sources. DPP sources, conclusively, require approximately twice the EUV power at the source than LPP source.

DPP had been leading the power-source race and was once considered the only solution for the production-worthy EUV source until recent years. However, recent developments on kilowatt-class high-average-power lasers has significantly improved the power of LPP sources surpassing the power of DPP sources[24]. Moreover, LPP source in general generated less debris compared to DPP sources. In addition, being a much bright source, i.e. better collection efficiency, LPP had become the preferred source for the HVM EUV lithography tools. On the other hand, uncontrollable debris from the DPP sources made them almost infeasible as a realistic source, leading to a great slowdown on their development.

1.4 Laser-Produced-Plasma Source: Current Status and Requirements on Laser Pulse Parameters

The current status of LPP EUV sources is summarized as follows:

4W of in-band EUV power at the source was demonstrated using a Xe-jet target and a 1-kW Nd-YAG laser with a 10-kHz pulse repetition rate, 100-mJ pulse energies and 6-ns pulse duration. The conversion efficiency is 0.4% [25]. With Sn-droplet targets, the state of the art CO_2 laser with 12kW of laser power demonstrated 100 W of power in the burst mode (5% of duty cycle demonstrated so far) calculated at IF (5W average at IF for an open-loop operation). Another 6-kW CO_2 laser also demonstrated 16 W of EUV power at IF with 1-sr collector using a rotating Sn-plate [26]. Richardson *etal.* demonstrated 24 W of in-band EUV power at the source, projecting 8W of power at the IF with a continuous operation using Sn-doped water-droplet targets and a Nd:YAG solid-state laser. To summarize, a production-worthy power level should not be unreasonable to imagine in the near future with the progressive development of high-power lasers to the required power level.

In addition to the power requirement, the laser must provide the correct pulse parameters to have efficient EUV generations. Several studies [2, 27, 28, 29, 30, 31, 32, 33] on conversion efficiency optimization using ns-pulsed solid-state lasers reported that the highest conversion efficiencies can be achieved at the intensities of $0.5 - 5 \times 10^{11} W/cm^2$ using the 1064-nm lasers and Sn or Sn-composite target materials. Several laser parameter sets for the Nd:YAG solid-state laser used to achieve high EUV conversion efficiencies with Sn or Sn-composite targets [2, 27, 28, 29, 30, 31, 32, 33] are provided in Table 1.4.

Solid-state lasers capable of efficient EUV generation have pulse durations of several nanoseconds and energies exceeding 100 mJ, corresponding to multi-megawatt peak powers (Table 1.4). Such pulse energies, however, pose a significant problem for fiber lasers, which have not achieved 100-mJ pulses at such pulse durations due to the relatively small transverse mode size of fiber gain media. Consequently, a strategy of

Ref.	Target	Pulse Duration	Highest Pulse Energy Available	Intensity for highest CE	Best CE
[29]	Liquid Sn-jet	5 ns	284 mJ	$5 \times 10^{11} W/cm^2$	2.5%
[30]	Solid Sn	8 ns	1 J	$5 \times 10^{10} W/cm^2$	2.0%
[31]	Solid Sn	1.2, 2.3, 5.6, and 8.5 ns	Not stated	$5 \times 10^{10} W/cm^2$to $1 \times 10^{11} W/cm^2$	2.2%
[32]	Low density Sn	10 ns	Not stated	$5 \times 10^{10} W/cm^2$	2.2%
[2]	Tin-doped droplet	11.5 ns	1.6 J	1-1.5$\times 10^{11} W/cm^2$	2.0%
[27]	Solid Sn	10.5 ns	200 mJ	$9.2 \times 10^{10} W/cm^2$	4.9%
[33]	Tin	7 ns	650 mJ	$4 \times 10^{10} W/cm^2$to $1 \times 10^{11} W/cm^2$	2.0%

Table 1.4: Laser parameters of solid state laser that demonstrated high conversion efficiency using Sn-based target materials

utilizing a fiber laser for efficient EUV generation should be distinctly different than using other types of lasers, since the operational-parameter space accessible with a fiber laser is very different from that of the solid-state laser shown in Table 1.4. One path toward achieving the required intensities with a fiber laser would be to exploit the facts that : (i) fiber lasers can provide much shorter pulses and near-diffraction-limited beam qualities and (ii) key parameters of the pulses (such as duration, shape and repetition rate) can be electronically controlled [34] with the diode-seeded fiber-amplifiers. Nonetheless, it is necessary to design a fiber laser providing the correct laser parameter space and also have enough power for a production-worthy EUV source. Using the required power at the source (Table 1.3) and the demonstrated modal efficiency of $\approx 2\%$ (Table 1.4), the required laser power is ≈ 25 kW.

1.5 25-kW High-Power All-Fiber-Laser Architecture by Spectral and Spatial Combining

The high-power pulsed-fiber-lasers have a significant potential as the cost-effective multi-kW power-scalable laser drivers for high-power laser-produced-plasma EUV lithography sources. However, two questions have not yet been investigated. (i) Given that the pulse parameter space is very different from that of solid-state lasers, can the pulsed fiber-lasers provide irradiation conditions suitable for efficient EUV generation? (ii) Is current fiber laser technology suitable to provide enough power required for high volume manufacturing?

1.5.1 Introduction to the Fiber Laser: A Compact, Robust, and Efficient Laser

Fiber lasers, first demonstrated by Snitzer [35], have significant technological advancements over the last few decades in several types of rare-earth doping materials such as Nd [36], Sr [37], Pr [38], Er [36, 39, 40, 41], Yb [42], Tm [43]. While the diode-pumped solid-states (DPSS) laser suffer from thermal-optical problems (thermal lensing and thermally stress-induced birefringence), the fiber laser exhibits much higher thermal management properties due to its larger surface-to-active-volume ratio [44]. Therefore, the beam quality of the fiber-laser output is dominated by the physical design of the fiber itself and the degradation due to thermal distortion as seen in DPSS is negligible. Another attractive feature of the fiber laser is its very high efficiency; up to 80% of optical-to-optical efficiencies can be achieved for Yb-doped amplifiers due to its very small quantum defect ($< 10\%$). Pumped with a highly efficient diode laser, the wall-plug efficiency of the fiber laser system can generally reach $\approx 40\%$, while gas lasers can only provide $\approx 10\%$ of efficiency.

Fiber lasers can also emit a broad range of wavelengths from 1064nm to $2\mu m$ depending on the dopant-of-choice and the typical operation wavelengths are 1064nm (Yb), 1550 (Er), and 2000nm (Tm) Among the dopant, the inherently high quantum efficiency of Yb^{3+} is also the reason that fiber-lasers with the highest power are doped with Yb^{3+}. Generally, the single-mode fiber lasers used in the telecoms system, with very robust mode quality and well-developed technologies for making it a compact system, have a core diameter of $\approx 10\mu m$. However, two major trade offs will accompany smaller core size. Core-pumped single mode diodes are limited to a power level of several watts, which in turn limits the maximum power that can be extracted from the fiber. Moreover, the small transverse core size also indicates lower nonlinearity thresholds, which limits the maximum output power, especially when operated in the pulsed mode.

The solution to this is the use of double-cladded LMA fibers [45]. The first cladding has a lower refractive index than the core, therefore guiding the electromagnetic wave, based on total internal reflection. The second cladding, usually made of polymer (for LMA fiber) or air-holes (for PCF fibers) [46, 47], surrounds the first cladding (also referred as "‘pump core"’) to guide the pump light. This geometry will increase the signal core size and also increase the pump power that can be coupled into the fiber with the diode lasers with same brightness.

The double-cladded design of the fiber has a very attractive performance of effective brightness improvement. This is the highly multimode pump light being absorbed gradually and completely over the entire length of the amplifier and the energy is transferred into high-brightness, high-power radiation guided by the core. The relatively long interaction length (usually in the range of several meters depending on the doping level and pump-cladding to core-area ratio) and smaller transverse core size makes the fiber laser more susceptible to nonlinear effects such as stimulated Raman-scattering (SRS), self-phase modulation (SPM), stimulated Brillouin scattering (SBS) and four-wave mixing (FWM). These nonlinear effects are beneficial in some applications, (eg. super continuum generation, nonlinear spectral broadening in fiber chirp pulse amplifier (FCPA) system, and in Raman amplifiers). However, for high average-power and high peak-power extraction as well as some applications requiring narrow linewidth (eg. laser ranging, LIDAR and spectral beam combining), nonlinear effects are generally detrimental and it is necessary to take into account these nonlinear effects while designing the fiber laser based system.

The powers from the CW fiber lasers with a diffraction-limited output beam in the last 15 years increased nearly three orders of magnitude from 5W to 3kW [48, 49, 50, 51, 52, 53, 54, 55, 56]. In addition, fiber core-size scaling is currently being pursued through several innovative approaches [57, 58, 59], which are likely to extend current capabilities of fiber laser technology much further. These approaches effectively provide single-mode output from the fiber with core size and numerical aperture beyond the waveguide criteria, by introducing additional structure around the core to increase the loss of higher order mode, through coupling the HOM into the side structures. Realization of these technologies,high power fiber lasers can be packaged into monolithic systems, to provide a robust, alignment-free, compact system for industrial, military, and medical applications.

1.5.2 Power Scaling Strategy for the 25-kW Fiber Laser EUV Driver

Although the single-beam continuous-wave fiber-laser has reached a power level of several kWs, the fundamental limitation on the output powers are quite different between continuous-wave (CW) and pulsed fiber lasers. For CW operation, the primary limitation was the nonlinearity of SBS (for narrow-linewidth output) and SRS (for broader linewidth output). Other limitation includes the heat generation from quantum defect and non-radiative recombination of the excited state of gain dopant. The length of the CW fiber-lasers is usually a few tens-of-meters for complete absorption of the pump light and to maximize surface area required by an optimal heat dissipation. However, for a high-peak-power pulsed-fiber-laser, the design strategy is considerably different from that of the continuous-mode operation.

Since nonlinearity is the major limitation of peak power extraction, the length of the gain fiber has to be as short as possible to minimize the nonlinear interaction length. For the desired high energy and peak power extraction required for efficient EUV generation the length of the active fiber is usually limited to 1-3 meters even with the use of large-mode-area fibers.

Moreover, considering the the highest operational rate for a current target dispenser ($\sim$ 100 kHz) and the energy per pulse from the fiber to several mJs, (due to the limited extractable energy from a fiber laser and nonlinear effect), the highest power that can be realized from a single fiber laser channel is of $\approx$ 500 W. Therefore, a combining scheme is necessary to reach the laser power requirement of 25kW.

We proposed a high-power fiber-laser architecture utilizing two types of combining: spectral beam combining and spatial beam overlapping (Figure 1.2). The system architecture can be divided into three layers:

1. The basic building block: a single-emitter fiber integrated module (SEFIM) that can provide laser pulses with 1 to 10-ns durations, 6-mJ of energy and 500-W of average power at a repetition rate of 83 kHz.

2. Spectrally combined modules (SCM) consist of ten SEFIM's spectrally combined modules (SCM) with wavelength-selective combining elements into one laser beam with average power 5 kW.

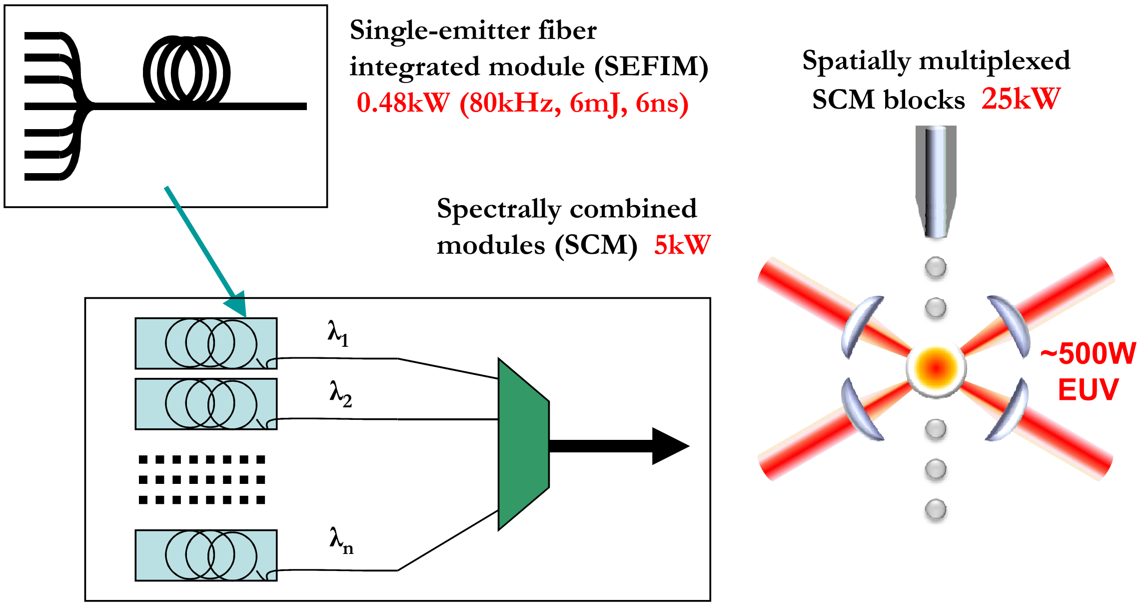

Figure 1.2: Power scaling strategy to reach required laser power for EUV generation. Spectral and spatial multiplexing enables fiber laser to reach the power level beyond that available from a single channel emitter.

3. Spatial multiplexer: five SCM's from different beam lines are focused on to the same focal spot on either the same or the consequent targets. Up to 25 kW of laser power will be available to the laser-produced plasma source. With $\sim$ 2% of conversion efficiency, this laser power will give $\sim$ 500 W of in-band EUV power at the plasma source.

Spectral combining multiplexes the laser beams of different wavelengths using wavelength selective components such as diffraction gratings, volume Bragg gratings, prisms, and multilayer dielectric thin-film filters. The challenge for spectral combining is to provide a compact, robust and efficient scheme that can handle up to hundreds mJ's of nanosecond pulses and several kW of average power simultaneously on the combining elements.

For the spatial overlapping, it is a comparatively straight-forward type of multiplexing scheme (Figure 1.3). The major challenge on the spatial overlapping is to maintain good control on the laser output pointing stability as well as the synchronization of the laser focal spot and target both temporally and spatially. This type of multiplexing in EUV generation was already demonstrated using two high-power solid-state Nd:YAG lasers on the droplet targets by Richardson *et al*. [60].

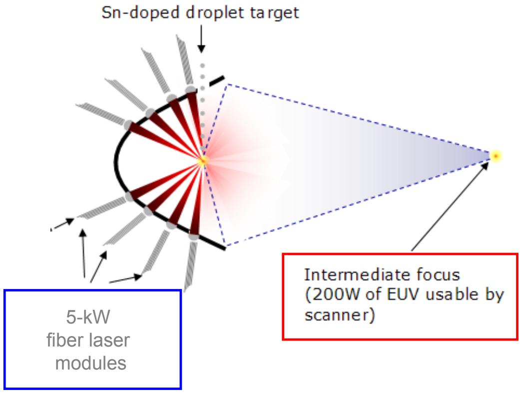

Figure 1.3: Spatial multiplexing shows the relative position of the fiber laser beam, target and the collector optics.

1.6 Chapter Overview

This dissertation is organized as follows: Chapter II is dedicated to the development of SEFIM as the EUV driver as discussed in Section 1.5.2. The analysis on the design requirements to reach the optimum intensity, given by the mode quality and the peak power/energy of the laser, will be carried out in detail. The laser parameters considering the limitations on nonlinearity and saturation will also be discussed. The improvement of the system configuration including the implementation of the arbitrary waveform generator (AWG) to control the pulse shape and arbitrary prepulse can not only compensate the amplifier gain saturation, but also can provide an instrumental tool for plasma the dynamics study. A record high peak power of 6 MW was achieved by seeding with a gain-switched 100-ps pulse from a Fabry-Perot diode. A high energy of 6 mJ with a pulse duration of 6 ns, giving a peak power of 1 MW, is generated with AWG preshaping. High average power up to 140W was also achieved by actively cooling the fiber-end and packing the fiber in thermally conductive materials.

Chapter III is devoted to two experiments of fiber-laser-produced-plasma (FLPP) EUV generation. The first one is a proof-of-principle experimental demonstration using a solid-Sn target. Prior to this experimental validation, EUV generation was not believed to be possible using the fiber laser due to its relatively small extractable energy. This demonstration is, to the best of our knowledge, the very first 13.5-nm EUV generation using a fiber laser. We achieved $\approx$ 1% conversion efficiency at a repetition rate of 50 Hz [61]. The conversion efficiency was limited by the highest available on-target intensity of $1 \times 10^{10} W/cm^2$ at the time. Higher conversion efficiencies can be expected with the improved laser intensity (Table 1.4). With the improved mode quality and the peak power from the $80\mu m$ fiber amplifier, as described in Chapter II, a higher intensity is achievable with a much smaller focusable spot size. The use of solid-Sn target merely served the purpose for the validating fiber laser as a suitable EUV driver. A realistic target with less debris generated and compatibility of higher repetition rate is the only solution to a practical LPP source. For this reason, the target-of-choice had changed to effectively-debris-free Sn-doped water-droplet targets developed by the University of Central Florida, to demonstrate a scalable and debris-free fiber-laser-driven EUV lithography source. With the help of the pulse-shaping capability of the laser system, $\approx$ 2.1% of conversion efficiency is demonstrated, resembling the CE demonstrated by the solid-state lasers with very different laser parameters as detailed in Table 1.4. Conversion efficiency is also shown to have a close dependence on the main pulse durations and prepulse parameters. This successful demonstration of efficient EUV generation indicates that the fiber laser is a feasible laser-driver-candidate for the next generation of lithography tools. The concept of the SEFIM as described in Section 1.5.2 is also realized with the successful demonstration of the efficient EUV generations.

Chapter IV of the dissertation describes a novel spectral combining scheme using non-spatial dispersive combining elements. This proposed combining scheme uses multilayer-dielectric filters as the beam-combining elements, giving no limitation on the polarization state and the line width on the laser. This is beneficial for combining fiber lasers with MW-level peak-powers, as required for efficient EUV generation. An experimental demonstration with three fiber-laser channels showed an overall combining efficiency $> 92\%$ at pulsed operation. 52 W of combined power is demonstrated at a repetition rate of 100 kHz in the high average-power demonstration. 4mJ of combined energies with a peak power ≈ 0.9 MW is achieved at a repetition rate of 1 kHz in the study of high-energy combining. This novel combining scheme enables high-average-power spectral-combining and provides a feasible solution to a 25-kW all-fiber-laser-based EUV source for the next generation of lithography steppers.

CHAPTER II

High-peak-power, high-average-power pulsed-fiber-laser EUV driver development

Aforementioned in Section 1.5.2, the basic building block of the fiber-laser-based EUV source is the Single Emitter Fiber Integrated Module (SEFIM). In this chapter, the design of the SEFIM for an efficient high power EUV generation will be discussed, supplementing the experimental performances and also the numerical design parameters. We begin with the design requirement of the fiber laser system and the selection of the core to reach the laser parameters for an efficient EUV generation in the Section 2.1 and 2.2.

Section 2.3 to 2.7 will describe the details of the system design, system performances, the nonlinear limitations on the peak power extraction, providing experimental results and numerical simulations. A numerical analysis and the experimental study on energy extraction, a thermal management design and the average power optimization of the system will also be given. Using the record-high peak-power with the diffraction-limited mode-quality, an experiment of atmospheric gas breakdown will also be discussed briefly in Section 2.6.4.

2.1 EUV Fiber Laser Design Criteria

Over the years, Sn or Sn-composite targets have been demonstrated to be the most efficient EUV target materials [2, 27, 28, 29, 30, 31, 32, 33]. Due to the differences in laser parameters, target formation, focusing condition and experiment apparatus, irradiation conditions (laser energy, pulse duration, intensity, focal spot size on target) at which the highest conversion efficiencies are reached differ among all experiments. However, for the optimal efficiency, a general trend exists for the reported intensities to be in the range of $0.5 - 5 \times 10^{11} W/cm^2$ and pulse durations between 1.2 ns to 11.5 ns. Reported target spot sizes though have a much larger range of variation from $17\mu m$ to $500\mu m$.

Consequently, the first guideline of designing a fiber laser system for EUV generation study is to achieve these intensity with 1-10ns pulses. Since the energy available from a nanosecond pulse fiber laser is limited, a sufficiently small focal spot size has to be used. Furthermore, it is important to match the laser beam focus and the target size to better utilize most of the target materials and to reduce the generated debris. Due to the relatively smaller energy available from the fiber laser in the nanosecond pulse duration, smaller focal spot size in the range of 20 - 30 μm become necessary to reach the intensity. Therefore, simple calculation indicates that more than 1MW peak power in 1-10ns pulses focused to 20 - 30 μm spot should produce the optimum intensities. These spot size are compatible with existing Sn-droplet plasma sources. Additionally, although efficient EUV generation is not much dependent on beam quality, beams with $M^2 \leq 2$ are desirable in order to place the focusing optics at a sufficient distance to mitigate laser-plasma debris contamination.

In addition to the requirement of the peak power and the mode quality of the laser beam, finding an optimized condition for efficient EUV-generation within fiber-laser parameter space requires controlling a wide range of pulse durations and energy levels. A diode-seeded fiber laser amplifier provides the potential of the temporal pulse-shape manipulation and the pre-pulses generation, providing a useful tool for plasma dynamics study.

2.2 Fiber Core Size Selection

Choice of fiber core size is determinative to provide both sufficient mode quality and peak power to reach the required intensity for efficient EUV generation. A larger-core fiber in general provides more extractable energy due to its higher saturation energy, however, at the expense of mode quality degradation. A good compromise has to be balanced while choosing the core size in order to meet both peak power and mode quality requirements. One way to increase peak power is to have higher extractable energy which is limited by the saturation energy of the fiber. For Yb^{3+}-doped fiber, the saturation fluence is 0.66 $\mu J/\mu m^2$ at 1064 nm [62].

As shown in Figure 2.1, the saturation energy scales with the mode area and the maximum extractable energy from an amplifier given by [63].

$$E_{avail} = E_{sat} \times \ln G_0 \tag{2.1}$$

where E_{sat} is the saturation energy and G_0 is the small signal gain. In order to extract several mJs of energy, saturation energy should exceed 1-mJ, giving the required mode field diameter larger than 44-μm (or a core diameter exceeding 58-μm for step index fiber with 0.06-NA cores). It is also important to keep in mind that amplifying beyond the saturation energy will come with a cost of pulse temporal deformation and a significantly lower saturated gain due to the population inversion draining in the gain medium (Section 2.6).

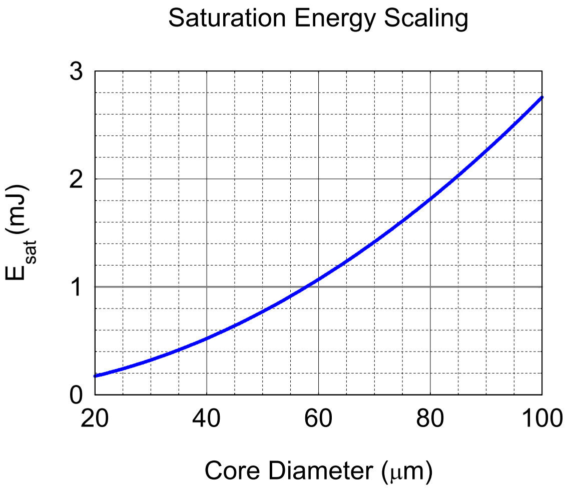

Figure 2.1: Scaling of saturation energy with fiber core size for a 0.06 core NA.

Another limitation of the peak power from a fiber laser is imposed by the bulk damage threshold of fused silica, which for a given fluence scales as the inverse square root of pulse duration. Taking the experimentally measured bulk damage threshold of 800 J/cm^2 for 6.2-ns pulses in the Yb^{3+}-doped fiber [64], Figure 2.2 plots the scaling of the peak-power-damage thresholds for three different pulse durations. The core size sustainable of a 1-MW peak power at 5 ns has to be larger than 38-μm in diameter. In practice, the fiber core size should be chosen to sustain at least twice of the damage fluence in order to avoid catastrophic failure.

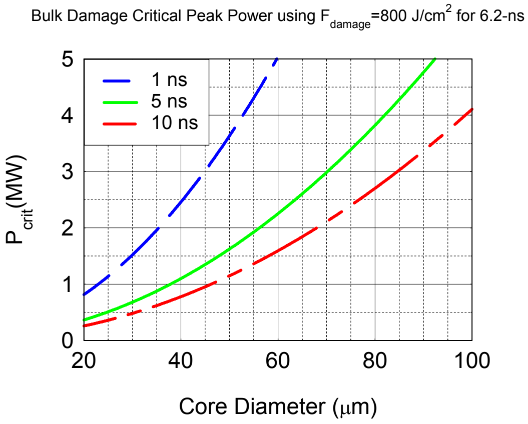

Figure 2.2: Critical peak power for fused silica bulk damage threshold for different core sizes with 0.06 core NA.

In addition to the peak power, the other requirement to reach the required intensity is the mode quality of output laser beam. In large-core conventional fibers, the achievable mode quality depends on the modal separation between the fundamental mode and the next higher order mode supported in the fiber and is characterized by the mode scattering coefficient. Detailed discussions will be given in Section 2.4. Based on our experiences on different large-mode-area fibers with core diameters of 50 μm, 65 μm, 80 μm, 115 μm 140 μm and 200 μm [65, 66, 61, 34, 67], the core diameters of the fiber that could be operating close to single transverse mode are in between 50 and 80 μm, with proper care in preparation and operation. Considering the above outlined analysis, the 80-μm core fiber appears to be the suitable choice as the largest core with sufficient beam quality.

It is important to keep in mind that the above mode consideration only applies to conventional step-index LMA fibers while development of novel fiber structure design can provide effectively single-mode LMA output [59] and the mode quality will not be limited by core size. The use of the conventional fiber is merely due to availability and to explore the mode size required for such high peak power and energy.

2.3 Pulsed Fiber Laser System

This 80-μm-core fiber was used as the last stage amplifier in a four-stage Master Oscillator Power Amplifier (MOPA) Yb-doped fiber experimental system (Figure 2.3). The system starts with an electric-pulse-driven Fabry-Perot semiconductor laser diode emitting at 1064 nm. Such a scheme enables versatile selections of the repetition rate, pulse duration and pulse shape.

The seed pulse is pre-amplified to peak power levels ≥ 1 kW by two stages of all monolithic, single-mode, polarization maintaining fiber amplifiers, pumped with the

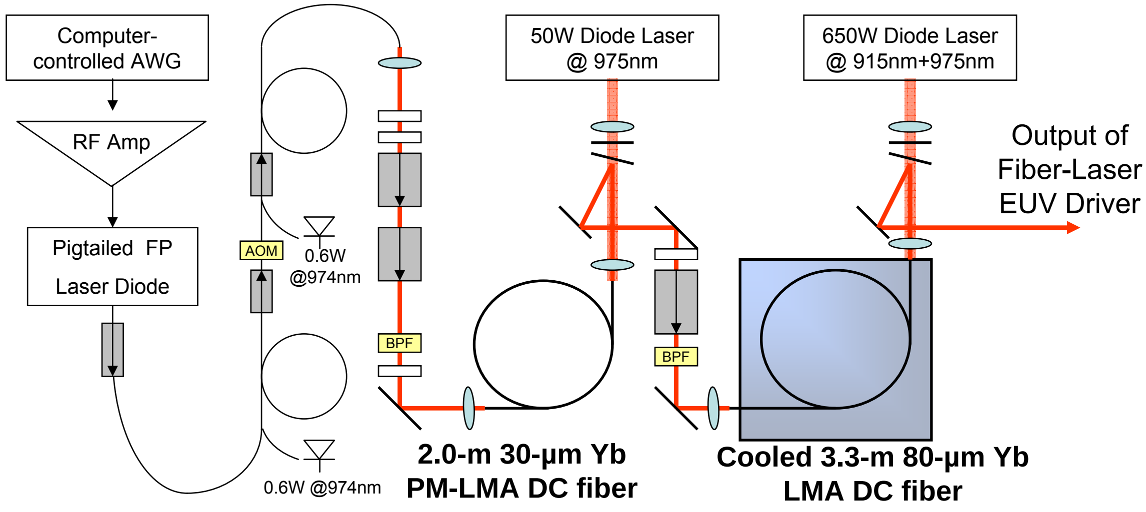

Figure 2.3: Configuration of our experimental high average power pulsed fiber laser system with Fabry-Perot (FP) diode seed. Two stages of monolithic single-mode fiber amplifier amplify the seed to kilowatt peak power level. Further amplification by two stages of large mode area (LMA) power amplifiers generates >MW peak power of nanosecond pulses with excellent beam quality close to single transverse mode.

600-mW telecom-graded single-mode laser diodes at 974 nm. In order to amplify the peak power beyond the level achievable by a standard single-mode fiber (Figure 2.4 (a)), it is necessary to use large-mode-area (LMA) fibers in the power amplifiers (Figure 2.4(b)).

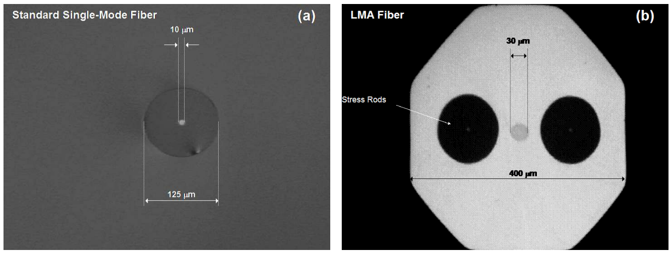

Figure 2.4: (a)Picture of a standard telecom-graded single mode fiber with a core diameter of 10 μm and a cladding diameter of 125 μm (b) LMA fiber with a 30-μm core and hexagonal 400-μm pump cladding. The picture also shows stress rods to preserve the polarization properties.

Two stages of free-space-coupled power amplifiers with the LMA fibers were used for further amplification of he pulses to the MW peak powers. The first stage power amplifier utilizes a fiber with 30-μm-diameter, 0.06-NA core and a pump cladding with 250-μm diameter and 0.45 NA, with available pump power of 50 W. Single-mode operation is achieved by coiling the fiber to a radius $\sim 4.25cm$, giving a measured mode quality of $M^2 \approx 1.05$.

The final amplifier stage is the 80-μm-diameter 0.06-NA-core fiber with a 400-μm diameter, 0.46-NA inner pump cladding. The fiber is end-pumped by diode lasers with a pump power of 650W by combining a 915-nm and a 974-nm laser diodes. Regardless of a very large mode field area of 2749 μm^2, the output beam quality was optimized by fiber coiling and mode matching, permitting the best output beam quality of $M^2 \approx 1.3$ [34].

In order to suppress CW ASE peaked at 1039 nm, the acoustic optic modulator (AOM) with a minimum window size of 100ns was placed in between the preamplifiers, and two bandpass filters with 20-nm-FWHM bandwidth were implemented in between the power amplifiers. The output ends of the power-amplifier fibers were protected with short pieces of splice-on coreless fiber from peak-power surface damage. The length of these protection pigtails is determined by the output beam quality and the mode field diameter of the fundamental mode, giving the required length $\approx 4mm$ for the $30\mu m$ fiber and ≈ 6 mm for the $80\mu m$ fiber.

The second-stage power-amplifier fiber is packaged in a water-cooled heatsink and a temperature-controlled end mount to ensure a good thermal dissipation and pointing stability of the output beam, which will be discussed in Section 2.7.

The overall system performance is summarized in Table 2.1.

Stages	1	2	3	4
core Diameter (μm)	6	6	30	80
Cladding Diameter (μm)	125	125	250	400
length (m)	10	2	2	3.3
Polarization	PM	PM	PM	non-PM
Best Mode Quality	SM	SM	$M^2 = 1.05$	$M^2 = 1.3$
Pump absoprtion (@975nm db/m)	2	250	9	6
Availabel Pump	0.6W @976nm	0.6W @976nm	50W @ 976nm	380 @975nm 220 @976nm
Energy Extraction using 2ns seed and 1.75kHz Repetition Rate Energy from FP diode = 0.6nJ per pulse				
Energy @ 2ns	13.6nJ	422nJ	181 μJ	3.1 mJ
Corresponding Gain (dB)	13.5 dB	14.9 dB	26.3 dB	12.2 dB
Performance on Average Power with 100kHz Repetition Rate and 1-ns seed Seed power from FP diode = 61.6 μW				
Average Power	1.377mW	28.9mW	6.30 W	140 W *
Corresponding Gain	13.5 dB	13.2 dB	23.4 dB	13.5 dB or 65% slope efficiency

*Peak power here is limited by the degrading polymer coating.

Table 2.1: Summary of the system performance including the gain fiber characteristics and the output gain, mode quality, power characteristics

2.4 Mode Quality Optimization

Scaling the core sizes beyond single-mode fibers while maintaining close-to-diffraction-limited mode qualities is of particular interest to many applications when both a high peak power and a good beam quality are highly demanded. Peak power extraction with a single-mode output are consummated by two distinct core-size-scaling strategies.

The first one is to increase the core size beyond the single mode waveguide criteria in the conventional index-guiding fibers governed by the normalized vector V$<$ 2.405 where $V = \frac{2\pi}{\lambda} \times a \times NA$, a is the fiber core radius, and NA is the numerical aperture. In this type of so called large-mode-area (LMA) fibers, single-mode operation can be achieved by proper mode excitation condition [68] or by using fiber bending induced higher-order-mode (HOM) suppression [69].

The other way to achieve single mode operation is to lower the NA in accordance to the core size in order to meet the single mode criteria. Since fabrication process of conventional modified chemical vapor deposition (MCVD) is limited to a $\approx 0.06NA$, the approach of a large-core low-NA structure can only be exclusively achieved by the photonic crystal fiber (PCF) [70]. However, such an approach restricts the fiber from bending for a core diameter greater than $\approx 40\mu m$ and also is fabricated in a stiff-rod geometry. As a result, a large core PCF can only be operated in the laboratory setup, greatly impeding its practical implementation to commercial products.

The practical advantage that conventional a step index LMA fiber has over PCF is that it allows compact packaging by fiber coiling. Careful mode control can be done to improve the mode quality to make the output beam close-to-diffraction-limited even the normalized vector V does not meet the single mode criteria.

The change of the guided modes takes place in two main processes during guided-wave propagation in a LMA fiber. The first process is the power exchange between different modes caused by perturbations in a fiber core. The second and the more important mechanism for modal control happens in a strongly bent fiber, in which the leakage of the modes from a fiber core to the cladding through optical tunneling (Figure 2.5).

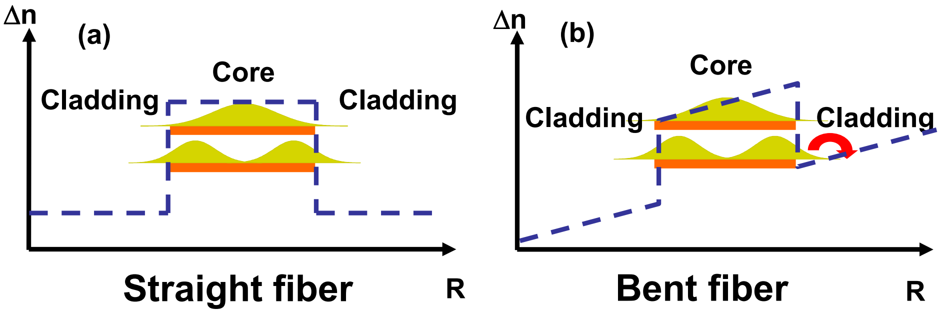

Figure 2.5: Bending induced optical tunneling showing (a) the refractive index profile for a straight fiber and (b) the effective refractive index profile after conformal transformation due to bending as seen by the optical wave propagating in the fiber, which allows optical tunnelling of higher order modes into the cladding.

Optical tunneling happens at a curved interface between two dielectric media, when the electromagnetic wave incident from the medium with higher refractive index (n) at angles greater than the critical angle, it becomes only partially reflected. This frustration of the total internal reflection is caused by the phase velocity of the wave in the denser medium is lower than the phase velocity of the plane wave in the less dense medium. Due to the curvature of the interface, these phase velocities become equal at a tunneling distance from the interface

$$\gamma_{tunnel} = \rho(\frac{\sin \alpha_{inc}}{\sin \alpha_{crit}} - 1) \tag{2.2}$$

where ρ is the radius of curvature of the interface, α_{inc} is the incident angle from the denser (larger n) medium, α_{crit} is the critical angle. Since optical wave cannot propagate faster than the phase velocity in the medium, for all $r > r_{tunnel}$, it will acquire phase velocity component non parallel to the interface. As a result, for $0 < r < r_{tunnel}$, the wave in the second medium is evanescent and for $r > r_{tunnel}$, is propagating at the phase velocity of the light in the lower-index medium, i.e. the wave will tunnel through the gap $0 < r < r_{tunnel}$. This optical tunneling process through a curved interface in a bent waveguide can be equivalently described in terms of tunneling through a dielectric barrier [71], which appears when representing waveguide bend through conformal mapping as a refractive index slope as shown in Figure 2.5. In other words, mode propagation in a bent fiber can be equivalently represented as mode propagation in a straight fiber, in which different path lengths seen by light traveling around a bend of radius R at different transversal position x can be accounted through the equivalent refractive index profile $\eta_{equivalent} \cong \eta_{straight}(1 + \frac{x}{R})$

An important result for a bent optical waveguide is that this curvature-induced loss increases with the guided-mode order, thus providing with a convenient mode filtering mechanism [69]. The mode quality improvement from coiling can be simulated numerically by the model described in [72]. Modal scattering coefficient was assumed to be the same for all modes and the magnitude of this coefficient is estimated from experimental evidence. Mode control behavior was experimentally investigated in the two fibers, an $115\mu m$ as shown in Figure 2.6 with $350\mu m$ octagonal cladding, and a $80\mu m$ core fiber with $400\mu m$ octagonal cladding as shown in Figure 2.6.

In the case of $115\mu m$ fiber , the mode quality is improved from $M^2 \sim 11$ (loosely coiled fiber with coiling diameter $\approx 14.5cm$ to $M^2 \sim 5.5$ with coiling radius $\approx 3.5cm$ (Figure 2.7).

Hoverer, the mode quality improvement comes at the expense of the loss in the transmitted power. In this case of 115-μm-core fiber , the transmission penalty is $\approx 50\%$ at coiling radius of 3.5 cm. In the amplifier configuration, this transmission

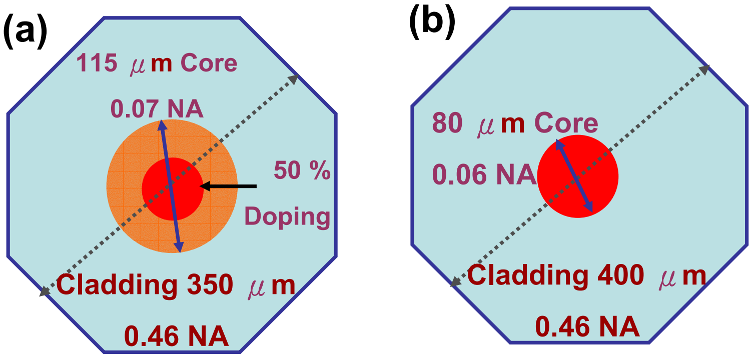

Figure 2.6: (a) LMA fiber with confined doping showing a 115-μm core and 50% confined doping. (b) The structure of the 80-μm fiber.

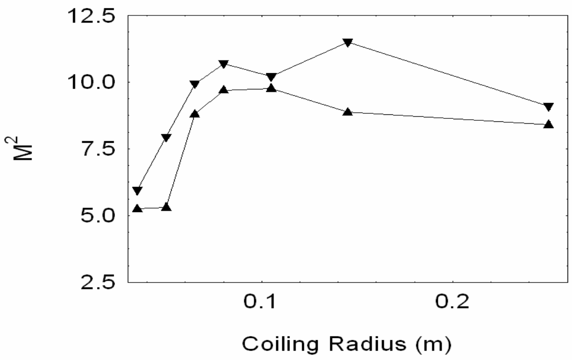

Figure 2.7: Measured M^2 for 115-μm-core output. The two curves correspond to the two orthogonal polarizations. Each data points is averaged over three sets M^2 measurements.

penalty can be compensated by the gain. Nonetheless, in order to retain the amplifier slope efficiency, only a limited loss can be tolerated. Hence, it is the transmission loss penalty that determines the practical limit of the achievable beam quality from a coiled large-core fiber.

In the 80-μm-core fiber, Figure 2.8 plots the two solid curves of the theoretical predictions of mode quality with the highest and lowest scattering coefficient obtained experimentally. It is also observed that there is a shift in the coiling radius in experimental result compared to the theoretical prediction. This discrepancy of the numerically prediction and experimental result was also observed in different core size LMA fiber. One possible explanation for this mismatch is that in the experimental setup, there is usually a certain length of the fiber at the input and output end that is not coiled to the radius as the rest of the fiber. The inconsistency in the coiling radius will effectively change the uniformity in the scattering process.

Indeed, all the efforts in the experiment were made to mode-match excitation beam spot size to that of the fundamental mode at the fiber input and to minimize excitation at the higher order modes. Experimentally, the mode quality for the 80-μm-core fiber was improved from $M^2 \sim 2.5$ to $M^2 \sim 1.3$ from a loosely coiled fiber to a coiling radius around 4.25 cm. The transmission of different coiling radius is also plotted in bottom of Figure 2.8 which shows that transmission loss $\approx 50\%$ at the tighest coiling radius.

Again, one has to keep in mind that the all the rigorous efforts on mode quality improvement in an LMA fiber will all become unnecessary with the introduction of emerging fiber solution [59], in which technology an additional structure around the core will serve as an effectively filters, causing additional loss to the higher order modes.

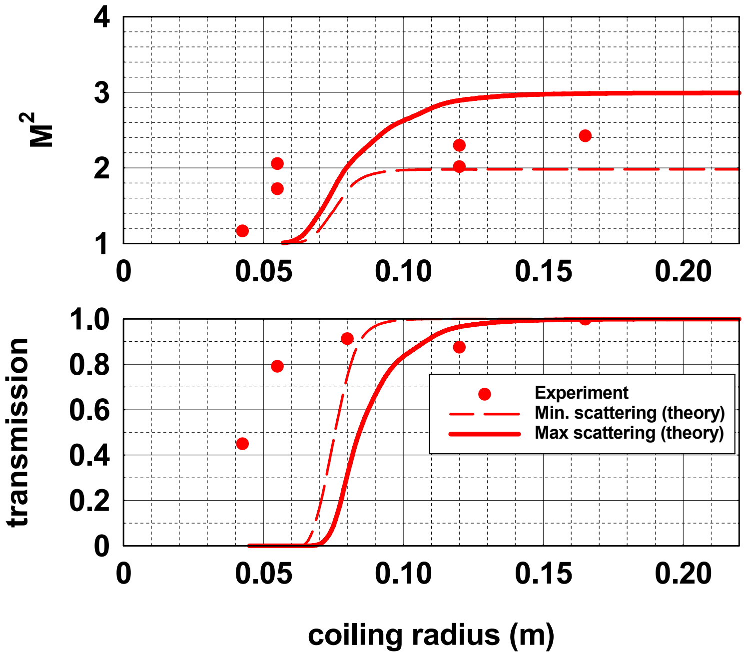

Figure 2.8: Comparison between experimental results and theoretical prediction of the coiling effect on transmission and mode quality for the 80-μm-core fiber. Theoretical predictions uses highest and the lowest mode scattering coefficient attained experimentally as plotted in the dotted curve (minimum scattering coefficient) and solid curve (maximum scattering coefficient)

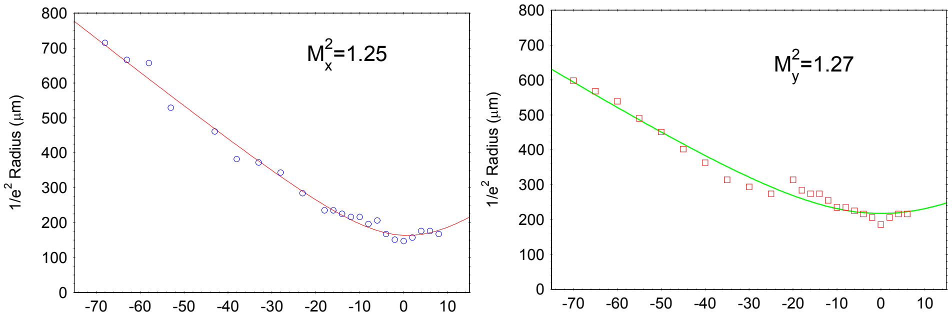

Figure 2.9: Measured mode quality of the 80-μm-core fiber, coiled to radius around 5 cm.

2.5 Peak Power Extraction and Limitations due to Nonlinear Processes

Peak power and pulse energy extraction from the pulsed fiber laser systems had been studied using both conventional LMA fibers [73, 74, 65, 66, 75, 34, 67, 76, 77] and PCF fibers [78, 79, 80, 81, 82, 83]. With LMA fibers, Galvanauskas achieved $1MW$ with 1-ns pulses in a 50-μm-LMA fiber with a diffraction-limited output-beam, and Cheng *et al.* [66] set a record high peak power of 2.4 MW using a multimode 200-μm core-fiber. With PCF large-mode fibers in a MOPA configuration, Teodoro and Brooks demonstrated 1.5 MW at the pulse duration of 450 ps with a diffraction-limited beam using a 1-m-long 40-μm-core PCF fiber, and 4.5 MW using a 140-μm-core-LMA fiber with $M^2 \sim 9$ [80]. Their further work with 100-μm-core rod-like PCF fiber ≈ 90 cm long improve the peak power to 4.5 MW, the highest peak power to date from a PCF, using 1-ns pulses with near diffraction-limited beam of $M^2 \sim 1.3$ [82]. However, this rod-type PCF fiber can not be operated with any micro-bending or macrobending, forsaking the most important advantages of the fiber lasers over the solid-state lasers.

The main impeding factors on the peak power extraction from a fiber laser amplifier are the nonlinearities including stimulated Raman scattering (SRS), stimulated Brillouin scattering (SBS), four-wave-mixing (FWM) and self-phase modulation (SPM) and self-focusing [84]. Fiber lasers are comparatively more susceptible to the nonlinear effects since the interaction length of the fiber laser is inherently two orders of magnitude longer than that of ordinary solid-state lasers [85]. Under different pulse parameters, i.e. pulse durations and bandwidth of the pulse, the nonlinear process occurring first will be somehow different. For bandwidth-limited pulses longer than 10 ns, SBS is the main limiting factor, and for pulses shorter than 0.5 ns, SPM will more likely to induce large distortion of the spectrum [84]. For brand-band pulses in ns-range, the major limiting factor is FWM, which will broaden the spectrum by beating with the Raman noise [75, 86, 87]. In reality, STS is the major limiting factor if FWM-spectral-broadening is acceptable in the application.

In addition, SRS is in strong effect in the same pulse-parameter region and strongly transfers the energy from the signal to the Stokes wave, creating additional loss from the signal wavelength. The Stokes components have a frequency down shifted by an amount dictated by the vibrational modes of the medium. In the case of fused silica, the Stokes wave is down shifted by $\approx 13.2THz$ ($\approx 50.5nm$) resulting a Stokes wave centered $\approx 1115nm$ for a 1064-nm signal. This adverse nonlinear effect will shed the energy from the amplified signal to the Raman Stokes, thus considerably loss the power from the intended amplified wavelength.

Since the strength of the nonlinear effects are proportional to the peak power of the signal and the interaction length, one important parameter characterizing the magnitude of a nonlinear effect is the integration of the signal power over the length of the fiber: the effective propagation distance, given by,

$$L_{eff} = [1 - \exp(-gL)]/g \tag{2.3}$$

where L is the fiber length, g is the amplifier gain, assumed to be constant along the fiber. The SRS threshold is denoted as the power transferred to the Stokes equals the power of remaining in the pump ($P_s(L) = P_p(L)$) and given by,

$$P_0^{cr} \approx \frac{16A_{eff}}{L_{eff}g_R} \tag{2.4}$$

where A_{eff} is the effective area, g_R is the peak Raman gain, with a magnitude $\approx 1 \times 10^{-13}$ at the pump wavelength of 1064 nm, and scales inversely at other wavelength [84](note that the critical power is the input power of the amplifier).

Critical power for backward Raman scattering bears the same form as Equation 2.4 with the numerical factor 16 replaced by 20. However in practice, we had usually experienced a SRS thresholds around two times higher than the peak power predicted by Equation 2.4. We contributed this discrepancy to the approximation by Smith [88] of a very long fiber, which become somehow invalid in our < 3 m long fiber amplifiers.

It is obvious that one can increase the core size (with a possible trade off of mode degradation) or decrease the length of the fiber (with a possible trade off of less pump power absorption) to increase the Raman-limited peak power. Figure 2.10 plots the scaling of Raman threshold for a three meters long fiber with 20 dB gain, it is shown that Raman threshold is $\approx 100kW$ for the $30\mu m$ and $\approx 0.7MW$ for the 80-μm-core fiber. Note that the effective mode field areas for fibers with step-index fiber of 0.06-NA cores used in the analysis is calculate by FiberCAD $A_{eff} = 0.375D_{core}^2 + 3.95D_{core} + 32.7$ where A_{eff} is in μm^2 and D_{core} is the core diameter in μm.

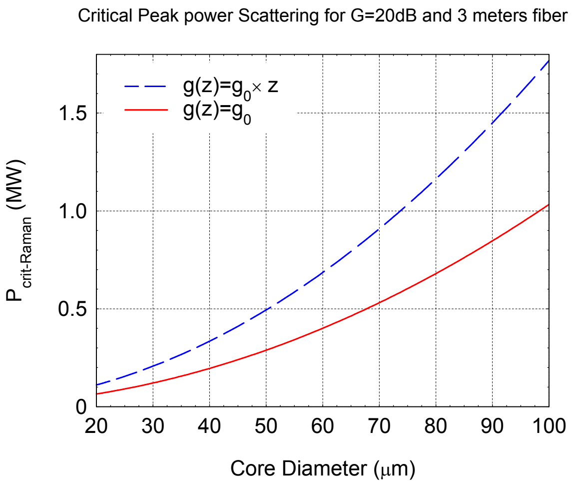

Figure 2.10: Scaling of the SRS as a function of the core diameter with a core NA of 0.06. The example shown here is for a 3-m fiber with 20-dB gain. Two curves plotted here are shown, with the solid one assuming a constant gain and the dashed curve assuming a linearly increasing gain, giving a higher SRS threshold.

In our fiber-laser EUV driver, the first two stages of preamplifier are telecom-graded single mode amplifier with standard core size, it is important to choose the fiber with length for adequate pump absorption but also minimized effective length will be preferred for higher nonlinear threshold. This consideration was taken into account when designing the EUV driver (Section 2.3), and a longer fiber of 10 m was used in the first preamplifier, in which the amplified peak power is in the order of 50W, to exploit the power gain (20dB in this stage). A shorter fiber of 2 meters with a higher doping concentration is used in the second preamplifier to increase the critical Raman power threshold. Also, counter-propagating pumping in the two stages of the LMA power amplifiers is another effective way to shorten L_{eff}, since the gain increases while approaching the end of the fiber.when this pumping configuration is used, yielding the integration of the signal power over the length of the gain fiber smaller.

Another factor changes the L_{eff} is the gain saturation. When the input fluence is strong enough, the gain will saturate at the end the amplifier. Therefore, the integration of the power over the length of the fiber in a saturated amplifier will be larget than that in a unsaturated amplifier under that same condition, yielding a longer L_{eff}. It is important to keep this effect in mind when optimizing the peak power extraction.

The evidence of SRS revealed in the output spectrum and also in the pulse temporal measurement. Figure 2.11 shows the spectra of the output pulses at various amplified peak powers. The example of SRS shown here is from the output of a co-propagating-pumped, 4.2-m, 30-μm fiber, seeded with a 2-ns-squared pulse and 0.18-kW input peak power.

Due to the temporal deformation by saturated gain, the output peak power was

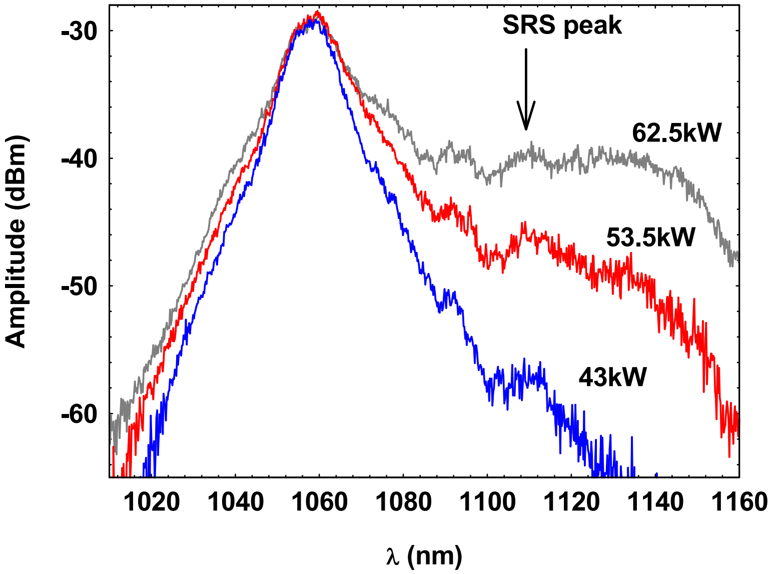

Figure 2.11: Spectrum of the amplifier output, showing the increase of the Stokes component at 1115 nm with the increase of power. The amplifier shown here is a 30-μm-core fiber and 4.2-m long. Seed pulses are 2-ns squared pulse with 0.18-kW peak power.

calculated by integrating the temporal profile and then normalizing with the measured energy, given by,

$$P_{peak} = \frac{E_{measured}}{\int_0^{\tau} P_{norm}(t)dt} \tag{2.5}$$

where $P_{norm}(t)$ is the normalized temporal profile with the peak set to unity.

As shown in Figure 2.11, the spectral component in the Raman band increases significantly when the peak power of the laser output increases from 43kW to 63kW. Figure 2.12 shows another evidence of SRS in the pulse temporal profile. The highest peak of the temporal profile disappears if the measurement was done after a narrow-band filters. (Note that the temporal measurement was done with an InGaAs photodiode with a 150-ps rise time and an oscilloscope with a 40-GHz bandwidth.) This absence of the temporal peak is because this part of the signal was transferred to the Stokes wave through the Raman gain, blocked by the a 10-nm filter. These band-pass filters are placed in between the amplifier stages for ASE suppression.

This shedding of the power away from the signal will consequently impede the peak power extraction.

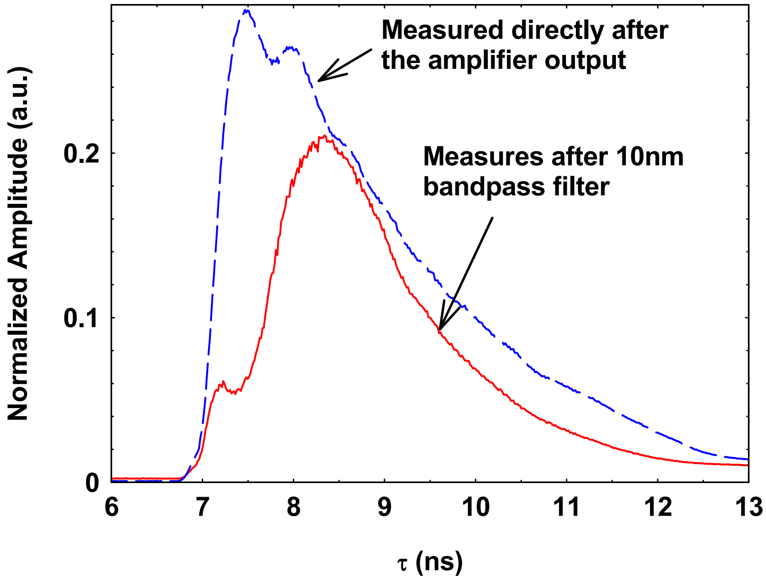

Figure 2.12: Another evidence of SRS observed in the temporal profile. Temporal profiles shown here are measured after the 30-μm-core fiber output with a peak power of 65 kW. The difference of the two profiles shown here is due to a 10-nm band-pass filter (for ASE filtering). The profile measured with the ASE filter shows a missing peak, due to the shedding of the signal power into SRS Stokes waves, which has spectral components out of the filter pass-band.

2.5.1 Self-focusing Limit on Peak Power Extraction

The ultimate limit of the peak power in a laser gain medium is imposed by self-focusing damage. It is a Kerr nonlinear process with an intensity dependent refractive index $n = n_0 + n_2 I$ [63] where n_0 is the linear index ($n_0 = 1.45$ for fused silica), n_2 is the nonlinear refractive index and I is the intensity. The critical peak power for self-focusing is expressed by,

$$P_{cr}^{sf} = \alpha \frac{\lambda^2}{4\pi n_0 n_2} \tag{2.6}$$

where λ is the wavelength in free space, α is an constant independent of material with a value of $\alpha = (1.22\pi^2)/8 \approx 1.8362$.

In a bulk medium, when the peak power of the propagating pulse is greater than P_{cr}^{sf}, refractive index distribution modified by the intensity profile (behaving as a focusing lens) will overcome the beam diffraction and cause the beam to collapse, then at some point, the peak intensity will exceed the material bulk-damage threshold, resulting in catastrophic damage. However, the exact critical peak power in fiber laser waveguide is mandated by the nonlinear refractive index in the fused silica, varying from $n_2 = 1.0 \sim 3.2 \times 10^{-20} m^2/W$, depending on the experimental techniques to extract the nonlinear n_2 [89]. As a result, P_{cr}^{sf} can range from 3.5 MW to 11.3 MW for 1064-nm pulses in fused silica. A thorough review on the measured n_2 of silica under different measurements for λ from 249 nm to 1550 nm can be found in [89].

Another factor that is associated with the value of n_2 is its contributing effects: Kerr and electrostrictive. The Kerr effect includes the electronic and Raman response, giving $n_2(fast) = 2.1 \sim 2.3 \times 10^{-20} m^2/W$ [90, 91]. The electrostrictive contribution ($n_2(str)$) is due to the change in the material density associated with the presence of an intense electric field, and its value depends strongly on the duration and the intensity spectrum of the pump pulse. Several works [92, 93, 94, 90, 95] investigated its magnitude and physical impact in an optical fiber. Buckland and Boyd [92] introduced the fractional electrostrictive contribution, given by

$$\eta \equiv n_2(str)/n_2(fast) = \chi^{(str)}/\chi^{(3)} \tag{2.7}$$

where $\chi^{(3)}$ is the third order electrical susceptibility includes both electronic and the Raman contributions. Their numerical analysis showed that the contribution of $n_2(str)$ could be negligible for pulses shorter than 100ps, and $\eta \sim 0.2$ for pulses longer than 1 ns. We can see that the P_{cr}^{sf} is higher at short pulses ($\sim 100ps$) and lower when the pulse duration is longer than 1 ns.

Several theoretical works studied the behavior of beam diameter change due to

Kerr nonlinearity close to critical peak power. For pulses with different spatial profiles, [96] reported an analytical solution on the spatial shape of the pulse profile shows that the critical power is within $\sim 10\%$ of the value predicted by the Townes soliton. Other detailed studies on the self-focusing threshold can be found in [97, 96, 98] and all of the theoretical predictions with different numerical or analytical approaches give the similar results as described by Equation 2.6.

However, even several experimental studies [34, 81, 79] had already reported the critical peak power that is higher than the predicted self-focusing critical peak power, no experimental evidences had prove the existence of self-focusing in the Yb^{3+}-doped amplifier. One possible reason for this discrepancy is the lack of inclusion of some physical phenomenon that alters the beam spatial profiles, such as gain saturation, in the previous models. To better understand Kerr-nonlinearity in the waveguide when operating in the high saturated region, we developed a numerical model using beam propagation method (BPM).

The scalar Helmholtz wave equation, governing the wave propagation in an inhomogeneous medium of cylindrical symmetry, is expressed as,

$$\frac{\partial^2 E}{\partial r^2} + \frac{1}{r}\frac{\partial E}{\partial r} + \frac{\partial^2 E}{\partial z^2} + \frac{n^2(r)\omega^2}{c^2}E = 0 \tag{2.8}$$

where E is the electrical field and represented as $E(r,z) = A(r,z)e^{-jkz}$ and k is the propagation constant $k = 2\pi n_0/\lambda$ and n_0 is the average refractive index of the propagation.

Adding the Kerr-nonlinearity-induced refractive index modulation and the saturated gain of the media, Equation 2.8 can be written as,

$$\frac{\partial A}{\partial z} = \frac{-j}{2n_0 k}(\frac{1}{r}\frac{\partial A}{\partial r} + \frac{\partial^2 A}{\partial r^2}) - \frac{j}{2k}[(\frac{n(r)\omega}{c})^2 - k^2]A - jkn_2\left|A\right|^2 A + \frac{g(r)}{2}A \tag{2.9}$$

where $g(r)$ is the transversely dependent power gain, given by [63],

$$g(r) = \frac{g_0}{1 + \frac{I(r)}{I_{sat}}} \tag{2.10}$$

and $I_{sat} = \frac{\hbar\omega}{\sigma\tau}$ where U_{sat} is the saturation fluence and τ is the pulse duration of the signal.

By implementing the fast Fourier transform beam propagation method (FFT-BPM), Equation can be treated as two actions of propagation over a very small Δz The first being the divergence of the beam in the medium is described as

$$\frac{\partial A}{\partial z} = \frac{-j}{2n_0 k}(\frac{1}{r}\frac{\partial A}{\partial r} + \frac{\partial^2 A}{\partial r^2}) \tag{2.11}$$

the second being the modification of the phase front due to waveguide and Kerr nonlinearity index modulation, as well as the saturated gain of the fiber,

$$\frac{\partial A}{\partial z} = -\frac{j}{2k}[(\frac{n(r)\omega}{c})^2 - k^2]A - jkn_2 \left|A\right|^2 A + \frac{g(r)}{2}A \tag{2.12}$$

Following the nomalization detailed in [99], a numerical recipe implementing the quasi-Hankel transform [100] and the end correction [101] provides a fast solution in cylindrical coordinate to study the effect of saturated gain, and Kerr nonlinearity in an cylindrical waveguide for the fundamental mode (LP_{01}).

First we simulate the propagation in a bulk medium (Figure 2.13). In order to simulate the same spot size as in a fiber amplifier (60-μm mode field diameter beam), we assumed a gain of $20dB$ over the Rayleigh range (3.85 mm for this beam size) to prevent the beam from diverging due to diffraction. We assumed the input peak power of 0.6 MW and the critical self-focusing power of 6 MW.

When the gain saturation is not included(Figure 2.13 (a)), the numerical result showed that Kerr nonlinearity will overcome the diffraction and collapse the beam, when the signal power amplified beyond the critical peak power. In a saturated-gain medium, the beam waist starts to collapse at a remarkably higher peak power

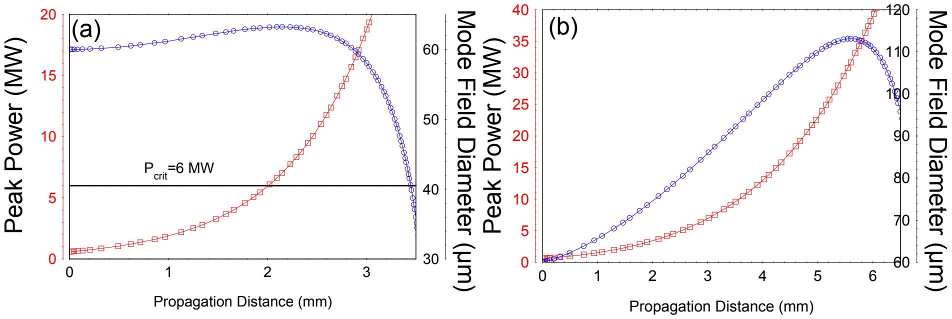

Figure 2.13: Propagation in the bulk media with the consideration of Kerr nonlinearity with (a) no gain saturation and (b) gain saturation

(Figure 2.13 (b)), considering the same gain per unit length. In both cases, the gain is confined in an 80-μm-diameter cylindrical region, to precisely emulate the gain profile in the gain fiber. It is also important to note that in reality, the spot size in a bulk media is much larger than the parameters chosen. The spot size and propagation length was chosen only to compare the same parameter space as in the fiber gain media.

Kerr nonlinearity was then numerically studied in the gain fiber with a 20-dB gain per meter, with the inclusion of the waveguide effect. The simulation used the following parameters: an input pulse duration of 0.5 ns with a pulse energy of 300 μJ, $\sim$ 6 times smaller than the saturation fluence of the 80-μm-core fiber, corresponding a peak power of 0.6 MW. The Kerr nonlinearly of $2.2 \times 10^{-20} m^2/W$ is chosen, giving a critical peak power of 5.41MW from Equation 2.6. Figure 2.14 plots the evolution of the peak power and the mode field diameter in the 80-μm-core fiber without considering gain saturation (on the left) and with consideration of gain saturation (on the right).

The trends in both cases show the same converging behavior of the beam-width as a function of the peak power. Since the gain is quenched in a saturated amplifier, the only difference is that it requires a longer amplifier length to reach the same peak

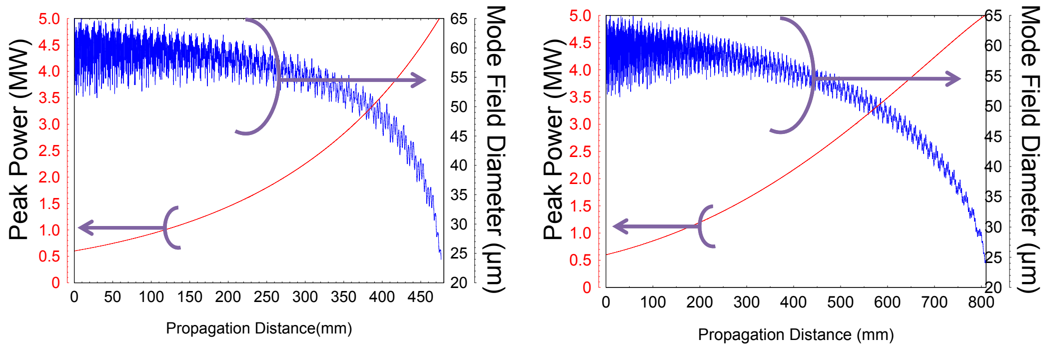

Figure 2.14: BPM simulation of the amplified signal in the waveguide with (a) no gain saturation and (b) gain saturation.

power in the saturated gain fiber as the energy is amplified close to the saturation energy. One very important result followed from this numerical study is that the beam-width of the fundamental mode start to decrease at the peak power of 1.5 MW, only 27 % of the critical peak power and the mode field diamter reduced to half of the original when the peak power reaches 4.5MW, giving the same trend as reported in Ref. [98] where FD-BPM was implemented.

In summary, from the FFT-BPM numerical analysis, it is clear that even with the inclusion of gain-saturation-induced transversely-dependent-gain, i.e. a higher gain on the wing of the Gaussian profile and a lower gain in the central peak, the self-focusing effect due to Kerr-nonlinearity still presents when the beam is amplified toward the critical peak power in the waveguide configuration. However, no experimental evidence on the change in the output beam divergence in the gain fiber has been reported, even though the achieved peak power is very close [82], or even beyond the critical self-focusing peak power [34]. The physical explanations for this repeated discrepancy require further investigations.

2.6 Energy Extraction and Pulse Temporal Shaping

In a high energy pulse amplifier, one physical limitation on the pulse energy extraction is the time varying gain saturation. In order to efficiently extract the energy in the inverted gain medium during its passage through the amplifier, the input pulse must be intense enough to cause significant saturation of the population inversion. However, an efficient energy extraction of the amplifier will lead to a sometimes undesirable result that the amplifier gain will be greatly reduced from its initial value to a small residual gain during the passage of the pulse, referred as the gain saturation.

Gain saturation can be visualized as the depletion of the excited states of the population inversion by the stimulated emission of the signal and one physical parameter to characterize this mechanism in one amplifier is the saturation fluence,

$$J_{sat} = \frac{h\upsilon_s}{(\sigma_{es} + \sigma_{as})\Gamma_s} \tag{2.13}$$

where $h\upsilon_s$ is the signal photon energy, σ_{es}, σ_{as} are the emission and absorption cross-sections at the signal wavelength, and Γ_s is the signal overlap with the active dopant [73].

Both the emission and absorption cross-sections of Yb^{3+} in SiO_2 are wavelength dependent and the spectroscopic properties were characterized by Paschotta and coworkers [102]. One can also approximate the emission and absorption cross section by approximating the Lorentzian line-shape for the absorption peak and emission peak [103]. For Yb^{3+} in SiO_2, the emission peak is centered at 1036 nm with the peak emission cross section of $\sigma_{es}(1036nm) = 0.55 \times 10^{-24} m^{-3}$ and a spectral bandwidth of $\Delta\upsilon_{es} = 50nm(FWHM)$. One absorption band is centered at 974 nm with the peak absorption cross section of $\sigma_{as}(974nm) = 3.5 \times 10^{-24} m^{-3}$ and a spectral bandwidth of $\Delta\upsilon_{as} = 8nm(FWHM)$. With the above parameters, the saturation fluence at 1064 nm is calculated to be $\sim 0.66\mu J/\mu m^2$ using Equation 2.13. The saturation energy is then given by,

$$E_{sat} = J_{sat} \times \frac{A_{dope}}{\Gamma_s} \tag{2.14}$$

where A_{dope} is the doped area, Γ_s is the signal overlap with the active dopant.

Table 2.2 listed the saturation energies for the LMA fibers of different core sizes studied in the pulse energy extraction,

Core Size	N.A.	Doping	E_{sat}
$6\mu m$	0.11	Uniform	29.2 μJ
$30\mu m$	0.6	Uniform	322.5 μJ
$50\mu m$	0.6	Uniform	771 μJ
$80\mu m$	0.6	Uniform	1814 μJ
$115\mu m$	0.7	Confined (50%)	14.38 mJ
$200\mu m$	0.6	Confined (50%)	41.8 mJ

Table 2.2: Saturation energies for various fiber core sizes using the Equation 2.14

Two important physical limitations are associated with this amplifier saturation. The first one is the deformation of the pulse temporal shape when an amplifier is under the saturated-gain region and the second is the extractable energy. Temporal pulse deformation, due to gain saturation, tends to provide more gain to the leading edge of the pulse than to the rest of the pulse, according to the time-dependent saturated-gain [63],

$$G(t) = 1 + (G_0 - 1)\exp[-J_{out}(t)/J_{sat}] \tag{2.15}$$

where G_0 is the small signal gain, J_{sat} is the saturation fluence, and J_{out} is accumulated energy fluences from the starting time t_0 in the passage of the pulse, defined as

$$J_{out}(t) \equiv \int_{t_0}^{t} I_{in}(t)dt \tag{2.16}$$

where $I_{in}(t)$ is the instantaneous intensity at the time t.

Figure 2.15 showed one example set of the pulse-shape deformation observed in the two stages of the power amplifiers with a 10-ns squared-pulse input. The first power amplifier (30-μm core) had an output energy of 92 μJ, approximately three times lower than its saturation energy, and the output temporal profile already showed moderate pulse reshaping. The second power amplifier (80-μm-core) has an output energy of 2.1 mJ, slightly higher than the saturation energy($\sim$ 1.8mJ), inducing a very strong deformation on the temporal shape (the solid curve in Figure 2.15). Consequently, the FWHM pulse duration was shorten to $\sim$ 2 ns.

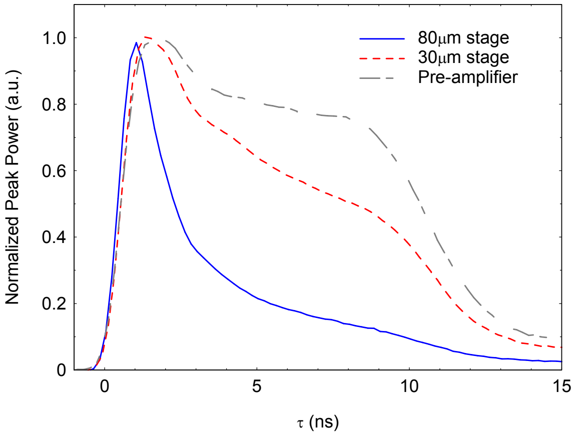

Figure 2.15: Temporal shaping due to gain saturation at the output of two power amplifiers. The input pulse energy after the preamplifier is 0.48 μJ with a 10.2-ns pulse duration. After the 30 μm stage, the output energy is amplified to 92 μJ with a pulse duration of 7.5 ns. Slight pulse shaping is observed even though the output energy is less than 40% of the saturation energy for this fiber. The output energy of the 80-μm-core amplifier is 2.1 mJ with pulse duration of 1.9 ns. Pulse shortening and reshaping is more severe in this stage, since the output energy is higher than the saturation energy of this fiber.

As a result, the implicit impediment of this pulse shortening is that once the leading edge of the pulse is amplified to the nonlinear critical peak power, the trigger of the undesired nonlinear effect, as described in Section 2.5, will generate out-of-band spectral components and deteriorate in-band energy extraction. However, many laser applications require a specific temporal shape of the laser pulse, therefore, it is necessary to preshape the seed pulse to compensate the gain-saturation-induced temporal-shaping to provide a desirable temporal shape. In principle, with the Equation 2.15, one can numerically predict the output pulse shape from an known input pulse with a certain shape and energy, knowing the saturation energy (calculated from the mode field diameter) and small signal gain (measured experimentally). Figures 2.16 and 2.17 show the predicted output shapes and energy with various input-pulse shapes, using the parameters of the 80-μm-core fiber amplifier, i.e. a small signal gain of 20 dB and a saturation energy of 1.8 mJ.

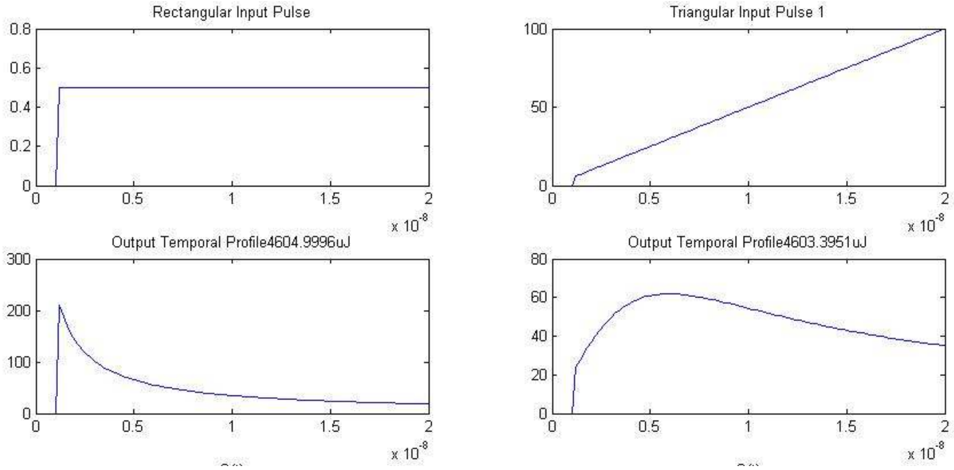

Figure 2.16: Output pulse shape with a squared-shaped and triangular-shaped input pulse, both having a pulse energy of 200 μJ. The same temporal duration of 20 ns is used for all temporal shapes for comparison. It is seen that the output pulse shape is largely deformed for a rectangular input pulse, compared to the output with a triangular input-pulse shape.

In order to compared the effect of the input-pulse shape on the output, the input pulse energies are chosen to be 200 μJ and the temporal durations are fixed to be 20 ns for all pulses. It is interesting to observe that the overall output energy are the same ($\approx$ 4.6 mJ) for all four input pulses even with very different input

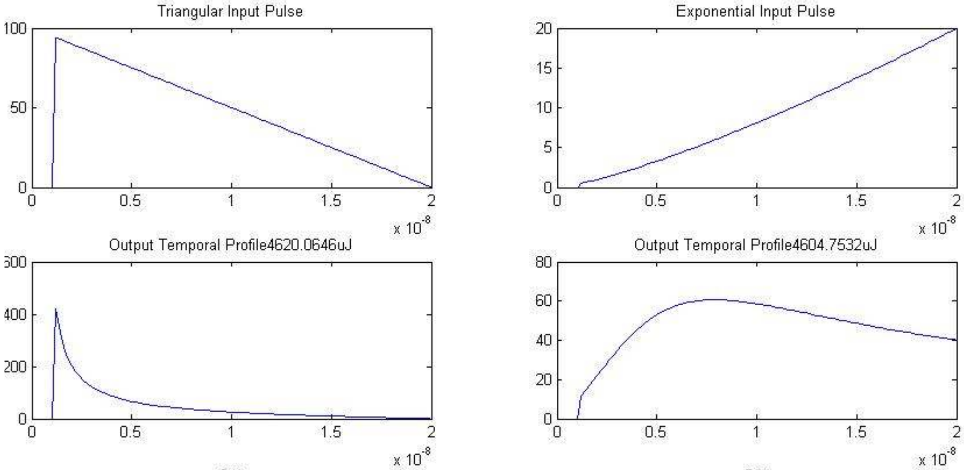

Figure 2.17: Continuation of Figure 2.16 with a triangular shape, which resemble closely the input pulse shape in the experiment. Another ideal exponential pulse shape is shown on the right.

shapes. Indeed, very different extent of deformations on the output pulse shapes is resulted from different types of leading edge. The peak power varied as much as ≈7 times between the triangular-shaped input pulse and the pulse with an exponential shape (Figure 2.17). These discrepancies in the peak powers certainly have different strength of nonlinear effects, regardless of the same extracted energy. This numerical analysis justified the need for active pulse to provide a slow rising edge to optimize the extracted energy, with the peak power below the limit of nonlinearities.

The validation of this analysis is also confirmed by applying Equation 2.15 to one set of experimental measurement. The numerically predicted and the measured output pulse shape shows a very good agreement (Figure 2.18).

2.6.1 Active Pulse Shaping and Generation of Prepulses by an Arbitrary Waveform Generator

One key parameter, other than the intensity, to optimize plasma generation is the temporal shape of the pulse. It is believed that the plasma condition, which is closely related to the overall EUV yield, is highly dependent on the temporal shape of the laser pulse, however, no direct evidence can be found in previous works

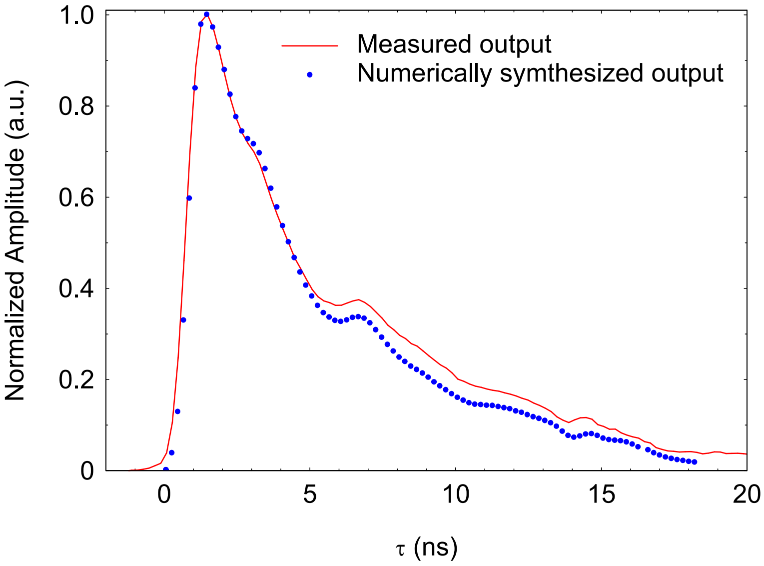

Figure 2.18: A good agreement between the calculated and measured output pulse shape from the 80-μm-core fiber. The calculated output pulse is obtained by using the Equation 2.15 and the measured energy and shape of the input pulse.

because of the absence of a temporal-shaping capability from solid-state lasers. In order to explore the dependence of plasma dynamics on the laser temporal shape and duration, we adapted a high-speed computer-interfaced digital arbitrary waveform generator (AWG) to drive the seed diode. This AWG has a risetime of 200 ps and a temporal resolution of 1 ns, providing a programmable seed pulse with a temporal duration up to 4 ms. Its 12-bit vertical resolution provides an ample dynamic range, enabling synthesis of high-contrast pulses.

In combination with a high-power large-bandwidth radio frequency (RF) amplifier, spanning from 0.5 MHz to 1 GHz, and a current-doubling transformer, this combination of driving circuitries generates electrical current $\geq$ 36 times the diode threshold current, providing high-quality optical pulses with a good power dynamic range. All the electrical driving circuitries were carefully designed to ensure a 3dB-bandwidth larger than 1GHz, eliminating possible capacitive oscillations on the electrical driving signal, as reported in Ref. [104]

Because of gain saturation in the power amplifiers, it is imperative to provide a temporally-preshaped seed pulse to the amplifier system for the extraction of temporal-shape-controlled high energy pulses. Adaptive-pulse-shape control was previously demonstrated to iteratively determine the shape of the input pulse required for a specific output-pulse shape [104], using a feedback loop and an algorithm to adjust the input seed pulse, in accordance to the measured output pulse shape.

We found that such adaptive control is elective. Indeed, if the small signal gain and the saturation energy of an amplifier stage is accurately known, one can closely relate every output pulse shape and energy to the corresponding pulse shape and energy at the amplifier input, using the following formula [63],

$$I_{in}(t) = \frac{I_{out}(t)}{1 + (G_0 - 1)exp[-\frac{\int_{t_0}^{t} I_{out}(t)dt}{U_{sat}}]} \tag{2.17}$$

where $I_{in}(t)$ is the input pulse power, $I_{out}(t)$ is the output pulse power, G_0 is the small signal gain of the amplifier, t_0 is the beginning of the pulse and U_{sat} is the saturation energy of the amplifier. Experimental verification of its accuracy is presented in 2.19, where a measured 5-mJ amplified pulse profile (dashed line) is shown together with the corresponding measured input pulse profile (solid line), and the reconstructed input pulse profile (marked line) calculated from the measured output shape by using Equation 2.17. Good agreement between the measured and numerically reconstructed input pulse shapes verifies this relatively simple but effective means of predicting required input pulse shape for achieving a desired amplified pulse shape. Note that in this example, the amplified pulse energy is ≈ 2.8 times larger than the saturation energy of the amplifier, i.e. the amplifier is operated under a strongly saturated-gain condition.

Furthermore, this approach for a single stage amplifier can be extended to enu-

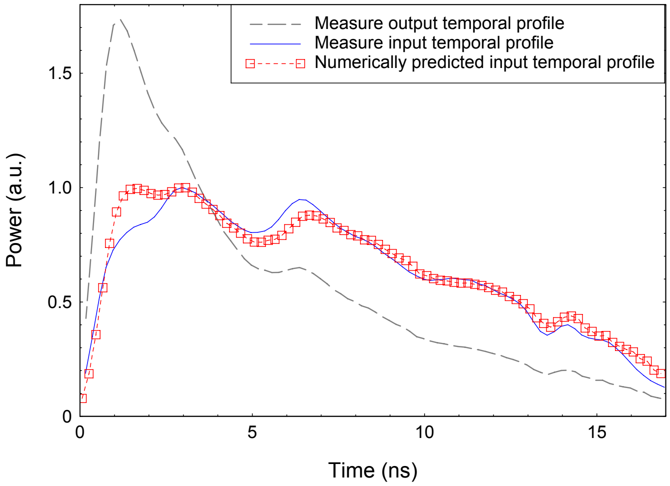

Figure 2.19: Example of numerically obtaining the input seed pulse including the effect of saturated gain from an output pulse of known shape and energy. Input pulse shape can be determined by knowing the saturation energy and the small signal gain of the amplifier. The example shown here is for 5-mJ 1064-nm amplified output pulse from an 80-μm-core Yb-doped fiber.

merate the required seed pulse at the input of a multiple-stage fiber amplifier in which all the saturation energies and the small signal gains are known for each stage (together with the accurate knowledge of all the losses in various fiber-optic components between the stages.) Figure 2.20(a) shows an example of the amplified pulse shape at the output of the four-stage amplifier under consideration and Figure 2.20(b) shows the corresponding measured (solid line) and predicted (marked line) seed pulses. Again, the good agreement on the measured and numerically predicted seed-pulse shape validates the direct approach based on the Equation 2.17.

Another propitious property resulting from using an AWG is the ability to introduce pre-pulses with programmable delays, controllable contrast and pulse durations. Pre-pulses were reported to improve the EUV conversion efficiency by creating pre-plasma, which is more effectively heated by the main irradiating laser pulse [32]. However, most of the previous works with pre-pulses use lasers of two different wavelengths for the pre-pulse and the main-pulse, typically spectrally combining lasers

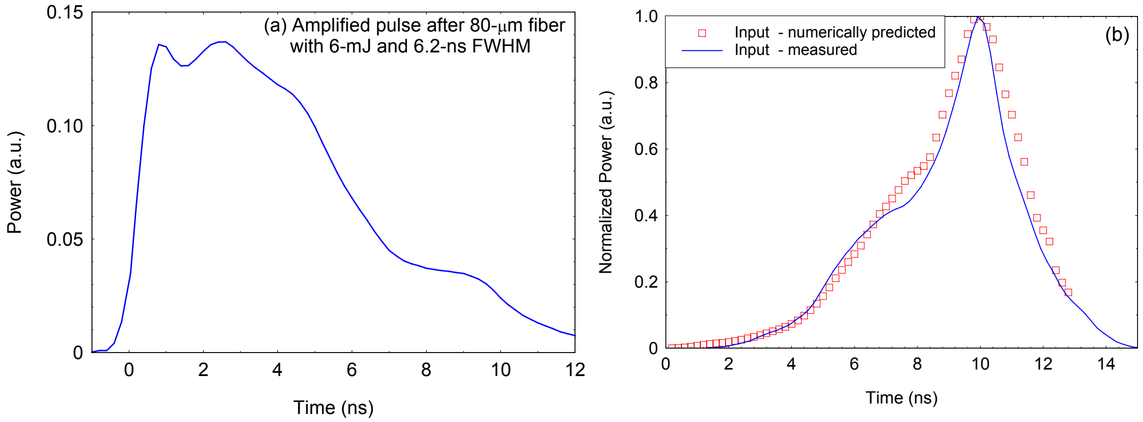

Figure 2.20: (a) Temporal shaped of the amplified pulse after final stage of amplifier, showing reshaping due to gain saturation, (b) Pre-shaped pulse temporal profile from FP seed diode and predicted pulse shape considering cascaded shaping effect for each stage of amplifier

of 532nm and 1064nm at a low repetition rate [32, 105], or employing polarization beam combining, along with variable optical delay lines [106]. Such approaches, nonetheless, will increase the complexity and the cost of the system if pre-pulses were necessary to achieve optimum conversion efficiency. Also, the control of the delay and the contrast can only be mechanically adjusted and the amount of delay is limited by the distance of the delay line.

Pre-pulses and main-pulse can be derived from a single laser emitter with our seed driving scheme while having precise control on temporal parameters of both pulses. Two examples of the temporal profiles of pre-pulses, with different delays and peak power contrasts, are shown in Figure 2.21. The contrast ranged from 1:1.27 in (b) to 1:11 in (a), and the delay between the pulses can be freely programmed. More importantly, in the contempt of pre-pulses generation, energies in the main pulses still remain close to $\sim 6mJ$, the same as the highest energy obtained without prepulses. The improvement of the EUV yield with the use of pre-pulses will be discussed later in Section 3.7.2.

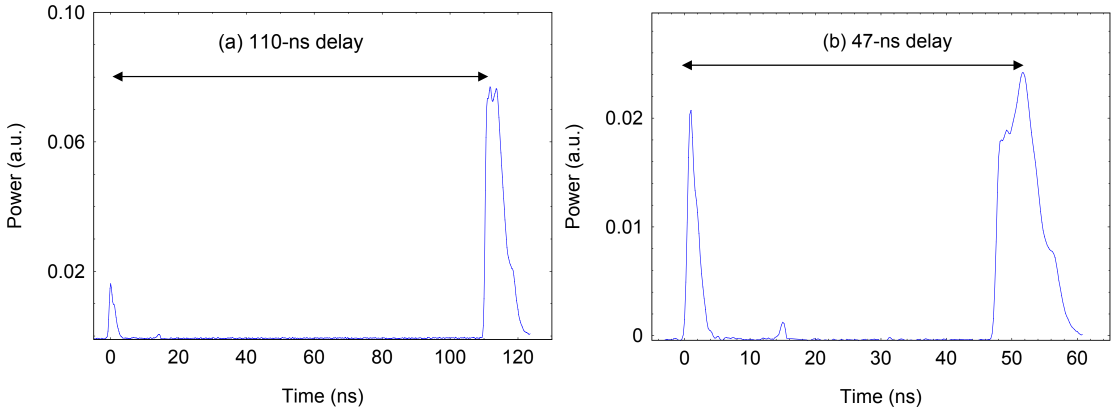

Figure 2.21: Examples of amplified pulse with pre-pulses of different contrast and delay: (a) pre-pulse to main pulse ratio 1:10 with 5.74 mJ in the main pulse, (b) pre-pulse to main pulse ratio 1:1.27 with 5.58 mJ in the main pulse.

2.6.2 Energy Extraction

In addition to saturate gain, another physical implication of the saturation energy is associated with the maximum available energy from an amplifier. Assuming an input pulse strong enough to completely saturate the initial inversion, the available energy from an amplifier is given by [63],

$$E_{available} = E_{sat} \times \ln G_0 \tag{2.18}$$

This equation gives extractable energy from the 80-μm-core fiber is $\approx$ 8.29 mJ with the measured G_0 of 20 dB. To increase the energy extraction, one can optimize the small signal gain of the amplifier or increase the saturation energy by increasing the core size, or decrease the core-signal overlap. Another possible approach is to engineer the doping profile of the core by, for example, confined doping (Figure 2.6), or ring-doping [73].

To better understand the energy extraction, we applied Equation 2.17 to a triangular pulse with varying small-signal-gain and saturation energy to study the differences in output energy and shape (Figure 2.22). The numerical analysis indicates

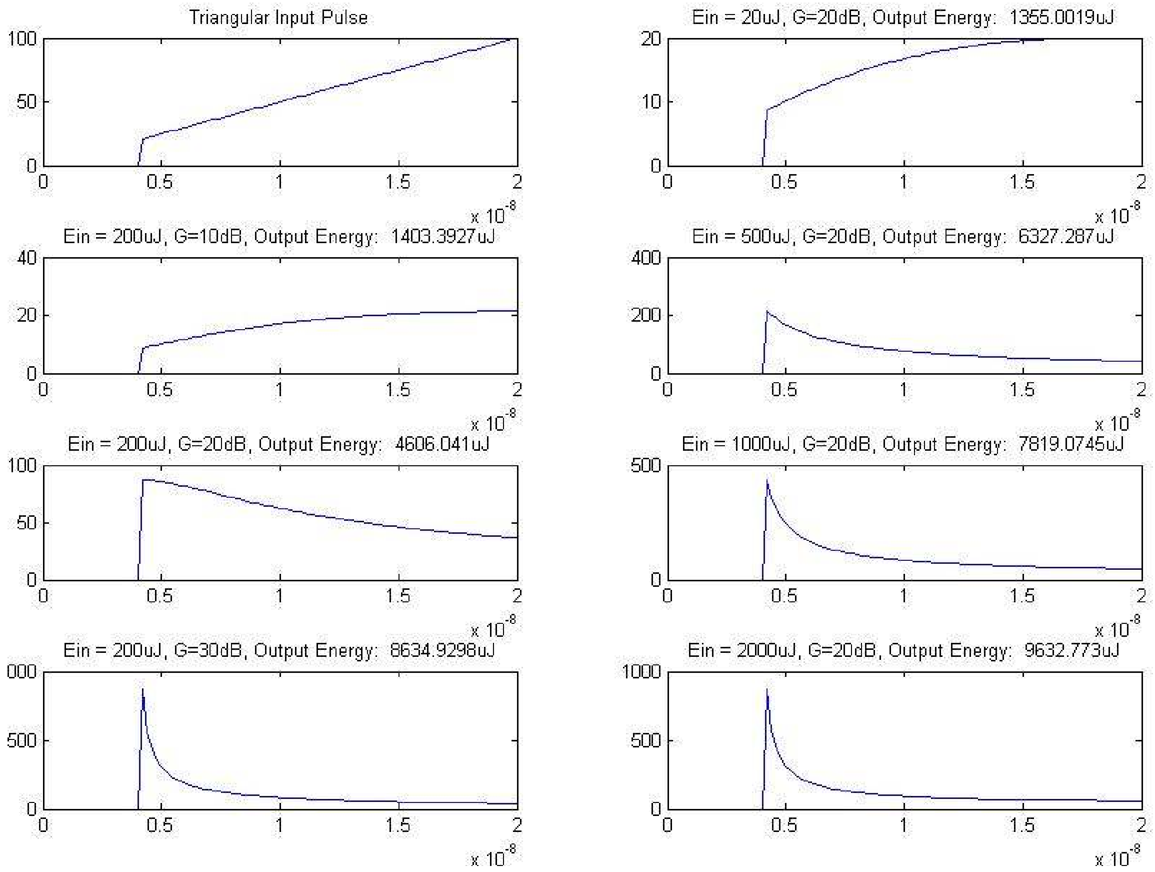

Figure 2.22: Investigation of pulse shape and output energy with an triangular input pulse varying input energy and the gain with the saturation energy 1.8 mJ. Obviously, high gain and high input energy are required for high energy extraction but at the expense of severe pulse deformation and low overall gain.

that the energy extraction is independent of the pulse shape but only dependent on the input energy and the small signal gain G_0 for the same E_{sat} assuming no trigger of nonlinearity. In fact the energy extraction can be characterized by the Frantz-Nodvick model [107]:

$$J_{out} = J_{sat} \log\{G_0[\exp(J_{in}/J_{sat}) - 1] + 1\} \tag{2.19}$$

where J_{out} and J_{in} are the output and input energy fluences.

We plotted the measured input and output energies at various pulse durations and with various waveforms in Figure 2.23, comparing the Frantz-Nodvick predictions.

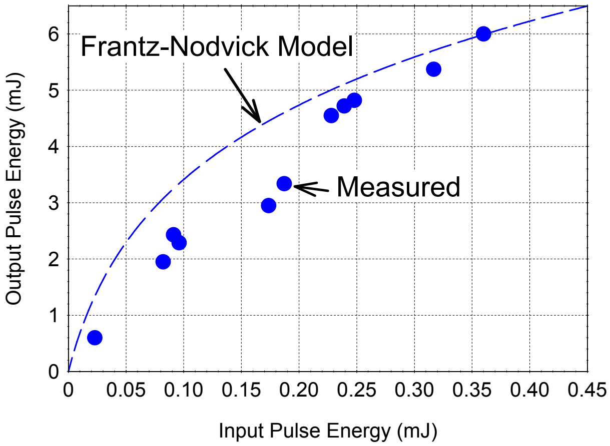

Figure 2.23: Frantz-Nodvick (dashed curve) showing a good fit to the experimental data (solid bullets) for various pulse energies. It is interesting to note that even though the input pulse shape for each measured data point is not identical but the extracted energy is only dependent on the input energy as modeled by Frantz-Nodvick. The only marginal difference at lower input pulse energy is due to squared seed pulses, being easier to amplify beyond the critical peak power of SRS. Therefore, further energy extraction inside the 1064-nm signal is impeded due to the trigger of nonlinear threshold.

The general trend for measured energy extraction as a function of input energies showed good agreement with the trend predicted by the Frantz-Nodvick model. A minor discrepancy occurs for input energies smaller than 0.2 mJ, where the amplifier is seeded with squared input pulses. All the energies recorded are SRS limited and Figure 2.23 clearly shows that the energies extracted using square-pulse input

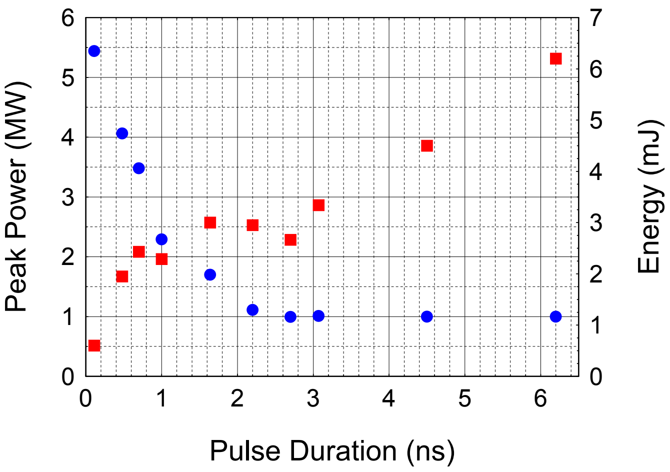

Figure 2.24: Amplified peak power (round bullets) and energy (square bullets) at pulse durations from 0.11 ns to 6.2 ns using the 80-μm-core fiber. A record high peak power close to 6 MW is reached using 0.11 ns by gain-switching pulse. Longer pulse duration up to 6 ns extracted 6 mJ of energy from the fiber, an energy that is more than three time of the saturation energy. All the amplified pulses measure here is limited by the trigger of Raman scattering. The laser is operated at a repetition rate of 50 Hz for the energy and peak power scaling study

are marginally lower than predicted by the Frantz-Nodvick model since the leading edge of the pulse reaches SRS threshold quickly and transfers energy into Stokes wavelengths. With the pulses generated by AWG, as shown in the last five measured data points in Figure 2.23, the amplified energies coincides better with the prediction from the model.

2.6.3 Energy and Peak Power Extraction Results from the 80-μm-core fiber

To summarize the peak power and the energy extraction results of the 80-μm-core fiber from Section 2.5 to Section 2.6.2, Figure 2.24 plots the experimental results of peak powers (round bullets) and energies (squared bullets) for pulse durations between 110ps and 6ns.

Maximum peak powers were limited in this configuration by the onset of the stimulated Raman scattering. Peak power close to 6 MW was obtained at the shortest pulse duration of 110 ps by gain-switching the FP diode. This peak power, in fact, is the highest peak power achieved from a pulsed-fiber amplifier to date. Peak powers were all accurately determined using measured pulse shape and measured pulse energy. Some apparent discrepancy between peak powers and energies is simply relate to the shape (different amount of energy in the pulse “tail”) of the different-duration pulses. Despite very high peak powers for pulse durations under 1 ns, we have not yet observed any core damage or change in the beam output divergence due to the nonlinear Kerr effect as described in Section 2.5.1.

Pulse energy generally increases with pulse duration. Square pulses were used for amplified pulse durations up to 1.7 ns, and pulse shaping by multiplexing two squared-pulse drivers, or by an AWG were used to generated longer amplified pulses. Arbitrary waveform generation can optimize energy extraction by tailoring output pulses to alleviate nonlinear effects. Pulse shortening was observed for energies exceeding the saturation energy of ~ 1.8 mJ for this fiber. Seeded with the slow-rising leading edge shown in Figure 2.20(b), we can compensate the gain saturation effect and produce a triangular pulse shape (Figure 2.20(a)) with energy up to 6 mJ per pulse, more than three times of the saturation energy while maintaining $\approx$ MW peak power. Although operated under saturated region, we are still able to retain a 13-dB gain while extracting 72% of the available energy from the last stage amplifier.

Measured peak powers and pulse energies are consistently below the experimentally measured fused silica bulk damage threshold data as reported in [108]. Table 2.3 compares measured energy fluences at different generated pulse durations from the 80-μm-core LMA fiber amplifier and the corresponding estimated bulk damage thresholds deduced from the data reported in [108]. Recorded energies are three to five time below the bulk damage threshold of fused silica. Note also that potential detrimental effects of modal-area reduction in bent LMA fibers [109] in the critical high-peak power path sections were avoided by using counter-propagation between the pump and signal beams in the high energy amplification stage and by leaving sufficiently long leads at the amplifier output that is only loosely coiled (typically 20 to 40 cm long).

Pulse Duration	Peak Power	Energy Fluence (MFD=60μm)	Bulk Damage threhold [108]
1ns	2.12 MW	97 J/cm^2	330 J/cm^2
0.7 ns	3.4 MW	84 J/cm^2	273 J/cm^2
0.48 ns	4 MW	68 J/cm^2	226 J/cm^2
0.11 ns	6 MW	23 J/cm^2	108 J/cm^2

Table 2.3: Energy fluencies at different generated pulse durations.

2.6.4 Air-breakdown Demonstration

As an additional, although an approximate experimental verification of achieved peak powers, we produced laser-pulse induced atmospheric breakdown with focused high peak power pulses. A particular interest of laser induced gaseous sparking is motivated by laser ignition of engines of special types in which an electrical igniter is a limitation, for example, large stationary gas engines used for power generation and natural gas compression [110]. A focused intensity in the range $\approx 200GW/cm^2$ is required to initiate the atmospheric breakdown, using ns-pulses [111]. This intensity level is easily achievable by a solid-state laser, yet, none of the ns-pulsed fiber laser to date had the capability to induce breakdown in the ambient air, since the output beam are not able to focus down to such a high intensity.

Enabled by the record-high peak power and near-diffraction-limited beam quality from the 80-μm-core amplifier, we conducted the air-breakdown experiments, for the first time using a fiber laser to the best of our knowledge. The output beam of the laser was first collimated by a set telescope and a focusing lens was ≈ 1 m from the output of the laser, far enough to prevent any possible feedback from the plasma which might possibly lead to the damage of the fiber core. An aspherical lens was used to focus the collimated beam to a small focal spot size ∼17 μm, as measured by the knife-edge technique with ±0.5 μm precision. Two pulse durations of 0.7 ns and 110 ps were tested for the pulse duration dependence on the breakdown threshold. Both durations successfully initiated visible and audible breakdown (Figure 2.25).

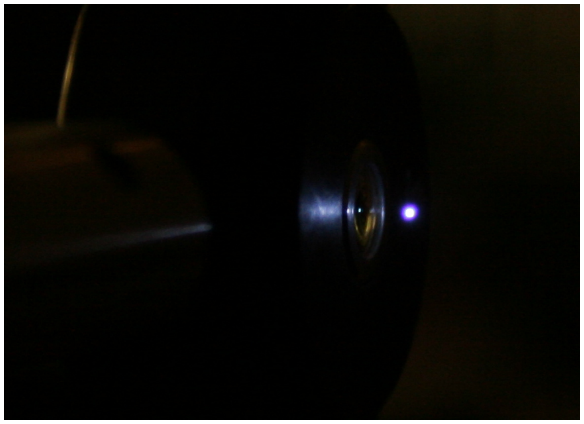

Figure 2.25: A photograph of the atmospheric breakdown initiated by a fiber laser. This indirectly verified the high peak power and the excellent mode quality from our LMA fiber, that allows it to reach record-high intensity levels, demonstrating the first air breakdown by using a ns-pulsed fiber laser

The breakdown threshold, defined as the intensity level at which 50% of the laser pulses induced air breakdown, was measured to be 510 GW/cm^2 for 0.7-ns pulses and 2.5 TW/cm^2 for 0.11-ns pulses. The laser was operating at a repetition rate of 50 Hz, allowing us to manually, and precisely, determine the level of the breakdown threshold.

2.7 Power Scaling and Thermal Management

Intrinsic quantum defect and non-radiative decay are two main contributing sources of heat from a fiber laser [45]. Intrinsic quantum defect is the energy difference between the pump and the signal photons. Taking an example of a 1064-nm signal and a 915-nm pump, the quantum efficiency is 86%, meaing 14% of the energy will become heat lost into the host medium through the nonradiative process. Also, in practice, the quantum efficiency is less than $\lambda_{pump}/\lambda_{signal}$, due to non-zero non-radiative decay rate W_{NR}, contributed from multi-phonon decay, ion-ion energy transfer, concentration quenching, diffusion, and cross-relaxation.

To have a high-average-power fiber laser with a short fiber length operating at high thermal load per unit length, careful analysis and design must be considered to remove the excess heat and to prevent thermal effects including the laser efficiency degradation, thermal lensing, and the damage of the fiber. The rule of thumb for the heat management is to keep fiber core temperature $\sim 162°C$, the temperature corresponding to a 6% drop in the quantum efficiency, due to increase of multiphonon relaxation [45]. Additionally, the polymer entire jacket must be kept below 50 $°C$ to minimize the material degradation of the pump cladding.

To get a general idea how temperature is distributed transversely in the fiber, one can think of the heat source as being located at the center of the core and the heat being transferred from the core to the ambient environment through the mechanisms of conduction (from the core to the cladding, and to the jacket) and convection (from the jacket to the surroundings). Conduction happens in two contacting solid materials, governed by

$$Q_{cond} = \kappa {}^{A}\!/_{L} \Delta T \tag{2.20}$$

where κ is the thermal conductivity in $W/m°C$, A is the contact area , L is the material thickness, and ΔT is the temperature difference. The exchange of heat in outer cladding and the ambiance is through convection,

$$Q_{conv} = hA(T_{air} - T_c) \tag{2.21}$$

where h is the heat convection coefficient

The radial dependence of the temperature in the fiber can be found by solving the Fourier Equation in cylindrical coordinates over the fiber volume [45]:

$$\kappa\{T(r) + \frac{1}{r}\frac{\partial T(r)}{\partial r}\} + Q = 0 \tag{2.22}$$

where Q is the heat dissipated per unit volume (in $Watt/m^3$) and κ is the thermal conductivity in W/m.

The boundary condition of the outer surface in contact with the external thermal reservoir (water or atmospheric air) can be written as,

$$\kappa\frac{\partial T(r)}{\partial r}_s + h(T_s - T_0) = 0 \tag{2.23}$$

where h is the convection heat transfer coefficient and T_s and T_0 is the surface and reservoir (water or air) temperature.

The solutions of for Equation 2.22 and 2.23 for the core, signal cladding and pump cladding are [45]:

$$T(r < R_c) = T_0 + \frac{QR_c}{4\kappa_1}(1 - (\frac{r}{R_c})^2) + \frac{QR_c}{2}[\frac{1}{\kappa_1}\ln(\frac{R_1}{R_c}) + \frac{1}{\kappa_2}\ln(\frac{R_2}{R_1}) + \frac{1}{hR_2}] \tag{2.24}$$

$$T(R_c < r < R_1) = T_0 + \frac{QR_c}{2}[\frac{1}{\kappa_1}\ln(\frac{R_1}{r}) + \frac{1}{\kappa_2}\ln(\frac{R_2}{R_1}) + \frac{1}{hR_2}] \tag{2.25}$$

$$T(R_1 < r < R_2) = T_0 + \frac{QR_c}{2}[\frac{1}{\kappa_2}\ln(\frac{R_2}{r}) + \frac{1}{hR_2}] \tag{2.26}$$

where R_c, R_1, and R_2 are the radii, and κ_c, κ_1, and κ_1 are the thermal conductivities and the subscripts of c, 1, 2 denotes to core, signal cladding (cladding) and pump

Radius	(μm)
core	41
first cladding	200
Jacket	256
Thermal conductivity	$(W/m^{\circ}C)$
Glass (κ_1, κ_2)	1.38
Polymer (κ_3)	0.2
Copper	401
Aluminum	237
Thermal convection coefficient	$(W/m^2 \times^{\circ} C)$
air @ 1 atm	1.38
water	105

Table 2.4: Important thermal coefficient for the system components used in the analysis and system

cladding (jacket) respectively. Table 2.4 summarizes the constant used in the thermal analysis.

One can estimate thermal load per meter using the available pump power, the pump coupling efficiency and the expected slope efficiency. Taking an example of a 630-W available pump power with 74% pump coupling efficiency and 60% slope efficiency, with a 3-m gain fiber, the average heat per unit length is ≈60 W/m, assuming the heat is distributed equally over the entire length of the fiber.

In order to emphasize the importance of cooling arrangement in high-average-power operation, Figure 2.26 plots the transverse temperature distribution under the conditions when (a) the fiber is passively cooled in the air and (b) the fiber is passively cooled in the water, both with an ambient temperature of 25 $^{\circ}C$. Without any cooling, the jacket of the fiber can reach a temperature more than 790 $^{\circ}C$ at this heat density and cooling with water will lower that temperature to $\sim 40^{\circ}C$.

Therefore, one has to implement force cooling in order to operate the fiber below the temperature that will not cause degradation in efficiency.

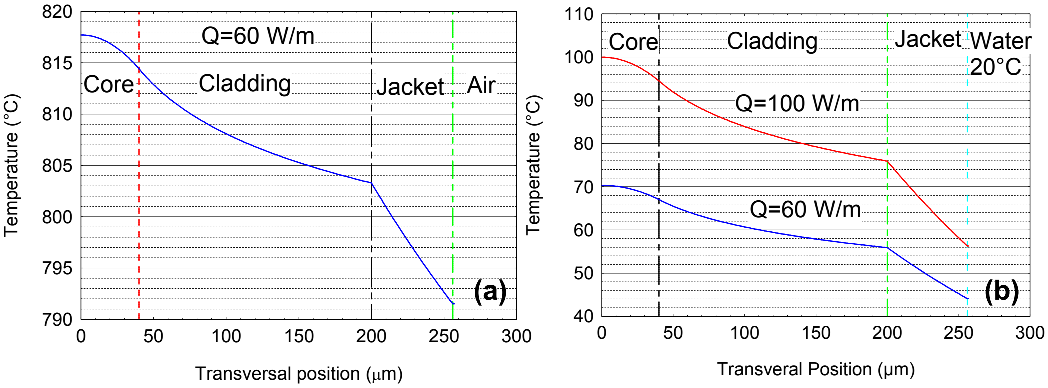

Figure 2.26: Thermal analysis showing the temperature distribution across the fiber for (a) passive air cooling with 60 W/m of heat density and (b) passive water cooling with 60 and 100 W/m heat density. It is discernible that temperature gradient is the highest in the jacket, where the thermal conductivity is the lowest, consequently becoming the highest thermal barrier across fiber. In addition, the passive air cooling will create a temperature discontinuity more than $760°C$ from the jacket to the air, beyond the melting point of the polymer.

In reality while pumping from a single end, the heat load will be more intense at the pump end than at the signal end. Moreover, another heat source comes from the pump light that is not coupled into the fiber end, given the typical pump coupling efficiency is ~72% to 75%. The uncoupled pump light illuminating at the fiber mount will increase the heat load on the end mount, unless it is ameliorated in two ways. One is to introduce an aperture in between the lenses of the pump-coupling telescope to block the outer ring of the pump light, the part not being coupled into the fiber. The end mount surface facing the pump is also polished to increase the surface scattering of the uncoupled pump light, otherwise contributing to the heat.

Heat dissipated along the uncoiled fiber is removed by a two-component TEC cooler (Figure 2.27).

In the first 10 cm near the pump end of the fiber, where the highest heat removal is required, forced cooling is implemented, using two solid-state heat-pumps (ther-

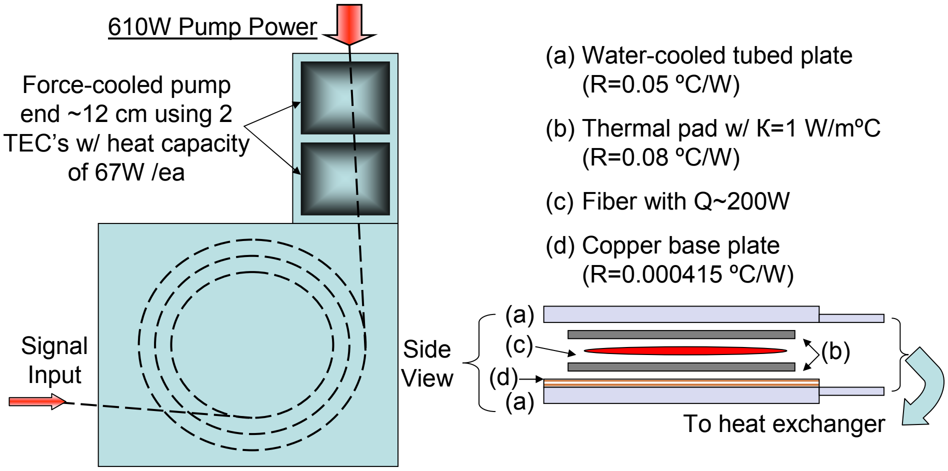

Figure 2.27: Heat removal arrangement on the left showing two cooling areas. The first 10 cm of the fiber at the pump end is actively cooled with two TEC's, each with a 67 W of heat capacity, with its temperature set to $15°C$. The rest of the fiber is packaged in thermally conductive materials, allowing temperature difference as small as $\Delta T = 13°C$ from the heat sink to the fiber jacket outer surface.

moelectric coolers or TECs), with a total of 134 W of cooling capacity. The TECs are controlled with an active feedback-controlled current source, with the temperature set at $\sim 15°C$, higher than the dew point temperature to avoid condensation of water vapor on the fiber.

Even water-cooling the fiber could provide sufficient cooling, there are technical difficulties for implementation. Therefore, the remaining part of the fiber is carefully packaged in tubed-plates as shown on the right of Figure 2.27. The tubed-plates serve as a heat exchanger for the active fiber which was cooled by an external liquid coolant exchanger. An analysis, using the thermal conductivities of each layer and Equation 2.20, predicted that a thermal difference as small as $\Delta T = 13°C$ across the fiber jacket to water temperature can be achieve with this arrangement, assuming a total of 200 W of heat is generated from the fiber. Compared to water cooling as shown in Figure 2.26, where the temperature difference from jacket to the reservoir is $26°C$, the arrangement shown in Figure 2.27 has a better thermal performance presuming no air gaps are allowed during packaging.

The extraction of the average power is strongly related to the seed power. The slope efficiencies of the amplifier as a function of seed power are plotted in Figure 2.28.

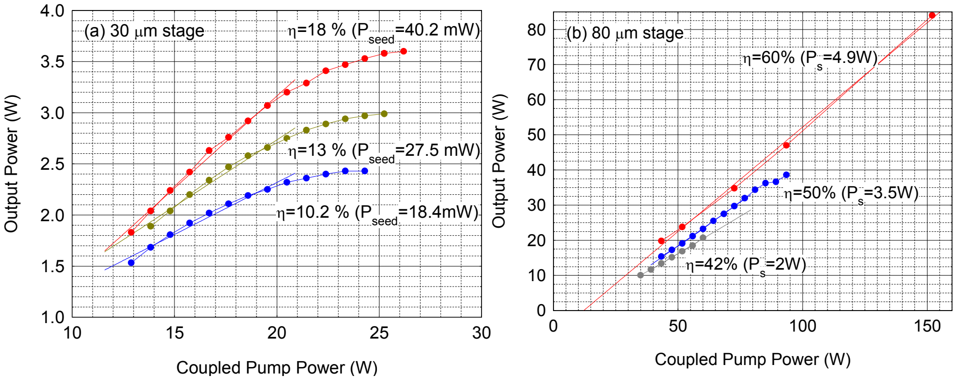

Figure 2.28: Study of the required seed power for the optimal slope efficiency for the (a) 30-μm-core stage and (b) 80-μm-core stage. Both power amplifier stages showed an increase in slope efficiencies with increased seed power.

The slope efficiencies of the 30-μm-core stage are lower, in the range of 10 $\sim$ 18%, due to seed powers limits on the order of tens of mW's, which a much more efficient extration can be achieved in the 80-μm-core stage, provided with a few Watts of seed powers. Based on the above observations, it is essential to provide a sufficient seed power to compensate the power lost due to coiling, as described in Section 2.4, and also to have good extraction of the stored energies. The highest average power we achieved is 140 W, operating at a repetition rate of 500 kHz, with 9W of seed power (Figure 2.29). The output is limited due to the degradation of the polymer coating, available from the fiber manufacturer.

With 630 W of available pump power, 72% coupling efficiency and 65% demonstrated slope efficiency (Figure 2.29), average power $\sim$288 W can be expected with improved polymer coating applied during the manufacturing process.

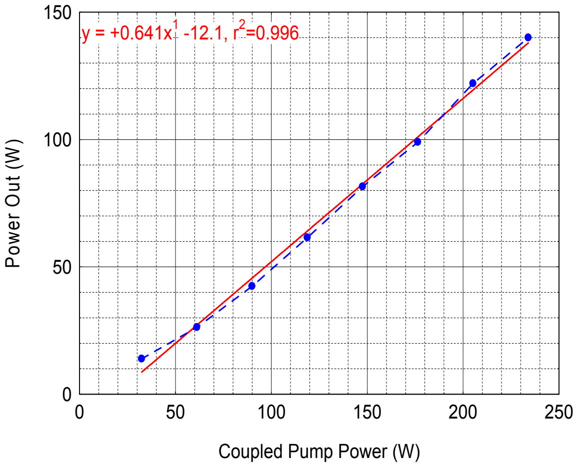

Figure 2.29: Power scaling of the system reached an average power of 140 W operating at the repetition rate of 500 kHz with a seed power of 7.3 W, yielding a slope efficiency of 64.1%. Power is so far limited by the degradation of the polymer coating. With coating with lower heat-induced degradation, average power up to 288 W is expected with available pump power.

2.8 Conclusion

A pulsed fiber-laser driver producing high peak powers, high energies, high beam quality, and controllable pulse parameters is developed to the study EUV generation. Careful selection of the core enables megawatt-level peak powers in nanosecond-pulse-duration region while maintaining a mode quality close to that of a single-transverse-mode. A record-high peak power close to 6 MW using 110-ps gain-switched pulses is reported and > 6 mJ pulse energies with 6-ns durations, giving > 1 MW peak power, is also achieved. Regardless of the large mode area of 2750 μm^2, scrupulous mode-matching and tight fiber-coiling provide an excellent mode quality of $M^2 \approx 1.3$.

A numerical simulation adapting the FFT-BPM technique to study of the Kerr-nonlinear-effect implies that a change in the divergence of the beam will occur even at peak powers a few times lower than the critical peak power for self-focusing. However, no experimental evidence is reported to date though peak powers close to the self-focusing limit with diffraction-limited beams have already been reported by several groups. Adapting an arbitrary-waveform-generator seeder enables active pulse temporal-shaping including the generation of pre-pulses under the saturated gain region of the cascaded fiber amplifiers. This instrumental tool allows us to study the pulse shaping that occurs during the passage of the pulse in a saturated amplifier. The experimental results coincided well the numerical results predicted from the Frantz-Nodvick model.

High average-power extraction while maintaining MW peak powers at the same time requires very high thermal-dissipation per unit length, since the fiber length has to be kept short to avoid nonlinearity. Forced-cooling, implementing both the solid-state heat pumps and the water-cooled heat exchangers, is designed and analyzed numerically. An average power up to 140 W is measured at the laser output with this cooling arrangement and further power scaling is possible to hundreds of watts by increasing the repetition rate of the system and the pump power. Conclusively, the SEFIM can provide a peak power and a mode quality to reach the required intensity, along with the average power, providing the parameters needed for a high-power EUV source. Still, experimental verifications on the targets need to be investigated, as will be described in the chapter III.

CHAPTER III

Feasibility Study of High Power Fiber-laser-driven EUV Generation

This chapter describes two feasibility experiments for fiber-laser driven EUV generation. Section 3.1 provides background information on laser EUV generation. The subsequent sections 3.2 to 3.4 describes experiments in which the fiber laser system irradiates a bulk solid-Sn target operating and this experiment demonstrates the first EUV generation by a fiber laser.

Sections 3.5 to 3.7.3 describes the second experiment, performed in collaboration with the University of Central Florida. In this experiment, a droplet target capable of high-repetition rate operation is fired at a rate of 1.75 kHz. The purpose of this experiment was to demonstrate high-efficiency EUV generation using a power-scalable and low-debris target, required for a production-worthy EUV source.

3.1 Introduction for laser-produced plasma EUV generation

For years, researchers have been searching for a suitable source for next-generation lithography. Due to the limited working wavelength of multilayer reflective optics in the EUV region (13.5 nm for Mo/Si mirrors), it is necessary to find an efficient light source producing strong emission in the reflection bandwidth of available optics. Nd:YAG lasers at Joule-level energies have been the preferred lasers for generating

13.5-nm EUV [2, 27, 28, 29, 30, 31, 32, 33]. Studies of efficiency versus pulse duration for these lasers have been conducted [112, 113, 31], generally finding that nanosecond range pulses yield the best results of a $\sim 2\%$ conversion efficiency (Table 1.4). Pulsed CO_2 lasers have also received much attention lately due to their relatively high efficiencies of approximately 4.5% [30, 114]. With average powers around ≈ 5 kW [24, 114, 115], CO_2 lasers show much promise for EUV generation. However, they suffer from a low wall-plug efficiency (a few percent), resulting in higher operational costs. In addition, there are thermal dissipation issues that need to be resolved.

Various targets have been researched for EUV generation. These include high-density solid targets (tin or frozen xenon), liquid jets (tin or xenon) [116, 117], and droplets (tin, tin-doped water, or pure water) [114, 113, 118], quasi-mass limited (thin layer) [119, 120, 32], laser punch-out [121, 122]. Water targets were studied as one of the earliest target source in the form of liquid jet, liquid droplet, and solid [1] and attracted many attentions in the early years due to it low cost and low contaminaiton on collector optics. However, lack of strong emission line in the Mo-Si reflection band (Section 1.3.1) limits its applicability as an efficient source material [123]. Only up to 0.4% of conversion efficiency can be realized even after shifting the central wavelength of Mo-Si mirrors from 13.5 nm to 13 nm.

Lithium has a very sharp emission line at 13.5 nm and is regarded as one of the most efficient EUV sources [124, 116, 27]. Conversion efficiencies of up to 2.2% from a planar solid lithium target has been demonstrated by George *et al*. [27] with a laser intensity of $6.6 \times 10^{10} W/cm^2$. However, its demonstrated efficiency is still lower than that of solid-tin ($\approx 4.5\%$) and debris issue from a solid lithium target still prevents it from being used for the lithography light source.

Xenon (Z=54), usually in liquid jet form, is one of the most commonly used EUV source materials due to its being a clean LPP source [125, 117, 126, 25]. The main drawback of Xe is the lack of efficiency, limited to about 0.8% at present [25]. This is because Xe has a much stronger unresolved transition arrays (UTA) located at 11 nm (with emissions from states Xe^{+6} to Xe^{+14}) with a less efficient emission band at 13.5 nm (Xe^{+10}).

Tin (Z=50), another very commonly used source for EUV generation, has nearly all species from Sn^{+7} to Sn^{+14} contributing to the in-band emission at the optimum plasma temperature ($\sim 30eV$). Efficiencies of up to 5% have been reported using solid tin targets [2, 27].

UTA in tin arise primarily due to the transitions of $4p^6 4d^N \rightarrow 4p^5 4d^{N+1} + 4p^6 4d^{N-1} 4f$ from Sn^{8+} to Sn^{11+} overlapping in energy [127]. The mechanism coupling the laser energy to the plasma is inverse Bremsstrahlung absorption [5], in which the electrons oscillate in the presence of the laser's electric field and collide with the ions to which the photon energy is transferred. The atomic processes in a hot plasma are quite complex, and in the simplest terms, radiation emitted from the relaxation of these highly ionized materials comes from two processes: free-electron-ion interaction and bound-bound transition of the ions. Bremsstrahlung from free-electron-ion interaction occurs when the passing electron is accelerated by an ion, causing it to radiate a broad continuum, with the spectrum closely related to the electron velocity. The process of bound-bound transitions of the ions in different ionization states yields very narrow emission lines.

The critical parameters for the radiation, which are the electron temperature and density, are determined by the target material and laser parameters. Rigorous simulations with hydrodynamics codes show that the highest electron temperature is in the region where the electron density is below the critical density at which the driving laser light resonates with the plasma [2].

3.2 First Demonstration of Fiber-laser-driven EUV Generation with Solid-Sn Target

Even though EUV had been generated for few decades with synchrotron source, electrical-pinched plasma and laser-produced plasma, EUV generation from a fiber-laser produced plasma (FLPP) was not thought possible due to its lower achievable pulse energy and intensity in the ns-pulse duration. Therefore the principle motivation of this study is to demonstrate the generation of EUV exploiting the state-of-the-art ns-fiber laser system.

3.2.1 Laser Parameters for Solid-tin Experiment

In this set of experiments, the output from a fiber laser, with either a 115 μm or 200 μm core power amplifier, is focused onto a solid-Sn target. The complete set of parameters are shown in Table 3.1. Since no seed pulse pre-shaping was implemented at the time, the square pulse exhibited strong deformation. Therefore, the peak power must be calculated using Equation 2.5.

3.3 Experimental Setup for Solid-Sn EUV Generation

The output beam of the fiber laser is delivered to the target chamber through two sets of telescopes to control the beam divergence. 70% of the laser energy is transported from the output onto the target due to clipping losses in beam delievery and the uncoated chamber window and focusing lens. The EUV target chamber is shown in Figure 3.1.

The laser beam was expanded and collimated by a telescope before the entrance port of the vacuum chamber with a $1/e^2$ beam diameter of $\approx 17mm$ on the focusing lens. The focusing lens was a 50 mm (f/2) achromatic lens which gives an effective

Fiber type core/cladding diameter	115/350 μm	200/600 μm
Amplified Energy @fiber output	3.5 mJ	6 mJ
Seed pulse duration	12.5 ns	100 ns
Amplified pulse duration (FWHM)	5 ns	6 ns
Peak power (by integration)	700 kW	514 kW
M^2	10.5	17
Smallest Spot size on target $1/e^2$ in diameter	48 $\mu m\times$ 75 μm	61 $\mu m\times$ 77 μm
Highest intensity on target (accounting to 30% loss in delivery)	$1.2 \times 10^{10} W/cm^2$	$6.5 \times 10^9 W/cm^2$
Repetition rate	50 Hz	50 Hz

Table 3.1: Summary of laser parameters used in solid-Sn target experiments

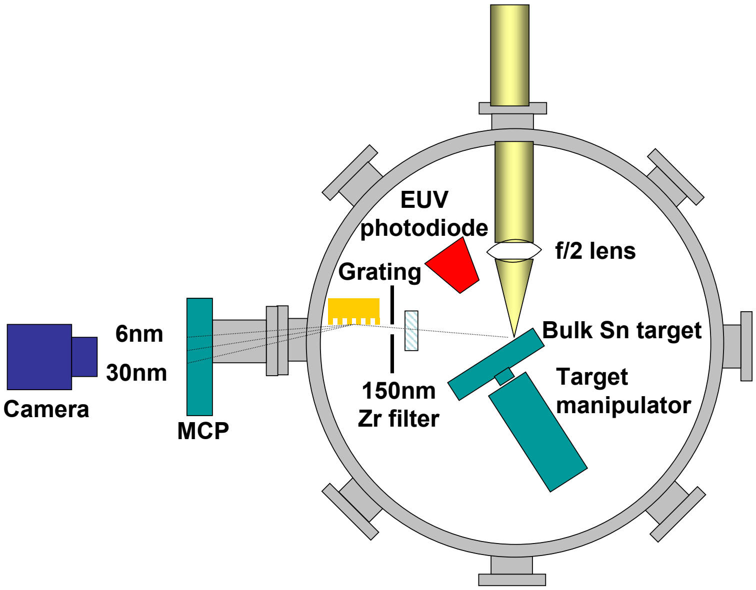

Figure 3.1: EUV-generation setup using solid-Sn target. The target is located in the center of the chamber and controlled by a mechanical target manipulator. The focusing lens used is a 50-mm achromatic lens with a 1-inch aperture. Diagnostics tools consists of a custom-designed EUV detector, mounted along the normal of the solid-Sn target. EUV spectrometer is also set up to monitor dispersed EUV emission from 6 nm to 30 nm.

f-number of ≈ 3. The focusing lens was also covered by additional pellicle membrane to prevent debris deposition on the focusing lens.

The focal spot size was measured by a knife edge measurement with an accuracy of ±500 nm. The smallest measured spot size was $\sim 60\ \mu m\ 1/e^2$ diameter, corresponding to a highest intensity on target of $1.2 \times 10^{10} W/cm^2$ with 0.5 MW of peak power delivered to the target. The incident angle on the target was 45°, and the target is mounted to a motorized translation and rotational stage, which is externally controllable outside the vacuum chamber. A fresh target is obtained for every shot by rotating the target. The wobble from the rotation is kept well below the Rayleigh range.

A custom-made EUV photodiode was placed 12 cm away from the plasma along the normal direction in the target surface. A copper plate for ion energy measurements (not shown in the Figure) was also implemented also along the normal direction of the target surface. The grating spectrometer was set up in the same vacuum chamber to monitor the dispersed EUV light from 6 to 32 nm with a zirconium (Zr) filter in the front of the grating to block the scattered laser light from reaching the highly sensitive multi-channel-plate (MCP).

The vacuum level is maintained at a level of 4×10^{-6} Torr for safe operation of the multi-channel-plate by a turbo-pump and backed up by a roughing pump.

3.3.1 EUV Diagnostics

The standard diagnostics for EUV generation studies include an EUV spectrometer, which covers the emission band from 5 to 40nmm to study the contrast of emissions from various states. This gives an estimate on the plasma condition, i.e. the plasma temperature.

The EUV spectrometer as shown in Figure 3.2 consists of a Hitachi spherical grating with a variable line-spacing centered at 1200 lines/mm to correct for aberration, placed at a grazing incident angle of 87°. The cylindrical grating gives a flat field image on the image plane, thereby eliminating distortion. The point source, the laser produced plasma, located 235 mm from the center of the grating is imaged onto the multi-channel-plate 237 mm away from the center of the grating. To prevent stray light from reaching the multichannel plate, the grating is surrounded by an optically opaque compartment, and a 250-nm thick Zr filter is place between the plasma source and the grating to block out everything outside the EUV band. We also installed a dipole magnet in front of the Zr filter to deflect energetic ions which could damage the thin filter. The spectral images are calibrated with the calculated geometry of the image, and by an aluminum filter, having very sharp cutoff edge at 17 nm.

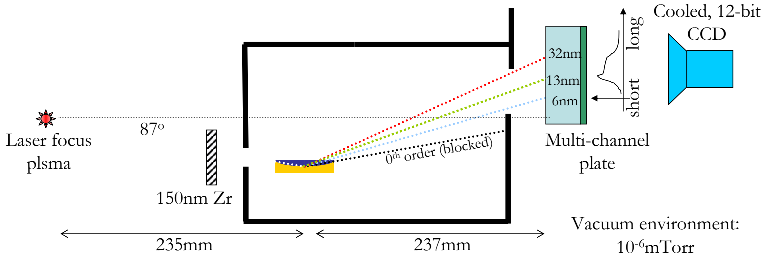

Figure 3.2: EUV spectrometer consisting of a spherical grating with 1200 lines/mm, placed 235 mm away from the laser-produced plasma. A flat field image is produced by a multi-channel plate with a spectral range from 6 nm to 32 nm and the image is taken by a CCD camera. A Zr filter with FWHM bandwidth from 6.5 nm to 18 nm improves the image spectral purity.

A light buffer is also placed in front of the MCP to block the zero order reflection so only the radiation from 6 to 32 nm is transmitted. A 12-bit TEC-cooled low noise CCD camera images the phosphor side of the MCP.

A calibrated EUV energy meter made specifically for the purpose of EUVL source measurement, consisting of spectrally selective components that measure only the emission inside the Mo/Si mirror bandwidth is usually implemented along with an

EUV spectrometer to measure the efficiency. Details the setup of both diagnostics will be discussed. The custom-made EUV detector sit in an aluminum housing is shown in Figure 3.3.

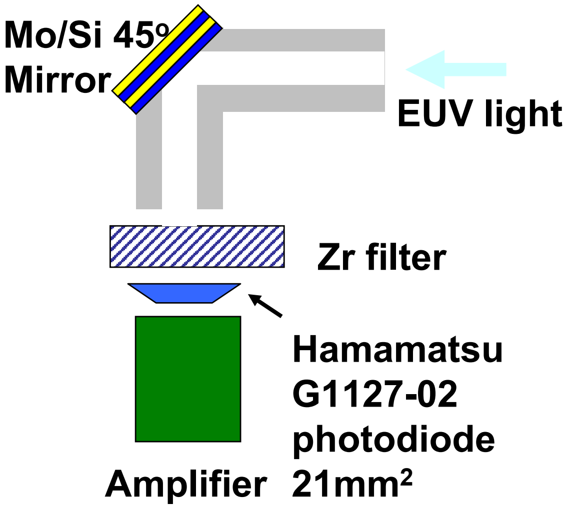

Figure 3.3: Custom designed EUV detector to measure the emission only in the working wavelength of Mo/Si mirrors. It consists of a Mo/Si mirror and a Zr filter for spectral selection. A large area photodiode, in which the signal is amplified by a transimpedance amplifier, detects the EUV emissions.

A 45° Mo-Si multilayer mirror with a 4% bandwidth is used to reflect the EUV emission from the plasma. Since the Mo-Si mirror is highly reflective for UV/VIS/IR, another 150 nm thick Zr filter is used to block the radiation outside the EUV band. The 4% inband emission centered at 13.5 nm is then detected by a Hamamatsu G1127-02 photodiode.

This Schottky diode originally intended for blue-UV detection possesses high quantum efficiency (about 10 electrons per photon) in the EUV wavelength. To improve the diode sensitivity, a transimpedance amplifier is mounted inside the casing. The diode has an area of detection of 21 mm^2 and has a long rise time of 300 ns.

3.4 Experiment result using solid Sn target

The image of the MCP and the corresponding spectrum for the best EUV yield are shown in Figure 3.4. The top image is the MCP, with the arrows indicating the calibrated spectral markers. The corresponding spectrum is shown below. The emitted spectrum has a broad peak around 13.5 nm. The Mo/Si reflection band is shown in the shaded area.

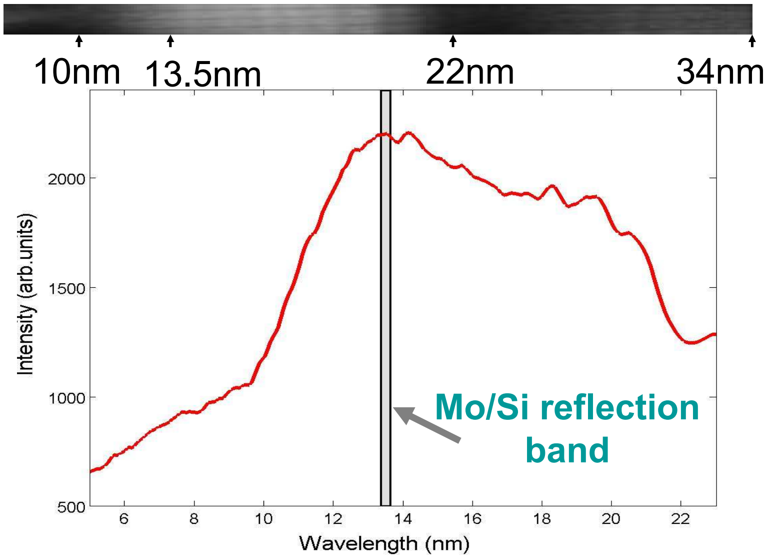

Figure 3.4: EUV spectrum from the solid-Sn target showing a strip of the MCP image on the top with calibrated markers and the corresponding spectrum plotted from 6 nm to 22 nm on the bottom. Gray shadow indicates the narrow bandwidth of Mo/Si multilayer mirrors.

Compared to the published literature [27], our spectrum shows similar spectral features with a lower contrast of the 13.5-nm peak to the background due to the available intensity of $1 \times 10^{10} W/cm^2$. Better contrast can be anticipated with improved laser intensity as discussed in Section 2.6.4.

For the measurement with the EUV photodiode, the optimal in-band EUV signal is plotted in Figure 3.5. Two curves shown in the plot are measured with different detector conditions. The curve with higher amplitude was measured with the 45° Mo/Si mirror removed from the housing and the detector directly facing the LPP

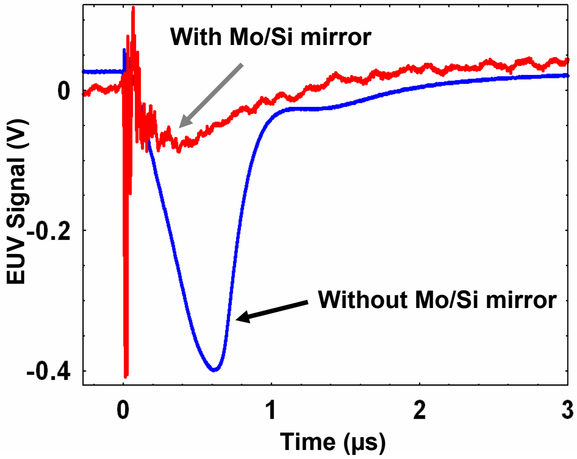

Figure 3.5: Oscilloscope trace of the EUV photodiode for the optimal EUV yield showing the higher amplitude curve, taken without Mo/Si mirror, and lower-amplitude curve, taken with Mo/Si Mirror.

EUV source. This curve shows all of the radiation inside the transmission band of the Zr filter (FWHM 6.5 nm to 18 nm). The lower-amplitude curve is taken with the Mo/Si mirror in place, meaning only light inside the 4% of the Mo/Si bandwidth reaches the photodiode.

After the experiment, the photodiode was calibrated with a EUV source with known energy with the help of Cymer Inc. The well-characterized source is a xenon discharge plasma with an energy of 24 mJ in a 2% bandwidth in 2π sr. The photodiode signal for the Xe source is shown in Figure 3.6.

By comparing the distance from the source and the integration of the detector signal for Figure 3.5 and Figure 3.6, we find our EUV energy to be $\approx 3\ \mu J$ per pulse, assuming isotropic emission into 2π sr. This implies a conversion efficiency of 0.9%. Also, the isotropy of the radiation is also verified from 5° to 85° off of the target's normal. The EUV signal shows a standard deviation of $\sigma = 7.5\%$ of the mean value.

Concerns of energy of debris from the bulk Sn target are also addressed by a time of flight experiment. The Faraday cup detector with a 2 cm diameter copper plate is placed 9 cm from the plasma on the normal of the target plane. The signal is shown

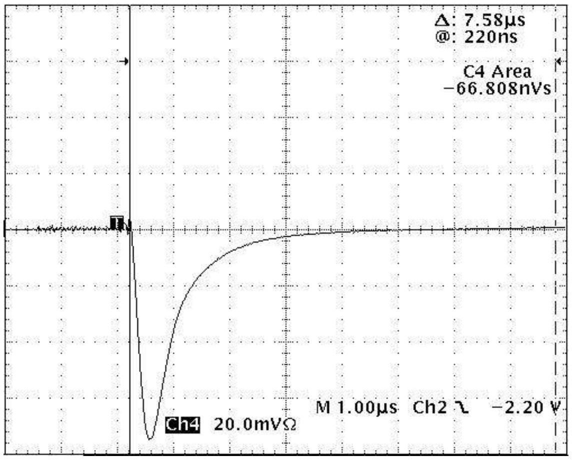

Figure 3.6: EUV photodiode signal for calibration, taken with a 24-mJ Xe-DPP source at Cymer, Inc.

in Figure 3.7.

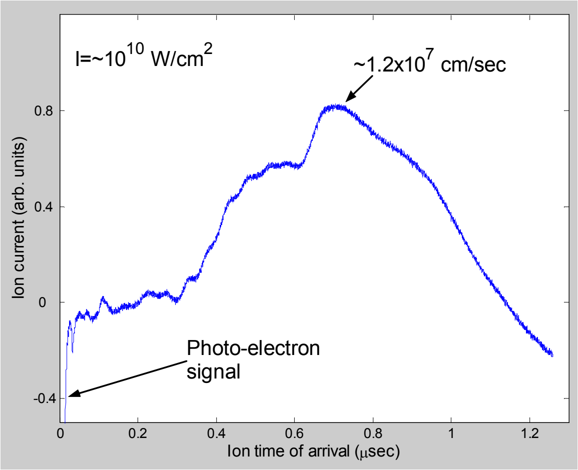

Figure 3.7: Time of flight measurement showing that the ion speed is on the order of 10^7 cm/s corresponding to several KeV. Energetic ions contaminate the focusing lens and EUV collector optics, so a mitigation scheme is highly desirable.

The ions speed is extracted from the distance and time delay between the photoelectrons signal and the peak of the ion signal (around 0.8 μs), as shown in the plot. The energetic ion speed is calculated to be around 10^7 cm/s, corresponding to several keV of energy. Such high energy ions present a enormous threat for the collector optics as well as the focusing lens.

We had demonstrated, to the best of our knowledge, the very first EUV generation from a fiber-laser-produced plasma using a solid-Sn target. Conversion efficiency of 1% is reported, limited by the highest intensity available from the fiber-laser at the time. Further improvement on the laser intensity and choice of a practical source is necessary for an high-power efficient long-life-time EUV source.

3.5 Practical High-power FLPP EUV Source Development

Previous successful demonstration with a solid-Sn target opens up the pathway for fiber-laser drivers as candidates for laser-produced-plasma EUV generation. As previously explained, solid-Sn targets become impractical for high power EUV sources for two reasons: their generation of excessive debris and their lack of high repetition capability.

It is observed from the previous experiment that Sn debris from high speed Sn-particles coated the focusing over thousands of shots, and these undesirable byproducts coat the multilayer mirrors and reduce the collector lifetime. Cleaning or replacing the optics results in a huge penalty on the cost of operation. Moreover, solid Sn targets are controlled by motorized target manipulators, which limits their highest repetition rate to hundreds of Hz. In order to meet the power requirements for high volume manufacturing (Section 1.3.3) with pulse energies of a few mJ (limited by the small transverse core size of fiber gain media), it is necessary to operate at repetition rates in excess of 100 kHz. Both issues mentioned above can be effectively addressed with the development of mass-limited droplet target dispensers.

The previous experiment with a solid-Sn target yielded a lower conversion efficiency compared to published results with the same target [27, 28, 29, 30, 31, 32, 33] due to the peak intensity on the target on the order of low $10^{10} W/cm^2$. Figure 3.8 plots the intensity dependence of the conversion efficiency with Sn-doped droplet targets versus intensity.

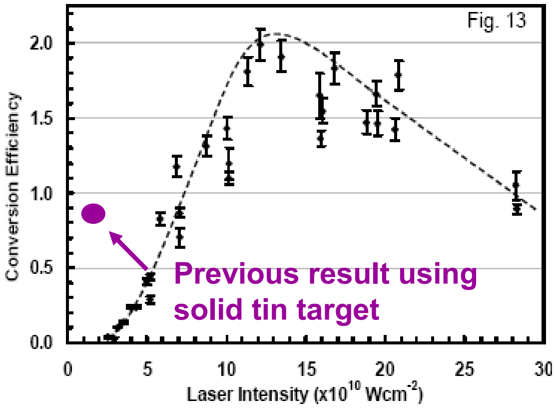

Figure 3.8: Conversion efficiency plotted against intensities for the solid-Sn target. The data shows optimal CE for intensities on the order of $10^{10} W/cm^2$.

With the development of high energy laser systems with nearly diffraction-limited output beams from 80-μm core fiber (Section 2.3), the intensity required for efficient EUV generation can be reached. However, since the efficiency of in-band EUV generation of laser-produced plasma is highly dependent on the plasma conditions [2], which in general are complex functions of laser parameters such as intensity, duration, pulse temporal shape, energy, spot size and wavelength, the suitability of fiber lasers for achieving efficient EUV generation with realistic droplet targets was an open question.

3.5.1 UCF Sn-doped Water Droplet Targets

Many different types of targets are being developed for high repetition rate operation and most of them use jet-like nozzles that dispense a liquid target [29]. Among them, a patented source design (U.S. patent 6,862,339) [128], shown in Figure 3.9, by Dr. Richardson's group at the University of Central Florida is a low-debris, high repetition rate compatible candidate. Debris is mitigated with the use of mass-limited targets, which contain just enough Sn ions to efficiently extract all the laser energy.

Droplet targets are formed through capillary dispenser with a piezo-electric module

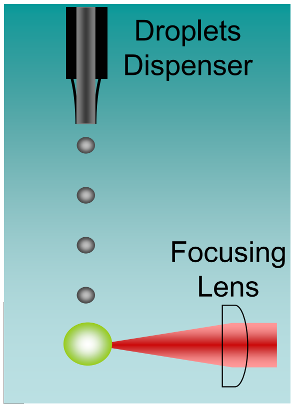

Figure 3.9: Schematic of UCF Sn-doped droplet targets [1], compatible with tens to hundreds of KHz repetition rates and effectively debris-free.

for repetition rate and synchronization control, which can be adjusted $in-situ$ during experiments. The spherical droplets are $\approx 35\mu m$ in diameter forming $\approx$ 10 mm from the exit of the nozzle with speeds of $2 \times 10^4 cm/s$ and stabilities of 3 μm at a repetition rates from 20-200 kHz. The concentration of the Sn-solution for this set of experiments is set at $\approx 30\%$ in mass, which amounts to $\approx 10^{13}$ Sn ions per droplet. Composition and target size can also be tailored accordingly to the laser energy per pulse, which as a result, minimizes debris that is mostly in the form of unionized Sn particles. The LPP source-size of droplet targets is also within the entendue limits of 1-3.3 mm^2 sr required for high brightness as stated in Table 1.2.

3.6 Experemental Setup - Sn-doped Droplet Target

Efficiency optimization of the droplet target and a high-peak-power fiber laser using a 80-μm-core fiber is studied in the experimental setup shown in Figure 3.10.

A telescope pair collimated the output of fiber laser beam to a $1/e^2$ diameter of 2 mm to 3 mm, in order to maximize transmission through the isolator, and to minimize thermal lensing inside the high-power polarization-insensitive isolator. The

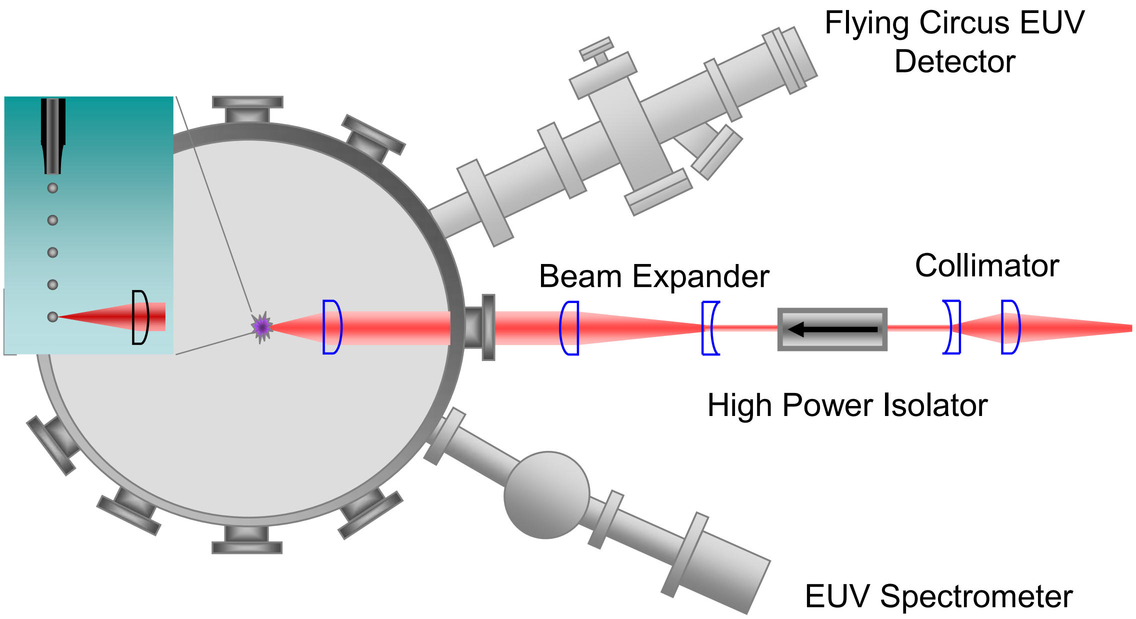

Figure 3.10: UCF experimental setup showing Sn-doped droplet source, EUV spectrometer and Flying Circus EUV spectrometer. Two pairs of telescope controlled the collimation and magnification of the laser output beam through the isolator and focusing lens. High power polarization insensitive polarizer impeded the feedback from plasma source.

isolator prevented feedback from the laser-produce-plasma. The feedback from the plasma was observed by using a pellicle sampler placed between the two stages of power amplifiers. A Si-photodiode monitored the reflection from the pellicle and showed that a spurious signal follows the signal reflected from the output beam with a temporal delay of $\approx 20ns$: the round trip time from the output end to the target ($\approx 3m$ apart). This additional feedback only presented when the laser pulse hit the droplet target (which can be controlled by synchronizing the laser to the target or blocking the laser beam between the target). An optical isolator at the output end of the fiber laser provided additional protection.

Another telescope at the output of the isolator expanded the beam before the focusing lens, a 60mm gradient lens located in the vacuum chamber with a diameter of 45 cm with 12 vacuum ports at 30° separation. A vacuum level below 10^{-3} Torr was maintained by a turbo pump backed up by a roughing pump for a low absorption of atmospheric air on EUV.

Meanwhile, two sets of telescopes were used to adjust the beam size on the focusing lens from 9 mm to 18 mm, allowing $in-situ$ control of the focal spot size on the target. With a 10× microscopic objective lens and an Ophir Beamstar CCD camera, the smallest spot size on the target is measured $\approx 18\mu m$ $1/e^2$ diameter. The image of the focal spot is shown in Figure 3.11.

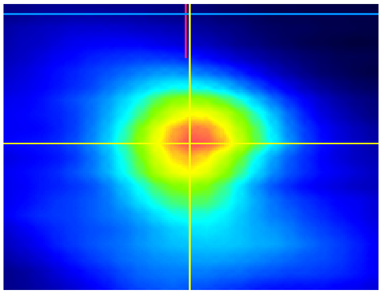

Figure 3.11: Smallest focal spot size image of 18-μm $1/e^2$ diameter measured with a 10× microscopic objective lens and an Ophir Beamstar CCD camera

A liquid-nitrogen-cooled collector cup, specially designed for this type of target, was placed underneath the target dispenser to help maintain the vacuum level by freezing the Sn-doped solution to avoid increase in particle inside chamber from evaporation. Temporal synchronization between the droplet target and the fiber-laser pulse is controlled with an external delay generator with an RMS timing jitter of less than 60 ps (Stanford delay generator). Emission from the fiber-laser-produced plasma was analyzed by two EUV diagnostic tools, an EUV flat-field spectrometer and Flying Circus EUV detector, placed 30° on the either side of the laser beam axis.

3.6.1 Laser Parameters Used in the Experiment

In the first round of experiments, an optimization study was conducted at a lower repetition rate of 1.72 kHz, providing an average output power of more than 10

W from the laser, with the droplet operating at 31 kHz (one irradiation every 18 targets). Further scaling of the average power can be achieved by increasing the repetition rate of the laser and the pump power of the last stage amplifier with preservation the output pulse parameters.

Laser parameters used are: For higher energy, 6 mJ and 6.2-ns duration pulses generated by an arbitrary waveform generator (AWG) were used where the pulse temporal profile is shown in Figure 2.20 (a). For higher peak power, shorter pulses with 1.7 ns and 2.9 mJ were used, providing a higher peak power up to 1.7 MW, yielding available intensity of $6.7 \times 10^{11} W/cm^2$ on the target. This intensity is six times higher than that which yielded the optimum conversion efficiency (Table 1.4).

Facilitated with the pulse-shaping capability of AWG, we also evaluated the effects of the prepulses on conversion efficiency. By changing the program for the arbitrary waveform generator seeder, a prepulse contrast ranging from 1:1 to 1:30 and the delay ranging from 19 ns to 100 ns were scanned to optimize EUV generation.

3.6.2 EUV Diagnostics

Two diagnostics tools were used to monitor the EUV emission from fiber-laser-produced plasma: an EUV spectrometer and a Flying Circus II EUV detector.

Figure 3.12 depicted the setup of a flat-field grazing-incidence spectrometer. An 80-μm entrance slit, 395 mm away from the FLPP source, collimated the radiation and governed the working spectral resolution. The grating is a 1200 lines/mm gold coated, variable-line-spaced (from 690 nm to 990 nm) diffraction grating with a radius of curvature of 5.649 m in the grating chamber with its center 237 mm away from the entrance slit. Aligned with an 87° grazing incident angle, the image-plane resided 235 mm away from center of grating. The geometry of the setup allowed recording of a dispersed spectrum from 11 nm to 19 nm and a sharp resolution of 0.01 nm with a 16-bit X-ray CCD camera (PI-SX, Roper Scientific) cooled by a TEC to a temperature -40°C for low thermal quantum noise, where images are recorded and processed by a personal computer.

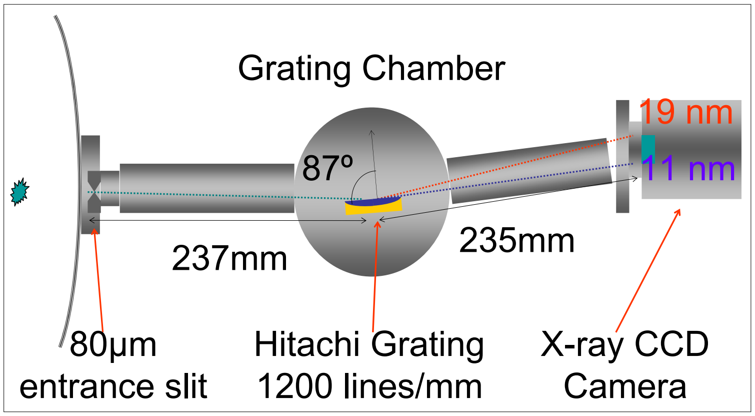

Figure 3.12: Schematics of flat-field grating spectrometer, showing an 80-μm entrance slit, acting as the line source with the illumination from the LPP. A grating in the chamber dispersed the EUV emission on to the X-ray CCD camera, recording high resolution images from 11 to 19 nm.

Broadband radiation is emitted by the fiber-laser-produced-plasma, yet only the radiation in the 2% bandwidth centered at 13.5 nm of the Mo-Si reflection band can be delivered to an intermediate focus by collector optics. The second diagnostic tool, named Flying Circus II EUV energy meter and developed by FOM-Institute of Plasma Physics Rijnhuizen was delineated in Figure 3.13. It measured the emission band of interest for EUV lithography and provided the conversion efficiency.

It consisted of a 1-inch spherical Mo-Si mirror with 69% peak reflectivity for a fresh mirror. The mirror acted as the limiting aperture for the apparatus. Since Mo-Si multilayer mirrors were also highly reflective in the VUV/VIS/IR range [3], a 0.5-μm-thick Zr filter with ≈ 18% transmission at 13.5 nm blocks radiation outside the EUV region. Reverse-biased at 24V to ensure linearity, an IRD AXUX-100 photodiode with a spectral responsivity of 0.24 A/W at 13.5 nm monitored in-band

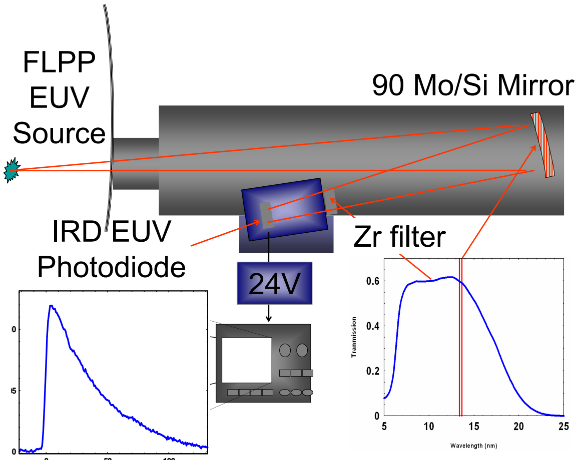

Figure 3.13: Flying Circus II EUV energy meter for CE measurement including Mo/Si mirror (acting as the limiting aperture of the apparatus) and Zr filter for wavelength selection with the corresponding spectral properties plotted in the inset. Photodiode was reverse-biased at 24 V ensure linearity.

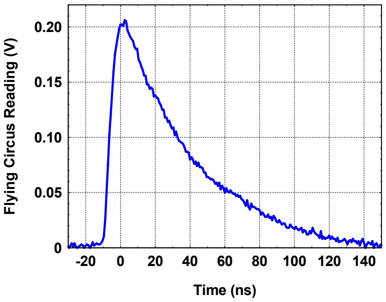

Figure 3.14: Reading of EUV diode signal from Flying Circus II (FCII) , measuring an amplitude $\approx$ 200 mV. FCII also has a very high sensitivity and fast response in the order of few nanoseconds

EUV energy. The signal from the EUV photodiode was recorded by an oscilloscope. An example of the readings was shown in Figure 3.14, which also showed a rapid response time of few ns for this photodiode.

3.6.3 Metrology of Conversion Efficiency Calculation

Instead of having a known EUV source for EUV energy meter calibration, a more sophisticated method utilizing both the Flying Circus II EUV energy meter and EUV spectrometer was used to calculate the in-band EUV energy, given by

$$E_{BW} = \frac{A_{scope}}{R_{scope}\eta_{diode}} \left(\frac{\int\limits_{BW} I_s(\lambda)d\lambda}{\int\limits_{all} I_s(\lambda)T_g(\lambda)R_{mir}(\lambda)T_f(\lambda)d\lambda} \right) \frac{2\pi}{\Omega} \tag{3.1}$$

The in-band EUV energy was calculated with Equation 3.1 by first obtaining the energy using the integrated diode signal(A_{scope}), oscilloscope resistance(R_{scope}) and diode reponsivity (η_{diode}). Since the multilayer mirror in the FCII had a broader bandwidth than 2% and also the Zr-filter transmission had a spectral dependence, it is necessary to spectrally calibrate the measured energy to include the energy only in the 2% BW by taking into account the gas transmission in vacuum chamber($T_g(\lambda)$), mirror reflectivity($R_{mir}(\lambda)$), the Zr filter transmission $T_f(\lambda)$, and the measured spectrum $I_s(\lambda)$. Isotropic radiation was assumed over the 2π solid angle and the conversion efficiency was then scaled with the solid angle of the limiting aperture Ω, which is the Mo-Si mirror in this case. *BW* here referred to the 2% bandwidth from 13.365 nm to 13.635 nm.

3.7 Conversion efficiency optimization study

Conversion efficiency studies on both water droplet target and Sn-doped water droplet target with various irradiation conditions (pulse duration, spot size, laser energy, intensity) was rigorously investigated in this experiment to provide a thorough and insightful understanding on the feasibility of high-peak-power fiber laser as an efficient EUV driver.

3.7.1 Water droplet target

Water droplets were considered as an EUV source since they are debris-free, low cost and high repetition rate compatible[1]. Earlier experiments studied the water droplets used as target for EUV source, as well as the pulse duration dependence.

During the experiment, water droplets were used as the targets for the spectrometer and EUV energy meter alignment. Also, distinct wavelength emissions from low Z materials such as oxygen were used for spectral calibration. Figure 3.15 showed spectra from water-droplet targets at various laser intensity levels. In this figure, the differences in the plasma temperature is realized from the change in the contrast in the spectral features. The first and more prominent indication of higher plasma temperature is the spectral photon count. In Figure 3.15, higher spectral count is recorded when a higher intensity is focused on the target, indicating that more EUV photons are emitted from the laser-produced plasma.

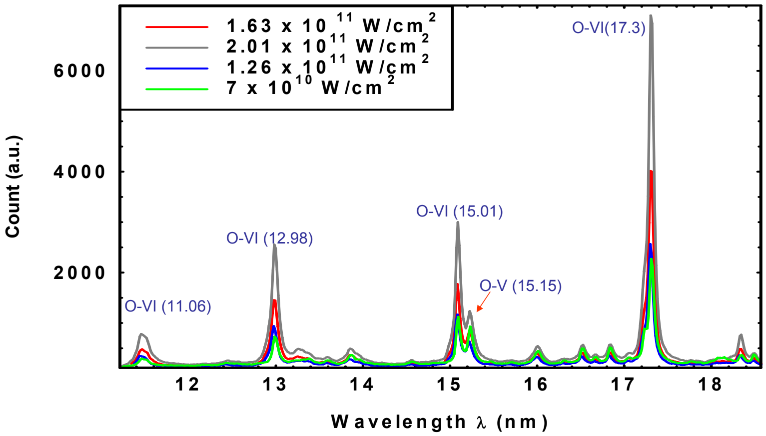

Figure 3.15: Water spectrum at four intensity levels showing emissions from different oxygen species. Change in the plasma temperature can be indicated from the change in the contrast predominately the two peaks around 15-nm. Note the emission from O-VI dominates with increase of intensity, which implies an increase in plasma temperature. Also note that each spectra is taken with the same exposure time, therefore, the photon counts directly reflect the emission strength.

Another significant change in the spectral features for higher plasma temperatures can be realized from the two spectral peaks located around 15nm, which are generated from different ionization states. The emission lines from O^{5+} (the higher ionization state) is peaked at 15.01 nm and the emission line from O^{4+} is at 15.15 nm.

An increase in the population of higher ionization states generally corresponds to an increase in the plasma temperature. In Figure 3.15, the strengths of the two emission peaks were close at an intensity of $7 \times 10^{10} W/cm^2$, while the emission peak from O^{5+} to the emission peak from O^{4+} increased to 2:1 when the intensity was increased to $1.63 \times 10^{11} W/cm^2$.

One important piece of information gathered from water-droplet spectrum is the actual plasma temperature. The actual plasma temperature from the experiment can be estimated by the comparing experimental spectra and the synthesized spectra at which the plasma temperature is known.

3.7.2 Sn-doped droplet target

The Sn-doped target was implemented, followed by the characterization of a water target. Two different pulse durations were selected to test the effect on EUV conversion efficiency. Shown in Figure 3.16, the best spectra for two different pulse durations were obtained at highest recorded conversion efficiencies. For 1.7-ns pulses, the highest attainable conversion efficiency was 0.33% with the intensity of $1.65 \times 10^{11} W/cm^2$. For 6-ns pulses, the conversion efficiency of 0.9% was recorded at intensity of $1.19 \times 10^{11} W/cm^2$.

Photo counts of the spectra shown in Figure 3.16 also manifested the difference in the plasma temperature showing that Sn UTA from the emission by 6-ns pulses has narrower width and higher peak than those from 1.7-ns pulses. It is noteworthy that even higher intensity was achieved at shorter pulse durations, the conversion efficiency is three times lower than CE from longer pulses, exhibiting that CE has a very strong dependence on temporal duration even within few nanosecond range. Other experimental condition for efficiency dependence of two pulse durations remained the same including the type of lens used (60-mm Gradium lens), focal spot size (30 μm $1/e^2$) and the size of the target to have a plausible pulse-duration dependence study.

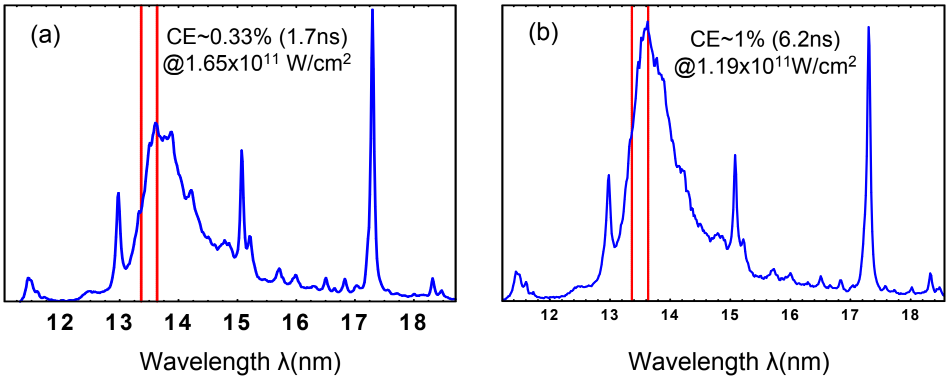

Figure 3.16: Pulse duration conversion efficiency scaling showing the spectra for pulse durations of 1.7 ns and 6 ns. CE of $\approx$ 1% from 6-ns pulses is obtained at intensity level of $1.19 \times 10^{11} W/cm^2$ and CE of $\approx$ 0.3% is obtained for 1.7-ns pulses at the intensity level of $1.65 \times 10^{11} W/cm^2$. Note that the difference in the spectra from 1.7-ns shows lower and broader Sn UTA indicating a lower plasma temperature even with higher intensity on target.

Figure 3.17 showed CE dependence on the lens position and laser intensity for 6ns pulses(laser intensity was adjusted by changing the focal spot size while keeping the same energy of the laser) and it showed that the highest efficiency was obtained at the focus where the spot was the smallest, corresponding to highest intensity at $1.19 \times 10^{11} W/cm^2$.

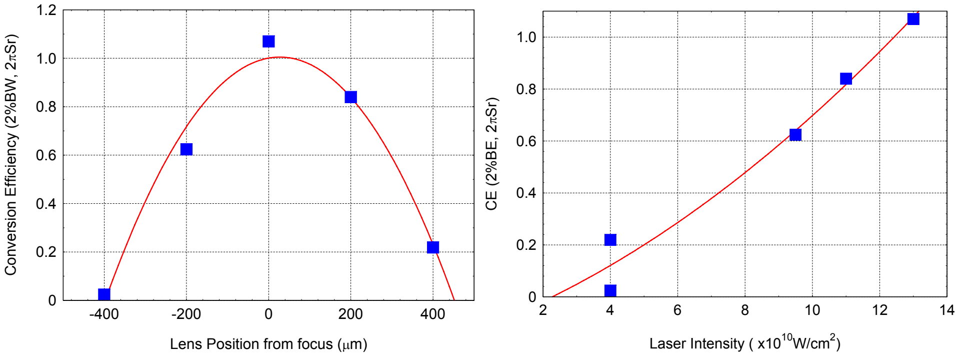

Figure 3.17: (*Left*) CE dependence on the lens focal position and (*Right*) The dependence of the laser intensity for 6-mJ and 6-ns pulses. The laser intensity is altered by transversing the position of the focusing lens.

Increase in pulse duration effectively optimized the CE by three times, yet, 1% CE did not provide enough yield for the EUV lithography application as it doubled the laser power requirement (Section 1.5) and more importantly, it was noticed that this conversion efficiency was only half of what was achieved by a solid-state laser at the same intensity. One possible explanation for not being able to reach the same CE at the optimal intensity was attributed to the temporal shape of the laser pulse. A Q-switched ns-solid-state laser in general generates a output pulse with a Gaussian temporal profile. The extracted output energy of a solid-state laser is much lower than its saturation energy, even at hundred-mJ energy levels. Temporal reshaping due to gain saturation will not be in effect under this condition in the YAG laser.

In the fiber-laser system with semiconductor diode seed, the amplified pulse had a much steeper rising edge compared to that of a Nd:YAD laser (Figure 2.20(a)). The rising edge of the temporal profile measurement was actually limited by the rise time of the detector (Si photodiode with rise time of 450ps). The difference in the leading edge of the pulse is speculated to be the reason for the lower conversion efficiency given the target plasma temperature is still low while most of the laser photons were incident on the target. Therefore, the absorption of the laser energy is not optimal. Later experiments that introduces prepulses to preheat will verify this assumption.

3.7.3 CE optimization with prepulses

Many previous EUV efficiency studies indicated that the introduction of a prepulse under the right conditions enhances the conversion efficiency [32, 105, 106]. As described earlier in Section 2.6, seeding using an AWG can conveniently generate pre-pulses with a programmable contrast and delay. In our prepulse optimization study, four different delays were tested: 27ns, 45ns, 75ns and 100ns. Contrast can also be arbitrary adjusted during the experiment while the laser is still in operation from ratio of 1:1 to 1:30. It was found that the best yield can be found at delay of

45ns and the spectrum was shown in Figure 3.18 with comparison to the condition without the prepulse, note that the temporal shape of the main pulses resembled the one without the prepulse.

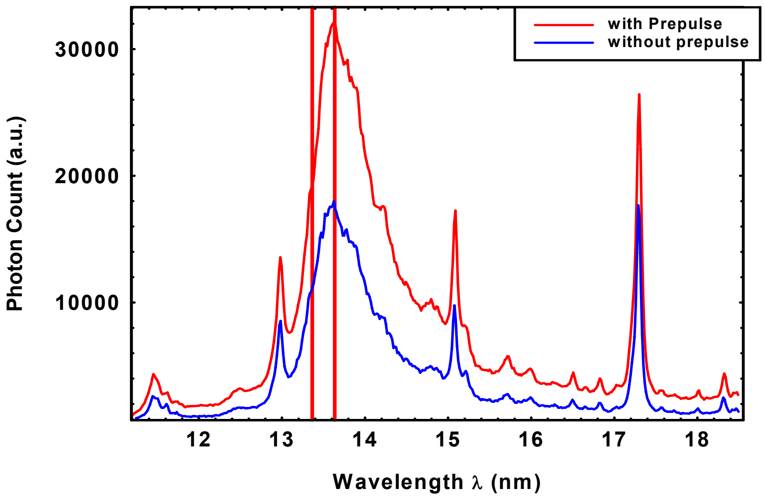

Figure 3.18: Spectra with and without prepulses. In both testing conditions, the shape and energy of the main pulse remain identical.

The photon counts in the figure of the Sn UTA showed two-fold improvement when prepulses were used to preheat the target and the contrast between the peak of the UTA to the 17 nm oxygen line is also enhanced (larger increase in Sn UTA) with pre-pulse, another indication more optimum irradiation condition attainable with prepulses preheating.

Figure 3.19 showed the optimal spectrum from the fiber-laser-produced-plasma with Sn-doped water-droplet targets as well as the image from the X-ray CCD camera. The spectrum had four sharp emissions from O^{5+} at 11.58 nm ($2s-4p$), 12.97 nm ($2p-4d$), 15.01 nm ($2s-3p$) and 17.3 nm ($2p-3d$), used for spectrum calibration [1]. Centered around 13.5 nm, the Sn unresolved transition array (UTA) has a spectral width of 1 nm FWHM.

CE dependence versus intensity was realized by adjusting the pump power of last stage amplifier to and by varying the focal spot size by transversing the focal

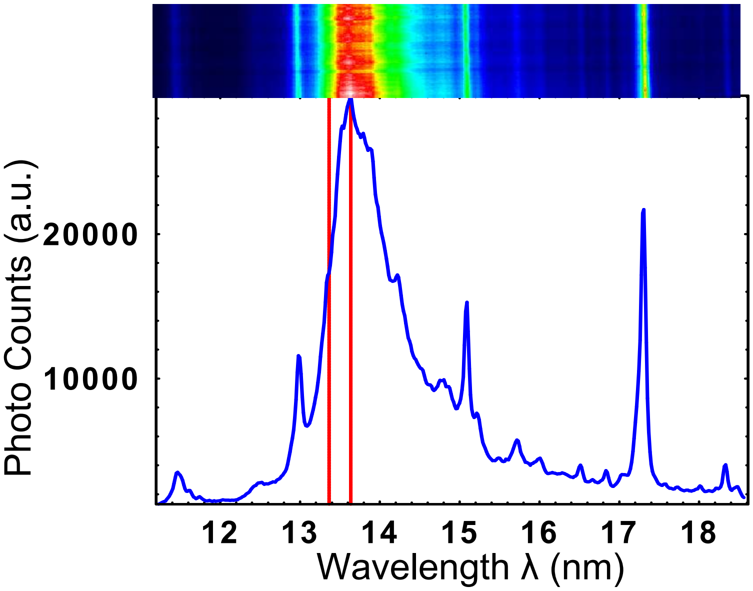

Figure 3.19: Best spectrum with prepulse preheating showing emission from Sn-doped water droplet target. It shows the image of the X-ray CCD camera on the top. Spectrum features the O^{5+} emission peaks at 11.58, 12.97, 15.01 and 17.3 nm, providing the reference points for spectral calibration.

lens position. The focal lens, mounted on a piezo-electric controlled translation stage, allowed changing the relative position outside the vacuum chamber in three directions: the z-direction to change the target focal spot size and the x- and y-directions to optimize the overlapping between focal spot position and the spherical target.

Figure 3.20 plotted the spectral dependence at different intensity levels, and showed that photon counts increased significantly when the laser intensity was increased from $2 \times 10^{10} W/cm^2$ to $9 \times 10^{10} W/cm^2$. Also, the spectral peak of the Sn UTA shifted from a longer wavelength to a shorter wavelength. The photon counts start dropping once the intensity is higher than $8 \times 10^{10} W/cm^2$, indicating that the optimum intensity for highest conversion efficiency is at this level. All the spectra shown were averaged over five spectral images, each with one second of exposure time, corresponding to an average of more than 8500 laser shots for each spectrum.

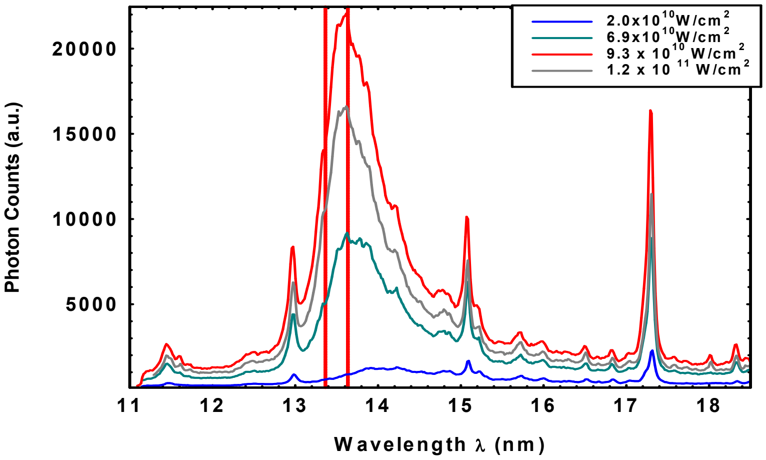

Figure 3.20: Study of spectral dependence on intensity showing a compelling increase in photon counts as the intensity increased from low to high $10^{10} W/cm^2$. Photo counts starts to decrease as the intensity increased further, indicating the optimum intensity level. The testing here utilizes prepulses of 45-ns delay and intensity includes the energy in the prepulse.

To ensure the same calibration for the Mo-Si multilayer mirror in which the reflectivity degrades by plasma debris coating, the conversion efficiency was estimated by calibrating the spectrum with the Flying Circus energy meter [2]. EUV energies measured using Flying Circus II (FC II) were taken along with several spectra for reference. EUV energy at other irradiation conditions was then calculated using measured spectrum and comparing photon counts, and spectral shape in the Mo/Si reflection band to those of the reference spectra. After the completion of all experiments, the Mo-Si multilayer mirrors in the FC II and Zr filter was calibrated at the National Institute of Standards and Technology to ensure correct conversion efficiency measurement.

Figure 3.21 plotted CE as a function of lens position and laser intensity on target and the highest conversion efficiency achieved was 2.07% at the intensity of $8.4 \times 10^{10} W/cm^2$. Beyond this intensity level, conversion efficiency declined. The drop in the conversion efficiency indicates that the optimal conditions for EUV generation were reached within the fiber-laser parameter space.

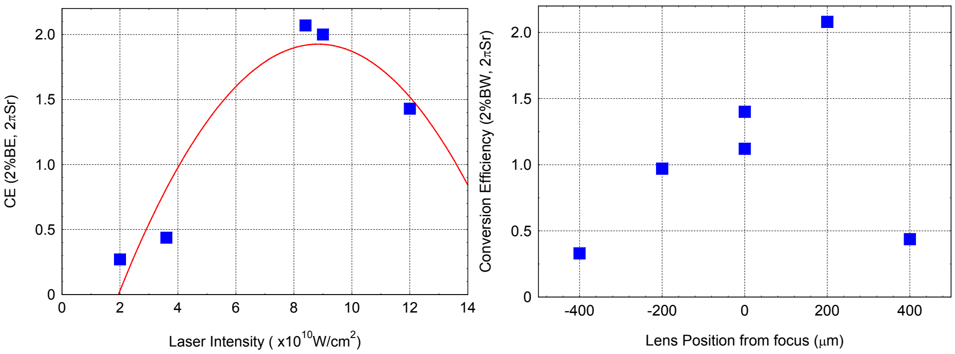

Figure 3.21: CE dependence on laser intensity (on the left) and lens position (on the right). The plots shown here used prepulses with delay of 45-ns and contrast of 1:10. Highest CE is reached at the intensity level of $8.4 \times 10^{10} W/cm^2$ and CE is lower with intensities higher than optimum. Interesting to note from the lens position dependence that CE is higher when the beam is diverging (+ 200 μm), which was first observed in [2]

Even with the use of lower-density Sn doped water droplet targets, there still existed a problem with Sn particle deposition on the focusing lens. After the experiment, energy transmission of the focusing lens is measured accounting for the conversion efficiency calculation. Averaged change in the transmission is ≈ 60% for ablation time ≈ 30 minutes. One possible explanation is that the overlapping between the focal spot and the target were not optimized at the beginning of the experiment. When the target was ablated off-centered, most target materials were sputtered rather than ionized, hence, creating a tremendous amount of neutral ions or high energy particles. The debris created under these unfavorable conditions will scatter in all directions and coat the focusing lens. Also, the overlap between the target and the focus had to be constantly and manually adjusted, therefore, making it difficult to ensure favorable irradiation throughout the experiment. The debris coated on the lens after the experiment, obtained by a scanning white light interferometer [3], is shown in Figure 3.22.

Another reason is that with the use of lower energies from the fiber laser, the pulses failed to ionize every Sn particles in the target completely, as a result, the "unused

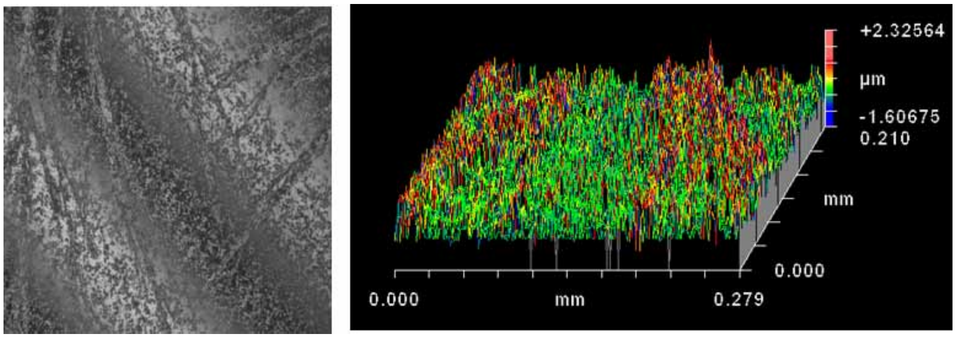

Figure 3.22: (Courtesy of Dr. Simi George) The image of scanning white light interferometer showing the debris coated on the focusing lens after ≈ 30 minutes of target irradiation [3].

targets" became source of contamination. In the experiment using a solid-state laser with 100-mJ energy per pulse and a 35-μm focal spot size [2], coating due to debris generation is minimized. This coating of debris can be cleaned immediately after the experiment with a minimal loss in the transmission (≈ 1%) after each cleaning. However, the lens AR coating will be eventually etched and introduce excess loss on the transmission, making it unfeasible for further use.

The comparison between the best spectra from a 1-Hz, 100-mJ laser with a 35-μm spot and the best spectra from the fiber laser is shown in Figure 3.23. Both spectra are normalized to the O^{5+} at 13 nm and the wavelength scale for the solid-state laser is slightly offset to better reveal the spectral difference. The targets and the experimental conditions are the same for both spectra and it is obvious that emissions of fiber laser resembled the spectral properties of that from a solid-state laser, as well as providing the equivalent efficiency of solid-state laser.

Furthermore, better debris mitigation is expected with higher pulse energies, made possible with beam combining, and larger focal spots or by reducing the size of the target for bettering matching the droplet diameter and focal spot size.

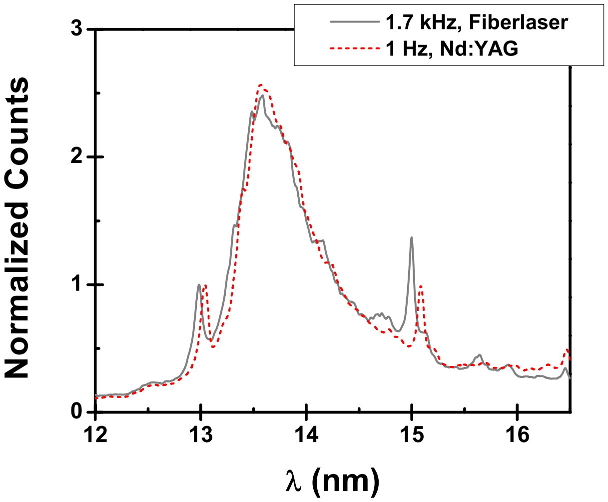

Figure 3.23: (Courtesy of Dr. Simi George) Comparison of the spectra from fiber laser and solid-state laser shows that fiber laser created the same irradiation condition for optimum efficiency extraction given very different pulse energy, pulse duration and focal spot size. [3]

3.8 Conclusion

The feasibility of EUV generation by a fiber laser were realized in two experiments. The first experiment using a solid-Sn target yielded 1% of conversion efficiency at a intensity of $1.2 \times 10^{10} W/cm^2$, the highest extractable from the 115-μm-core fiber. Experiences from this experiment further revealed the needs for a laser with higher intensities laser and a low-debris target compatible with a higher repetition rate. This demonstration, being the first EUV generation of fiber laser, extended the choice of feasible laser candidate for high efficiency high power EUV source.

Second experiment with realistic Sn-doped water-droplet targets verified fiber-laser EUV driver as an efficient choice of laser. A conversion efficiency of 2.1% is obtained while operating at 1.75 kHz with a laser power more than 10W in this optimization study. A decrease of conversion efficiency with a laser intensity higher than optimum point also indicates that fiber-lasers are capable of generating irradiation condition which are optimum for efficient 13.5-nm EUV generation. The achieved conversion efficiency was essentially same as that obtained using a Q-switched solid-state laser, despite the fact that the energy and peak power of a solid-state laser are higher than those of fiber lasers.

Successful demonstration of the same conversion efficiency with less energy per pulse opens up a pathway for fiber lasers to suitable drivers for high power EUV lithography with their programmable temporal parameters. The high beam quality of new LMA fiber systems and the ample gain bandwidth of Yb-doped fibers also indicate an unrivaled potential for power scalability to tens of kW by spectral combining and spatial overlapping.

CHAPTER IV

Spatial Dispersion Free Spectral Beam Combining Using Multilayer Thin-Film Filters

Multi-kW-class high-power lasers with near-diffraction-limited mode qualities are desirable in many applications of laser cutting, laser welding, laser fusion, and defense. The main technological limit is the thermo-optic effects that degrade the mode quality at a high pumping power. One of the most promising solutions is to combine multiple laser beams without degrading the mode quality.

Among all the laser types, semiconductor lasers and fiber lasers are the most suitable types of lasers to apply beam-combining because of the ease with which they can be built into arrays, the diffraction-limited beams they produce and their high electrical-to-optical efficiencies. Fiber lasers, in addition, bear additional advantages of a domination of waveguide properties over thermo-optic effects and high surface-to-volume ratio, alleviating the design requirements on the thermal management compared to solid-state-laser. Because ultimately limited by the optical damage, thermal dissipation, and nonlinear effects, it is necessary to combine multiple fiber laser beams into a single output beam to achieve powers exceeding 100 kW.

This chapter begins with a brief introduction on laser beam combining and reviews previous work on different beam-combining techniques. We then propose a spectrally combined fiber-laser-systems using the multilayer dielectric filters (MLD) filters as the spectrally combining elements, which are not based on spatial dispersion and, consequently, eliminate the principal limitations of the conventional spectral combining schemes based on the dispersive-grating components. We studied the performance of this novel scheme by a combination of spectrally broadened fiber lasers into a single spatially-overlapping high-quality beam with $M^2 \approx 1.86$, $> 91\%$ of combining efficiency, 52-W of average power and 4.0-mJ of pulse energies.

4.1 Introduction of Laser Beam Combining

The first and the simplest type of laser beam combining is incoherent spatial combining, without imposing any spectral or phase control. The conventional diode-laser arrays and the fiber bundles are two such examples. In spite of increasing the total power, the incoherent spatial combining does not improve the radiance and consequently, can not provide a near-diffraction-limited output.

Other types of laser beam combining were pursued greatly over the past few years [129, 130] in techniques using both spectral beam combining (SBC) [131, 132, 133, 134, 135] and coherent beam combining (CBC) [136, 137, 138, 139, 140, 141, 142]. Both types of combining schemes can improve the radiance from a single laser output, however, only CBC can improve the spectral radiance. Current state-of-the-art SBC system achieved a combined power of 522W [133, 132]. 470W using CBC [138] was also obtained recently. In both CBC and SBC, the radiance scales with the number of the channels times the combining efficiency. Previous work and the general properties of CBC and SBC will be briefly discussed in the next two sections.

4.1.1 Coherent Beam Combining (CBC)

Historically, coherent beam combining (CBC) is the type of the combining scheme that had been studied the most extensively, in the application of semiconductor, solid-state, gas and fiber lasers. However, due to its fundamental challenges on precise phase-locking, not much success was accomplished until recently. In principle, CBC implements phase-locking of the individual laser elements to a common frequency and vectorially summing the output amplitudes into a spatial array, and consequently, providing an increase in brightness compared to individual beams.

However, the major and the most demanding requirement is the phase-locking between the laser elements, only allowing an error to a small fraction of the wavelength. Additionally, since the electric field must be constructively added, the output polarization of each laser elements must be precisely controlled at every instant of time. Most of the developments in CBC, as a result, has been focused on finding the sophisticated locking techniques. Even with the best phase-locking mechanism, the combined beam still generate far-field side-lobes, contributing 30% of the total power, even under the ideal phase condition.

The phase-locking techniques developed over the years include: common resonator, evanescent-wave, self-organizing, active feedback, and nonlinear optical. Currently, the state-of-the-art coherent by the active feedback phase-locking (Figure 4.1) demonstrated a four-channel combining with a total output power of 470 W. However, only 70% of the power resided in the central fringe of the multiple-lobe far-field combined beam.

4.1.2 Spectral Beam Combining(SBC)

SBC schemes implement dispersive beam combining elements, i.e. diffraction gratings and volume Bragg gratings, to combine laser elements at distinctive central frequencies. Therefore, it trades the brightness enhancement with the loss of the spectral purity. However, in most high power applications, spectral properties are

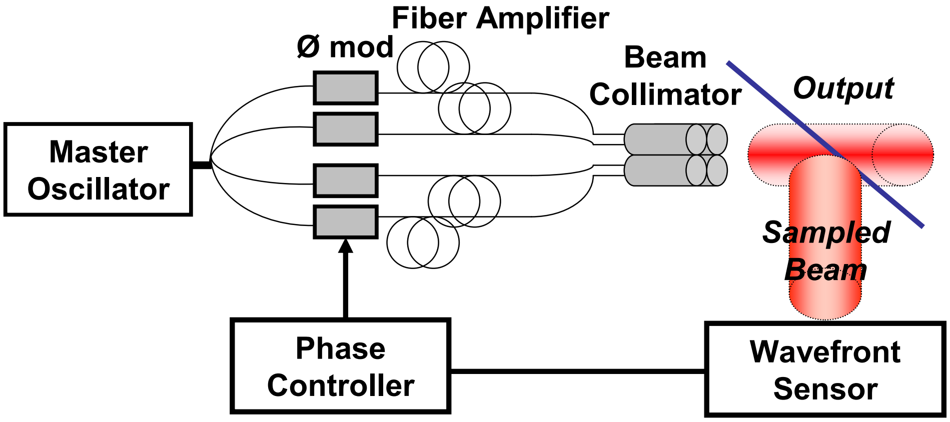

Figure 4.1: Coherent combining with active feedback by detecting the output phase to control the phase of the beams to be combined.

not the major concerns.

SBC is favored over CBC for the reasons of its anticipated robustness and relative simplicity for implementation. Indeed, conceptually it merely requires multiple independent lasers of distinct wavelengths whose output is spectrally combined by the combining element(s). High robustness of the overall system should result from the fact that, unlike CBC, no active optical path-length and phase control is required. In general, the advantages of SBC over CBC include,

i. SBC does not use spatial addition of multiple elements, and Gaussian beams at both near field and far field can both be realized without losing a significant part of the power into the side lobes.

ii. Laser sub-elements are not coupled since SBC does not require phase synchronization, yielding a greater potential in scalability.

iii. SBC requires wavelength-control instead of phase-locking, a great alleviation from engineering difficulties and an ideal situation to exploit ≈ 60 nm of the Yb^{3+} gain bandwidth.

The potential in scalability was appreciated in the numerical prediction by Brochove [143], stating that more than 160 channels can be packed into ≈ 60 nm wide

Yb^{3+} gain bandwidth with an $M^2 < 1.5$ combined output, using a geometric channel spacing < 1 mm, a transform optical length < 50 cm, 1-kW fiber lasers operating < 3 GHz, and a grating groove density of 1740 lines/mm.

Many successful work using the dispersive spectral elements have validated both the scalability and the robustness of SBC. Augst reported one of the earliest work in spectral-combining Yb-doped fibers with a combined power of 6W (five-channels-combining) and excellent mode-quality of $M^2 \approx 1.14$.

Loftus combined three channels of Yb-MOPA lasers (Figure 4.2), with ≈ 522 W of combined power, $\approx 93\%$ of combing efficiency and a mode quality of ≈ 1.2 [132]. Using volume Bragg gratings, two channels of high average power fiber lasers with 180 W were combined with 92% combining efficiency by Ciapurin [135]. However, optical path difference was a problem, creating an issue when focusing the combined beam to measure the mode quality.

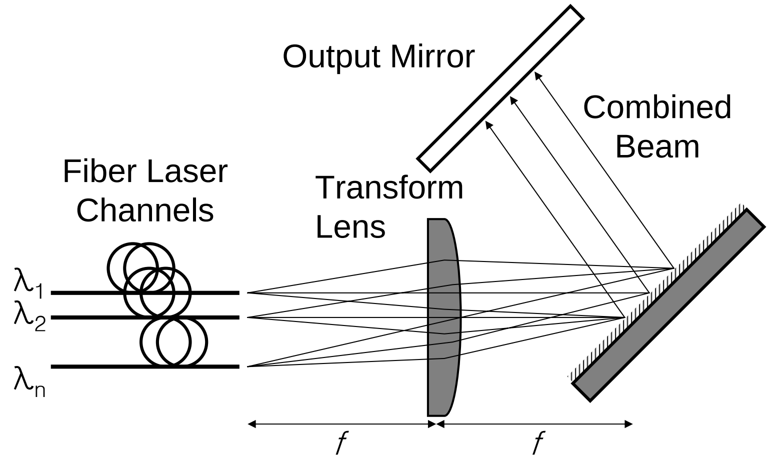

Figure 4.2: Spectral combining setup using a diffraction grating to combine beams at different wavelengths, which are incident at a slightly different angle.

4.1.3 Limitation on Spectral Beam Combining

Careful investigation, yet, reveals significant technological limitation in spectral combining approach constituted by the spectral combining element itself. Current spectral combining methods are based on spatial spectral dispersion such as diffraction gratings [130, 131, 132, 133, 134] or volume Bragg gratings [135] to superimpose beams of different optical wavelengths. Limitation on the linewidth and the beam size to retain the mode quality for spatial dispersive combining elements bears potential problem for combining fiber laser with MW peak powers. For spectral combining using diffraction grating, spatial dispersion will result in additional angular divergence proportional to $g\Delta\lambda$ where g is the grating grooving density and $\Delta\lambda$ is the laser linewidth [133]. The spatial dispersion effect is also dependent on the spot size on grating.

For a desired combined beam quality (M^2), there exist a limitation on both the spot size on the grating and the linewidth beam governed by,

$$\Delta\lambda = \frac{2\sqrt{(M^2)^2 - 1} \times c \times \cos(\alpha_0)}{g \times \lambda \times \pi} \times \frac{1}{\omega_0} \tag{4.1}$$

where $\Delta\lambda$ is the linewidth in Hz, M^2 is the mode quality, c is the speed of light, α_0 is the incident angle of the grating (which usually equals to Littrow), g is the groove-density in lines/mm of grating ω_0 is the beam width in mm. Figure 4.3 plots the requirement on the linewidth and the beam-width requirement for a near-diffraction limited output beam ($M^2 = 1.2$ to 1.5) from the diffraction grating combiner with an 1064 nm wavelength, 1740 lines/mm grating and Littrow ≈ 66°, the same parameters as used in [133, 130].

Note that Equation 4.1 applies to combining diffraction limited beam, for beams with $M^2 > 1$, the combined mode quality becomes worse. Analysis shows for linewidth in the order of tens of GHz, beam radius <1 mm is required, which will lead to very high power density on the grating as shown in Figure 4.4 with targeted

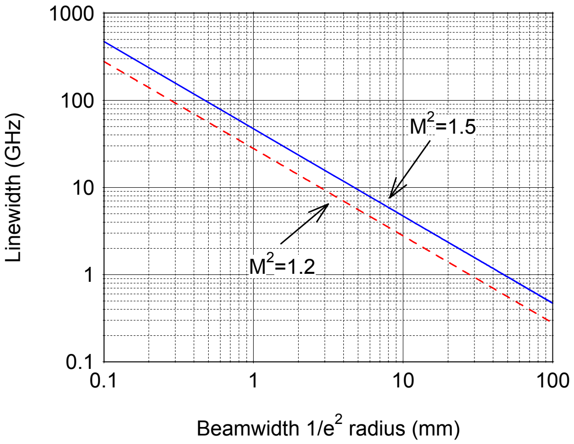

Figure 4.3: Design tradeoff for the laser spot size on a diffraction grating and linewidth of the laser to maintain mode quality between M^2=1.2 to 1.5. The example shown here is plotted using 1740-lines/mm grating at a Littrow (66°) incident angle.

combining power 5 kW, 25 kW and 100 kW.

$$I_{peak} = 2P/(\frac{\pi\omega_0^2}{\cos(\alpha_0)}) \tag{4.2}$$

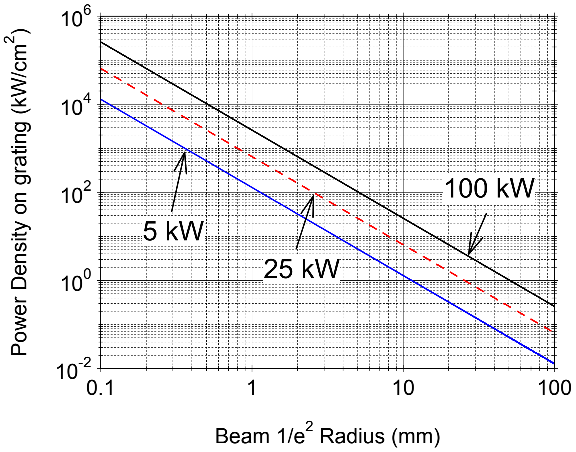

Figure 4.4: Average power densities on the combining grating (SBC) for combined powers of 5 kW, 25 kW and 100 kW.

One way to mitigate the power density on the grating is to use a larger spot size on the grating with narrower linewidth to maintain the combined beam quality. Yet, smallest linewidth from an multi-stage MW-peak-power Yb-doped-fiber-amplifiers is limited by spectral broadening of nonlinear effect, i.e. self-phase-modulation (SPM).

Assuming an unchirped Gaussian input pulse, the change in the pulse spectrum due to SPM is given by $\delta\omega_{\max} = 0.86\Delta\omega\varphi_{\max}$ where $\Delta\omega$ is the initial spectral width and unchirped Gaussian pulse $\Delta\omega = T_0^{-1}$ where T_0 is the pulse duration. $\varphi_{\max}$ is the maximum phase shift defined by $\varphi_{\max} = \gamma P_0 z_{eff}$ where γ is related to nonlinear index coefficient n_2 by $\gamma = (n_2\omega_0)/(cA_{eff})$ $A_{eff}$is the effective core area and c is the speed of light and ω_0 is the angular frequency. z_{eff} is the effective length of the amplifier and related gain of the fiber g and length of the fiber L by $z_{eff} = [1 - \exp(gL)]/g$

For n cascaded stages of amplifiers where each stage has different gain, core size and length, the increase in spectral width $\delta\omega_{\max}$ for the overall system can be given by,

$$\delta\omega_{\max} = \sum_{i=1}^{n} 0.86 T_0^{-1} \frac{2\pi n_2}{\lambda A_{eff(i)}} P_i \frac{1 - \exp(g_i L_i)}{g_i} \tag{4.3}$$

where n is the number of amplifier stages, T_0 is the initial pulse duration, n_2 is the nonlinear refractive index ($3.2 \times 10^{-20} m^2/W$ for fused silica), λ is the wavelength of the signal,$A_{eff(i)}, P_i, g_i$ and L_i the effective core area, input peak power, gain and length of amplifier of ith stage respectively.

With parameters provided in [82] with assumption of equal gain per stage and 3dB interstage loss due to optical isolator, filter and coupling, Equation 4.3 gives the increase in spectral width of $\approx$ 18 GHz, similar to empirical observation reported in [82]. Hence, the spectral broadening of MW peak power pulses in a cascaded multi-stage amplifier will induce tens of GHz spectral broadening even seeding with unchirped transform-limited Gaussian pulses. This bandwidth leads to requirement of $< 1mm$ beam width on the grating to maintain mode quality with $M^2 < 1.2$. With this beam diameter, only up to $\approx$ 25 mJ of nanosecond pulses can be combined in by gold coated grating with reported damage threshold at ≈ 0.8 J/cm^2 for 1-ns pulses [144].

Although all dielectric diffraction has a higher damage threshold up to 4.4 J/cm^2

for 5 ns pulses [145] (which gives maximum combined energy ≈ 138 mJ), the spectral bandwidth of such gratings are typically in the range of 15 nm to 20 nm [146], which is too narrow to exploit the large gain bandwidth (≈ 60 nm) of Yb-dope fiber amplifier [133]. Consequently, an alternative spectral combining scheme free from spatial spectral dispersion will be desirable for combining fiber laser with MW peak power output.

4.2 Spatial Dispersion Free Spectral Combining using Multilayer Film Filters

4.2.1 Multilayer Thin Film Coating for High Power Application

Development of dielectric thin-film technology was driven in late 1990s by the demand of wavelength-division-multiplexed optical communication-system during telecom boom. Current technologies for thin-film coating including electron-beam deposition (e-beam), ion-assisted e-beam (IAD) and ion-beam sputtering (IBS) and all the processes are conducted in a vacuum chamber.

In e-beam technology, materials heated by an e-beam, generated by hot filaments, evaporate and condense on the substrate in the direct line of sight. IAD deposition is similar to the e-beam deposition with an additional ion gun bombarding on the substrate which help the vapor from the e-beam deposition to form a denser film.

In IBS (Figure 4.5), a metal or metal oxide target is irradiated by a high-energy ion-beam from an ion source and a given molecule with ≈10 eV of energy is sputtered from the surface of the target and deposited on the substrate. Due to the high thermal energy, the molecules form a covalent bond upon deposition and result in a uniform, dense and non-porous coating with superior adhesion.

The key parameters of the three deposition techniques are listed in Table 4.1. In the IBS deposition, although the atom-by-atom removal is slower and the process is

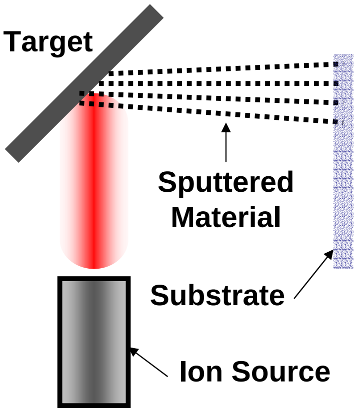

Figure 4.5: Ion beam sputtering (IBS) offering a high degree of control on depositing the materials on the substrate.

	E-beam	IAS	IBS
Cost	least expensive	in between	most expensive
Density	low	medium	high
Damage fluence (for ns-pulses)	20-40 J/cm^2	slight lower than E-beam	$40 J/cm^2$
Surface roughness	1 A	4 A rms	< 1A for 50 layers
Advantages	cost and versatility, easily scalable processes	higher packing density, can be used on plastic	near theoretical reflectance
Disadvantages	porous film, low packing density	contamination not easily controlled	slower and expensive, can not be used for UV coating

Table 4.1: Properties of the three commonly used thin-film coating methods

more expensive than e-beam or IAS, its higher damage thresholds, near theoretical limits reflectance, low absorption, superior optical quality, excellent stress and environmental sensitivity properties make IBS the ultimate choice for the production of high power and high quality optical coatings.

Multilayer dielectric (MLD) filters had been widely used to multiplex high-power semiconductor laser-diodes with different wavelengths to pump high-power fiber lasers. However, due to its limited wavelength selectivity (sharpness), it has not received much attention as a solution to high spectral-density beam combining. The recent developments on the ion-beam-sputtering MLD filters have greatly improved their efficiency (reflectivity/transmission), wavelength selectivity (sharpness) and energy/power damage threshold and make them a viable combining elements for high-power efficient beam combining [147]. To study the feasibility of these combining elements, we use a combining scheme relying on MLD filters rather than elements using spatial-spectral dispersion.

Consequently, this approach offers the following principal advantages:

(i) It allows broad-bandwidth signals thus eliminating SBS-induced limitations on individual-laser output power. Since each individual beam does not experience any spatial dispersion in multilayer-film combining components, no beam divergence in addition to diffraction is produced for a signal of any arbitrary spectral width. This also eliminates the constrain on the beam size since beam size does not affect combined-beam quality.

(ii) In principle, the MLD deposition on a flat glass substrate are much more suitable for multi-kW power scaling compared to any grating structure. Existing ion-beam-sputtered MLD filters fabricated on high quality flat glass substrates already can withstand multi-kW powers without any observable thermal effects. Further power scaling should be relatively straightforward and can be further facilitated by the absence of principal constraints on the beam size.

(iii) These filters can be designed to be polarization insensitive for a certain incident angle up to 45°. This significantly simplifies the requirements for a fiber laser design, eliminating need for using the polarization-preserving fibers.

Based on MLD filters, a combining scheme (type I combiner), is illustrated in Figure 4.6, where the beam is multiplexed through reflection in the combining element

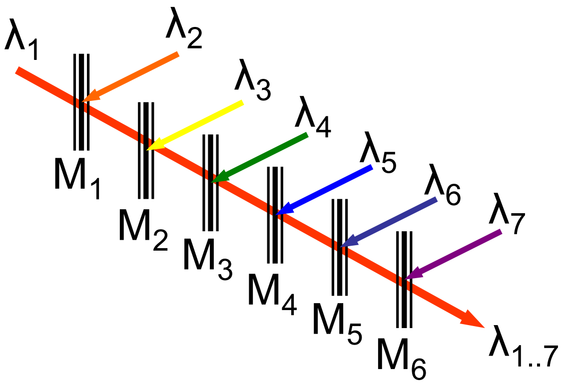

Figure 4.6: Type I combiner, in which a combined beam (located on the long-wavelength side of the LPF filter edge) is transmitted through the filter. Meanwhile, each new spectral channel (located on the short-wavelength side of the LPF filter edge) is added to the combined beam by reflection from the filter.

through cascaded filters. This scheme allows relatively simpler alignment since the spacing between the channels is only determined by filter separation.

An alternative scheme (type II combiner) where channels to be combined are transmitted by the MLD filters as sketched in Figure 4.7. For a substrate with a relatively higher absorption, type II combiner imposes less thermal load on the filter, since each combining element will only have the thermal load generated from laser power of one channel and the combined power is efficiently reflected by the MLD thin film.

In Figure 4.8 spectral transmission of each edge filter $M_1, M_2....M_6$ and laser spectra centered at 1064 nm are shown. In this example, six filters can spectrally combine up to 7 lasers, however, much larger numbers of combined fiber lasers are possible, depending on filter characteristics as discussed further in the text. Each filter in either Figure 4.6 or Figure 4.7 configuration should have a sharp edge in the spectral transmission characteristics separating the spectral ranges where the optical waves are either reflected from the multilayer thin-film coating or transmitted through the coating layers and the substrate. Although the particular example of

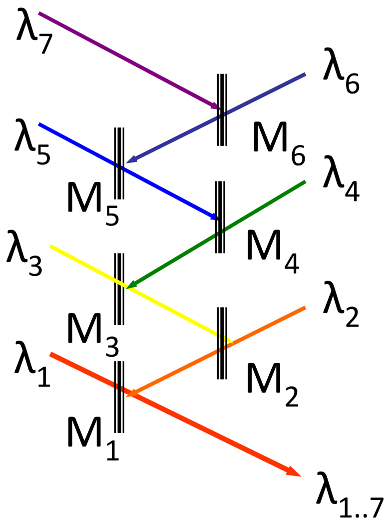

Figure 4.7: Type II combiner showing the combined beam is reflected (and is located on the short wavelength side) while each new spectral channel is added through transmission (on the long wavelength side of the corresponding filter spectral edge).

Figure 4.6 and Figure 4.7 uses long-wavelength-pass filters, short-pass filters could be used instead.

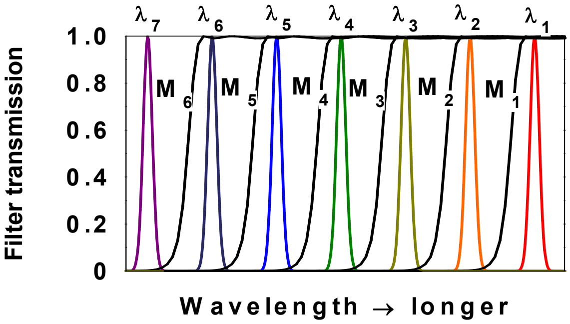

Figure 4.8: Relative wavelengths of the laser lines and multilayer cutoff edge for the combining configuration in Figure 4.6 and 4.7.

The ultimate choice of combing scheme is designated by the overall efficiency, given by

$$\eta^{I} = \frac{R(1-T^{N-1})/(1-T)+T^{N-1}}{N} \tag{4.4}$$

for type I combiner or

$$\eta^{II} = \frac{T(1-R^{N-1})/(1-R)+R^{N-1}}{N} \tag{4.5}$$

for type II combiner and where N is number of channels, T is the transmission, and R is the reflectivity. Applying Equation 4.4 and 4.5, Figure 4.9 predicts the channel-number scaling as a function of filter efficiencies (T and R) for both types of combiners. In order to combined 40 channels with 90% of total efficiency, each is required to have 99.7% of reflectivity/tranmission. If the filter has lass than 97% of reflectivity/tranmission, only 5 channels can be combined with $>$ 90% efficiency. Therefore, a slight increase in the reflectivity/tranmission will yield a much higher channel density to reach the $>$ 90% overall efficiency.

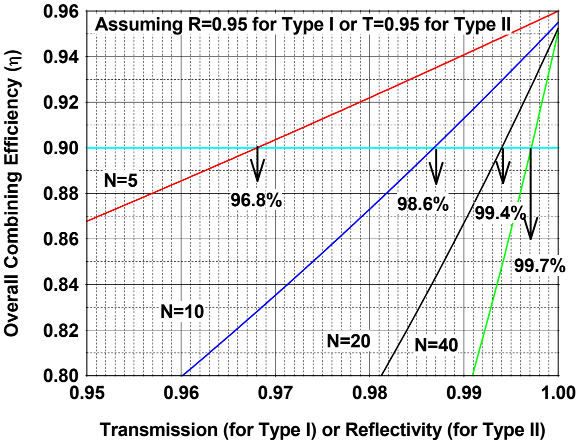

Figure 4.9: Analysis showing the requirement on the filter transmittance of type I combiner/ the filter reflectivity for type II to achieve overall combining efficiency $>$ 90% for 5, 10, 20 and 40 channels (N) with an assumption of R=0.95 for type I and T=0.95 for type II.

The other limitation on the channel density is imposed by the maximum numbers of channels:

$$N_{\max} = \Delta\lambda_{Gain}/(\Delta\lambda_F + \Delta\lambda_L) \tag{4.6}$$

where $\Delta\lambda_{Gain}$ is the gain-bandwidth of the Yb fiber ($\approx 60nm$), $\Delta\lambda_F$ is the transition width of the filter (sharpness) and $\Delta\lambda_L$ is the linewidth of the laser. Therefore, it is obvious that both filter sharpness and linewidth are critical to the channel density. In order to pack 30 channels into the gain-bandwidth of the Yb fiber, it merely requires a 1-nm sharpness for the filter and 1-nm spectral width for the laser output, both requirements are relatively easy to achieve for the filter and for the laser, even with very high output peak power.

The thermal load depends greatly on the filter efficiency and

$$H = P_{tot}(1 - \zeta)/(\pi\omega_0^2) \tag{4.7}$$

gives the highest thermal load imposing on the last combining element where H is the thermal load (W/cm^2) and is ζ replaced by T for type I combiner and by R for type II combiner. We can see that one can effectively reduce the thermal load by increasing the reflectivity/transmission on the last filter or increase the beam width on the combining element, both are relatively easier to achieve by using multilayer dielectric filter as combining elements.

Other key characteristics of this combining scheme are determined by the following main spectral filter characteristics:

(i) Sharpness of the spectral edge determines the ultimate spectral density of the combined laser channels.

(ii) Long-wavelength transmission for the configuration Figure 4.6 or, alternatively, short-wavelength reflectivity for the configuration Figure 4.7 will critically determine the achievable maximum combining efficiency and its scalability with the increasing number of combined channels.

(iii) The optical damage level and residual absorption in the combining filters determines the power handling capability of this scheme.

4.3 Spectral Combining Filter Characterization

An off-the-shelf ultra-steep long pass filter (LPF) was characterized using a diffraction-grating base wavelength single-polarization tunable fiber laser. The transmission characteristics with a 14° incident angle is plotted in Figure 4.10, which shows the transmission $> 95\%$ in the pass band and a sharp transition of 0.8 nm from 10% to 90% transmission point. The cut-off wavelength can be precisely tuned by the incident angle of the laser beam and the same multilayer coating covers a wide range of spectrum, which will be ideal to utilize the large bandwidth of Yb-doped amplifiers.

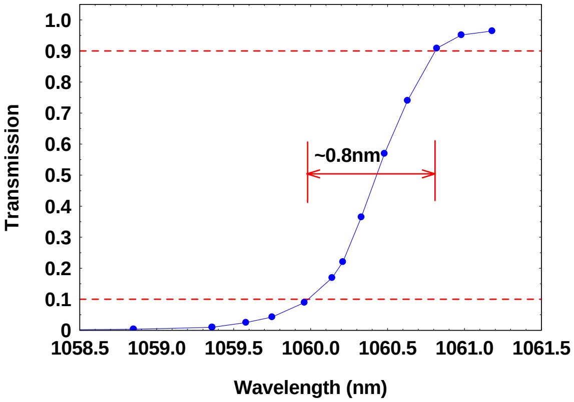

Figure 4.10: Transmission curve for 14° tuning angle showing a sharp transition of 0.8 nm from 10%-90%-transmission points.

The 50% and 90% transmission curve for s- and p- polarizations can be plotted as shown in Figure 4.11 using the parameters provided by the filter manufacturer using the following equation.

$$\lambda(\theta) = \lambda_0 \sqrt{1 - (\frac{\sin\theta}{n_{eff}})^2} \tag{4.8}$$

using n_{eff} 2.0815 for Ts=90% 2.860 for Ts=50% 1.6191 for Tp=90% 1.6199 for Tp=50% Figure 4.11 plots the dependence of cutoff wavelength on the incident angle.

A 45-nm shift in the cutoff wavelength can be achieved by a moderate tuning angle of 28° as shown in Figure 4.12 and filter transmission and sharpness remain the same despite of the wide wavelength tuning, which is a critical characteristics for

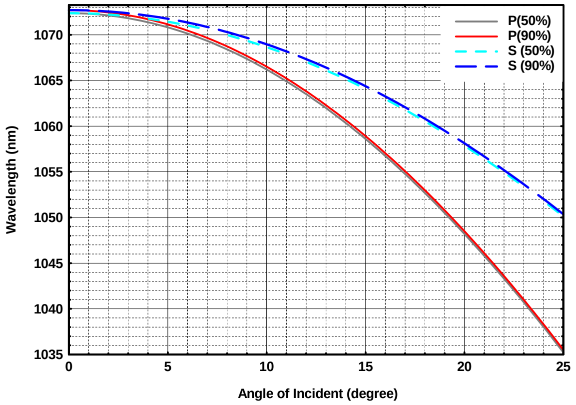

Figure 4.11: The angle tuning characteristics of the particular filter tested. Note that the curve is polarization sensitive, which means that the s and p polarization work at the normal incident angle. As the angle of incident increases, the cutoff wavelengths for both polarizations begin to walk off and the splitting will become more dominant at larger incident angles.

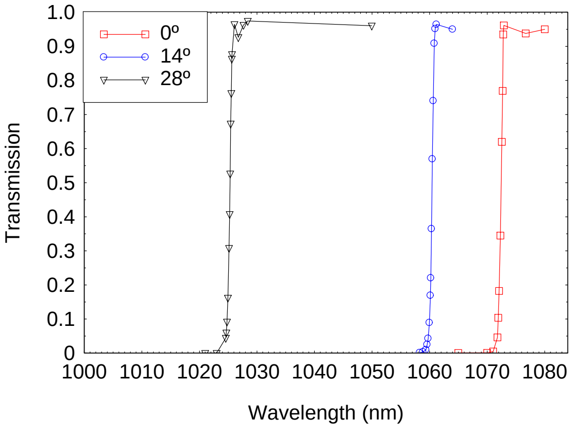

Figure 4.12: Measured filter transmission at three incident angles showing a spectral shift of 45 nm with 28° of tuning for p-polarized light. The transmission is measured to be > 95% independent of incident angle.

the combining density over a broad range of spectrum. Using an experimental setup with 8 reflections at wavelengths of 1050 nm, 1055nm, 1060 nm, 1065 nm (Figure 4.13), and 1070 nm, reflectivity was measured to be $> 99.7\%$ for wavelengths shorter than the cutoff wavelengths. Conclusively, the high reflectivity makes this filter ideal for the combining configuration as shown in Figure 4.7 in which each individual channel will transmit through one filter and reflect through the rest of the combiner. Using the measured transmission of 95% and reflectivity of 99.7%, Equation 4.5 that up to 37 channels can be combined with overall efficiency $> 90\%$ assuming equal power in each channel.

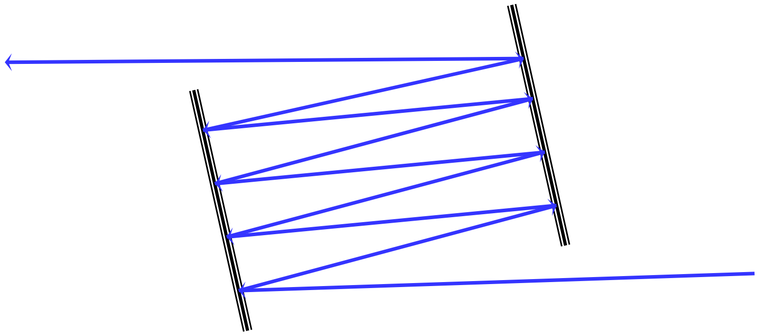

Figure 4.13: Experimental setup for multi-pass reflectivity measurement. Two multi-layer mirror are placed in parallel to each other with separation of 35 cm. Collimated beam of narrow bandwidth single frequency laser is used to test at the wavelengths of 1050 nm, 1055 nm, 1060 nm, 1065 nm and 1070 nm with small incident angle. Reflectivities are measured to be greater than 99.7% for the above mentioned wavelengths.

The filter is manufactured by ion-beam-sputtered dielectric-thin-film-coating [147] and therefore is capable of sustaining high damage fluence greater than 1 J/cm^2 (for 10-ns pulses and the quoted number specified by manufacturer was tested by laser with wavelength of 532 nm, for 1064 nm the expected damage fluence is twice this number, which is 2 J/cm^2)and $> 10 - 100kW/cm^2$ average power density (note: as a rough rule of thumb provided by the filter manufacturer, the damage power density is 10-100 times in the unit of kW/cm^2 of the damage fluence in the unit of

J/cm^2). Such high damage thresholds offer superior energy and power scalability for combining both pulsed and CW lasers. In general, multilayer film filters are polarization sensitive, given that the cut-off wavelengths for s- and p- polarization state are only the same at the designed working incident angle and the difference between cutoff wavelengths for the two polarization states becomes larger as the angle of incidence increases. The walk off in cutoff wavelengths will be detrimental for combining efficiency and should be taken into consideration as will be discussed later in the text.

4.4 Experimental Setup for High Power SBC Demonstration

Previous work in SBC combined individual laser channels with a well-defined wavelength and bandwidth, hence, yielding the overall system cost proportional to the channel numbers. One path to a more compact and cost-effective spectral combining system can be realized from the Master Oscillator Power Amplifier (MOPA) configuration as in most of high energy pulsed amplifiers [79, 80, 79, 66, 72, 75, 148]. Here we propose a compact high-power SBC laser architecture with only one LMA power amplification stage for each spectral channel-amplifier. All channel-amplifiers are seeded from a common seed source. The output of the seed source is distributed spectrally by the MLD filters, (the same kind as those used in the combiner), to seed the channel-amplifiers. This arrangement effectively reduced the overall system complexity since the duplication is only needed at the channel-amplifiers instead of having a whole multi-stage MOPA system for each individual channel.

The seed source is a four-stage MOPA with the same architecture described in [77] comprising an electric-pulse-driven Fabry-Perot semiconductor laser diode emitting at the wavelength centered at 1057 nm. The seed pulse from the laser diode is

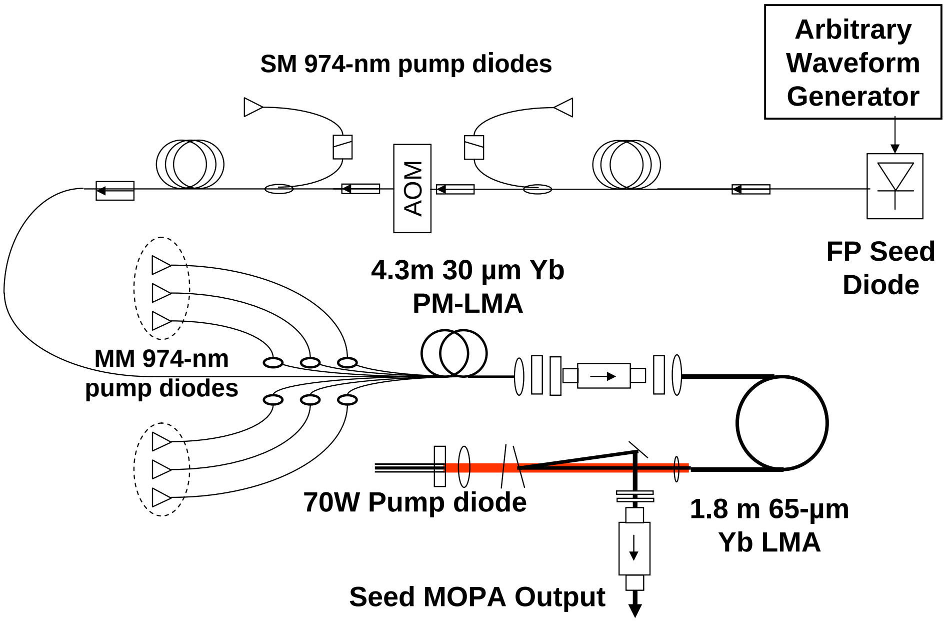

Figure 4.14: The four-stage system consisting of the seed MOPA using a monolithic fiber laser system and single mode output.

pre-amplified by three stages of all monolithic, single-mode operating, polarization maintaining fiber amplifiers (two stages with telecom-graded components and one 30-μm LMA stage). The fourth stage is a free-space-coupled power amplifier with large-mode-area (LMA) fibers, amplifying the pulse to MW peak-powers by a 65-μm-diameter 0.06-NA core. Single-mode operation is achieved by careful mode-excitation and fiber-coiling, giving a measured $M^2 \sim 1.05$.

Figure 4.15 illustrates the SBC setup consisting of the seed splitter, the channel-amplifiers and the output combiner. Seed splitter with MLD filters F_1 and F_3, spectrally divide the beam from seed source into three components, namely blue (the channel with the shortest wavelength), green, and red channels (the channel with the longest wavelength), for the ease of description throughout this paper. The angle of incident for each filter is chosen to optimize the performance of channel-amplifier in accordance to the wavelength-dependent gain of Yb^{3+}. Average power and energy scaling were done with different filter angles to adapt the spectral difference in the seed source at different operating conditions.

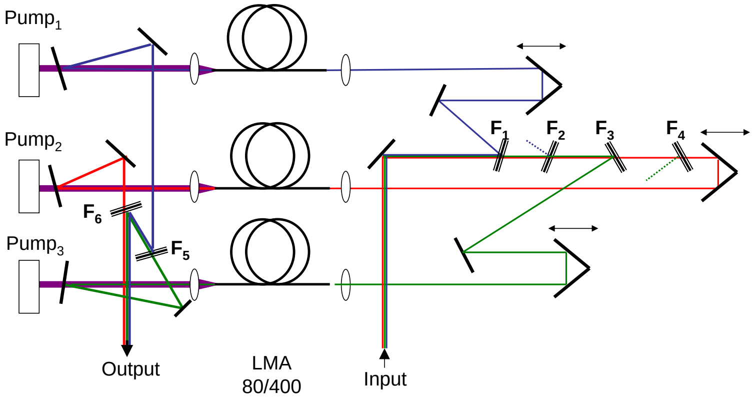

Figure 4.15: Spectral beam combining experimental setup shows splitting filters F_1 and F_3 which are used to separate a broad spectrum of input beam center at 1059 nm into three spectral component seed. The edges of splitting filters are chosen to provide sufficient seed for the LMA 80/400 stage for efficient power/energy extraction. Cleaning filters F_2 and F_4 are used to increase spectral spacing between seed channels to avoid overlapping. Combining filters F_5 and F_6 are used at the output of the amplifier. Note that two combiner filters are only separated ≈ 3 cm.

Since the seeds for the three channels are generated by splitting an output of a broad band spectrum, the intrinsic transition width of MLD filters Figure 4.10 will result in an overlapping of two adjacent seed channels, which will deteriorate the combining efficiency of the combiner. The overlapping can be truncated by introducing additional spectral cleaning filters F_2 and F_4 as shown in Figure 4.15 to improve the combining efficiency while maintaining a small channel separation. Given that the seed source provides a sufficient seed power/energy, this marginal loss in the seed power will not cause any degeneracy on power/energy extraction efficiency.

We use a fiber core with an 80-μm-diameter and 0.06-NA core for the channel-amplifiers based on the consideration of low nonlinearity. The fiber is not polarization-preserving and is not ideal to use with the polarization-sensitive sample filters available to us. However, it is chosen merely for the study the feasibility of high power and high energy scaling of this spectral combining scheme.

Each amplified spectral components are separately collimated to an $1/e^2$ diameter ~ 2 mm and spectrally multiplexed with combiner, (step edge dielectric filters F_5 and F_6). Edges of the spectral components in the combiner are aligned for an optimum combining efficiency. To align the beams coaxially, a charge-coupled device (CCD) camera was used to overlap the beams in the far field and at the focus of a 200 mm plano-convex lens. The optical delay lines at the input of the three channels as shown in Figure 4.15 are used to align the optical path of each channel for the pulse temporal overlapping.

4.5 Results

High average power combining and high energy combining are studied under different seeding conditions. In the study of high average power scaling, the squared-seed-pulses with a higher repetition rate were used to operate below the onset of nonlinearity, while longer pre-shaped pulses with a slow-rising edge were used to optimize the energy extraction at a lower repetition rate.

4.5.1 Power Scaling Demonstration

The pulses with a repetition rate of 100 kHz and durations of 2 ns are chosen to explore power scalability. In order to better characterize the potential of this combining scheme, we defined the combining efficiencies by dividing the output power for each channel after the spectral combiner by the power in single polarization at the output of the channel-amplifier. Since the purpose of this experiment is to study the feasibility of this combing scheme, this decision was justified by two reasons. First is there exists no principal limitation on the mode area for PM fiber and recent development had already advanced PM-LMA fiber to MFA to 2300 μm^2. Secondly, MLD filters can be made polarization-insensitive by custom-design for a specific incident angle, and having the same spectral dependence for both s- and p-polarization.

In our experimental setup, the combiner and splitter are angled to work with s-polarization of the beam. Degree of polarization (DOP) of the seed source is measured to be $> 99\%$. In channel amplifiers, with careful mode excitation and fiber coiling, DOP $> 84\%$ was obtained at the highest available pump power. Combining efficiencies at the highest available pump power are measured to be 97% for the blue channel, 91% for the green channel, and 92.1% for the red channel. The total combined power is 52 W, limited by available pump power, corresponding to ~0.52 mJ and ~221 kW peak power per pulse. Lower combining efficiency for the green and the red channels are due to the $\sim 5\%$ transmission loss through the multilayer coating and the glass substrate. The demonstrated combining efficiencies are $\sim 3\%$ lower than the theoretical limit due to the slight spectral broadening in the channel amplifiers. The spectra of the three seed channels and the output are plotted in Figure 4.16, showing that the channel separation < 2 nm at high combining efficiencies. It is noticed that even at this peak power, slight channel broadening fills the gaps of seed channels and contributes to the 2-3% of difference between the overall combining efficiency and the theoretical limit of the filters used.

The temporal profile of the combined beam shows good overlapping ((Figure 4.17). The temporal property was measured by a InGaAs detector with a 150-ps rise time and an oscilloscope with a 40-GHz bandwidth and the measurement shows no optical path differences at this resolution. We observed only a slight modulation in the temporal shape due to the saturated gain in the channel amplifiers.

The mode quality improvement is done by choosing the lens at the input end of the 80-μm fiber and also changing the divergence by adjusting the distance between

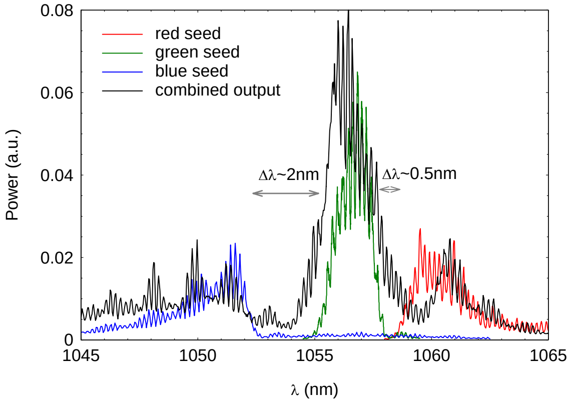

Figure 4.16: Seed spectra for three channels and combined output spectrum. The structures in the spectra are longitudinal modal structure of the Fabry-Parot seed diode.

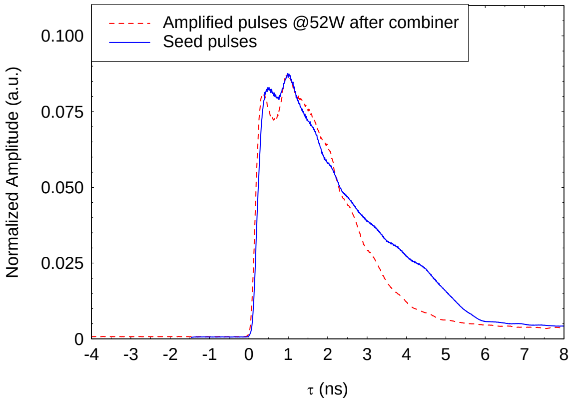

Figure 4.17: Temporal profiles of the input and amplified pulses after combiner showing a good temporal overlapping on a nanosecond scale. Slight temporal shortening of the amplified pulse is due to the gain saturation of the amplifier. The detector used here has a 150-ps rise time, along with a 40-GHz-bandwidth oscilloscope.

the collimating telescope after the 65-μm fiber. A CCD camera was used to optimize the modal distribution to ensure maximum energy distributed in the center-lobe of the core, resulting in an optimized distribution in the fundamental mode (LP_{01}). Figure 4.18 shows the far-field output beam profiles for each individual channel after the combiner and the combined-beam. The combined-beam intensity distribution shows that beam qualities of individual laser channel were preserved after the MLD filters in spite of significantly broad spectral width.

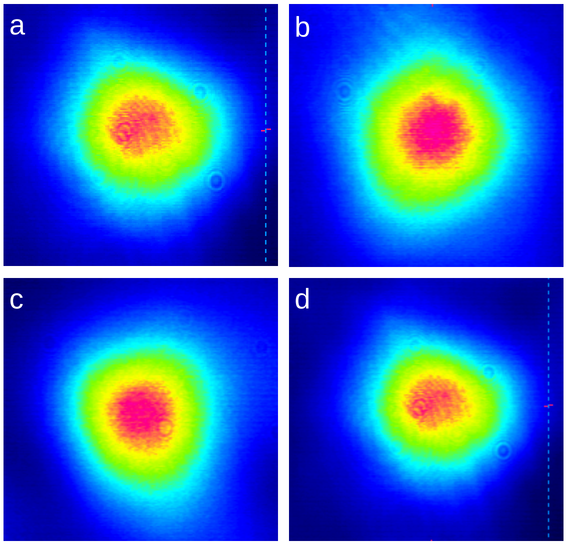

Figure 4.18: Beam profiles after 80-μm fiber for the (a) blue channel (b) green channel (c) red channel, and (d) combined beam profile.

Characterized by M^2, the mode quality of the individual channels after the combiner the combined beam are measured. An Ophir CCD camera was used to measure the full-width half maximum (FWHM) of the beam profiles over a range more than four times Rayleigh range.

For the individual channels, near diffraction limited beams was obtained for red and green channel with the $M^2 \approx 1.20$ and ≈ 1.30 for red channel as shown in Figure 4.19, the $M^2 \approx 1.26$ and ≈ 1.42 for green channel as shown in Figure 4.20.

Since the distance from the output of 65 μm fiber to the input end 80 μm fiber

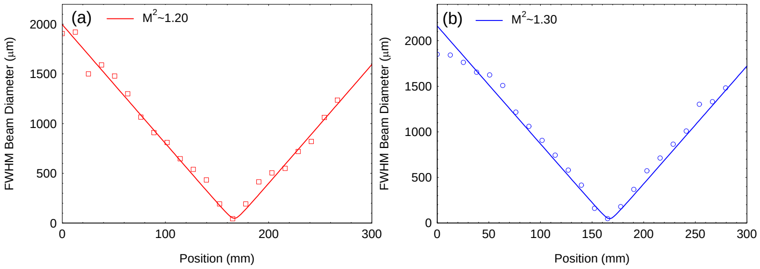

Figure 4.19: Mode quality measurement for red channel output with measured M^2 of 1.20 and 1.30 for the horizontal and vertical axes.

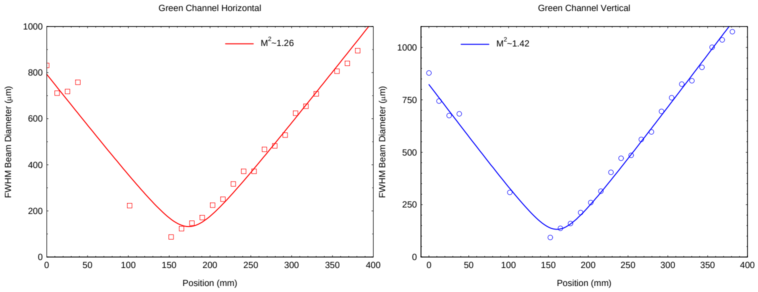

Figure 4.20: Mode quality measurement for green channel with measured M^2 of 1.26 and 1.42 for the horizontal and vertical axes.

is different for each individual channels, the convergence of the beam can not be optimized for all inputs of three channels. Also, due to a tighter coiling radius and less optimized mode excitation condition in the blue channel gain fiber, larger M^2 of ≈ 2.63 and ≈ 2.41 are measured.

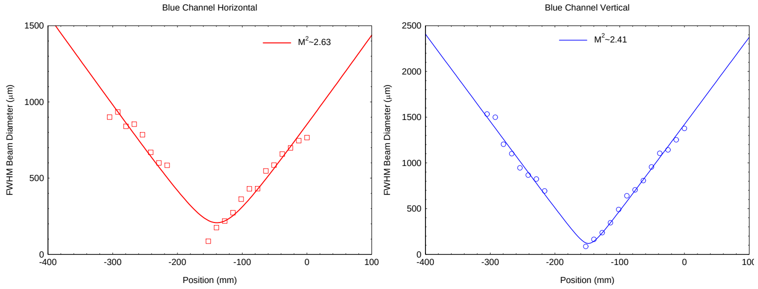

Figure 4.21: Mode quality measurements for the blue channel with measured M^2 of 2.63 and 2.41 for the horizontal and vertical axes.

The degraded mode quality in the blue channel contributed to the degradation of the overall mode quality and M^2 of the combined beam, measured to be ≈ 1.85 (Figure 4.22) for both axes.

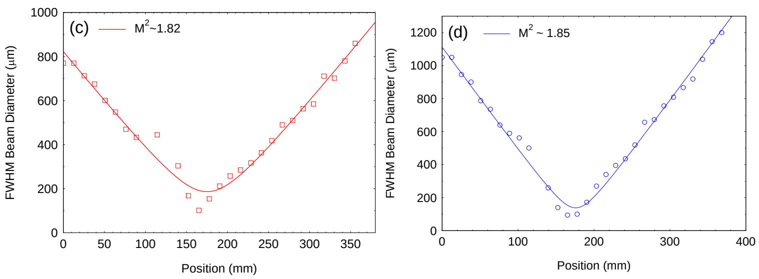

Figure 4.22: Mode quality measurement for the combined beam with measured M^2 of 1.82 and 1.85 for the horizontal and vertical axes.

4.5.2 Spectrally Combined Energy Scaling

In a separate experiment, longer preshaped pulses with a slow rising edge and FWHM duration $\sim$ 6 ns at a repetition rate of 1 kHz were used to study the energy scalability. In the high pulse energy region, spectral broadening becomes detrimental for the combining efficiency since it will result in channel overlapping, therefore, the channel separation was increased to $\sim$ 4 nm to minimize the channel overlapping due to spectral broadening. In the last stage amplifier seeded with $\sim$ 4 nm spectral-width input, we observed 38% of broadening on the FWHM spectral width due to four-wave-mixing [87] when amplified to a peak power of 130 kW (1.11 mJ), and 76% of spectral broadening when amplified to 1.16 MW (5.09 mJ)(Figure 4.23). (The discrepancies between the peak power and the energy are due to the saturated-gain-induced temporal deformation.)

We also noticed that the degree of polarization decreases from 82.5% at 1 mJ to 58% when amplified to 3.6 mJ. We attribute the DOP degradation to the gain saturation of the fundamental mode (with saturation energy $\sim 1.8mJ$ for this fiber). As a result, the higher order modes, possessing different polarization state than the LP_01 mode, are amplified more beyond the saturation of the fundamental mode. Observed by a CCD camera, the degradation of the modal distribution is confirmed

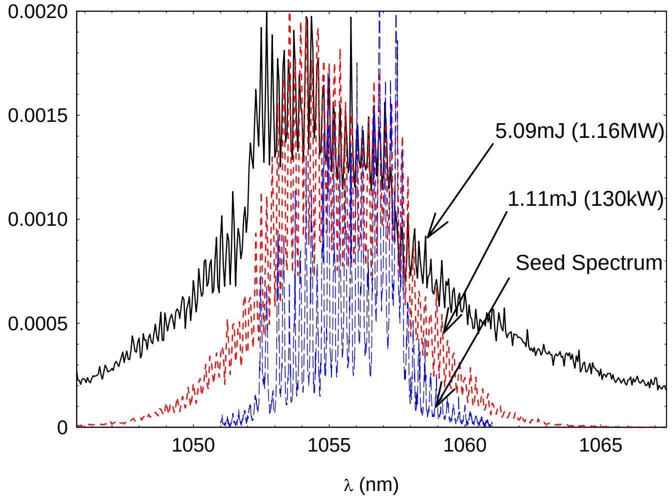

Figure 4.23: Spectral broadening is observed after the 80-μm-core amplifier.

by the change in the modal structure.

In this part of demonstration, channel separation was increased to ≈ 4 nm between blue and green channels and $\approx 2nm$ between green and red channels as shown in Figure 4.24to minimize the channel overlapping due to spectral broadening. Seed energies used for the amplifiers are 250 μJ, 101 μJ and 495 μJ for blue (B), green (G) and red (R) channels.

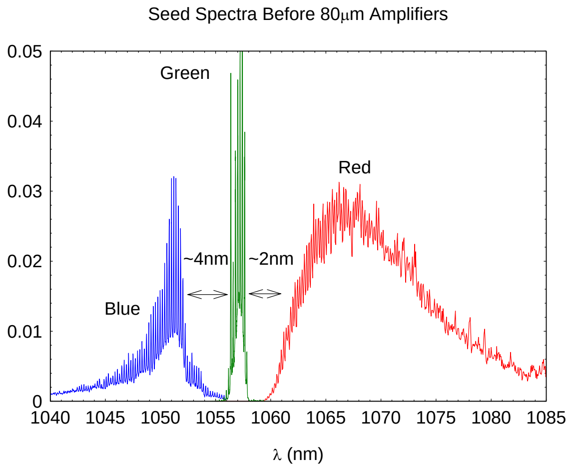

Figure 4.24: Spectra for the three seed channels for energy scaling study.

Seed energies used for the amplifiers are 250 μJ, 101 μJ and 495 μJ for blue (B), green (G) and red (R) channels. Under the limitations of spectral broadening and degradation in DOP, we only report the highest combined energy before the combining efficiencies degenerated. Amplified output energies of individual channels after the combiner are 1.25 mJ (B), 1.02 mJ (G) and 1.76 mJ (R) with combining efficiencies of 92% (B), 87% (G) and 92% (R) respectively, and the combined energy of 4.03 mJ with peak power of 0.714 MW.

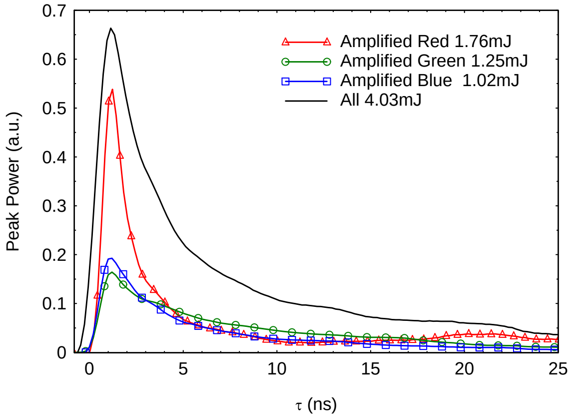

Figure 4.25: The output pulse shapes of individual channels and combined beam show reshaping by gain saturation since all the energy in each individual is higher than saturation energy of the 80-μm-core fiber. Lower output energy after the combiner is due to the polarization degradation.

4.6 Conclusion

In this chapter, we proposed a spectral-beam-combing scheme using non-spatial-dispersive multilayer-dielectric filters. This combining scheme imposes no constraint on the laser line-width and the beam-width to maintain the combined-beam mode-quality. Analysis showed that up to 37 channels can be combined with the measured characteristics of a commercially available filter, and further channel scaling is possible with improved filter sharpness and efficiency. This combining scheme is ideal to work with laser with simultaneous MW peak- power and multi-kW average-power since there exists no trade-off on the laser line-width and the beam-size. Experimental results also verified this effective combining scheme using three channels of spectrally-broad lasers. We achieved $> 91\%$ of combining efficiency, > 52 W of combined power and $M^2 \sim 1.8$ for the combined beam in the study of average-power combining. 4.03 mJ with peak of 0.714 MW is also reported in the study of high-energy combining capability. The combined energy is limited by channel overlapping due to nonlinear spectral. Higher combined peak power and energy is possible using lasers of distinct wavelengths.

In conclusion, this SBC method using MLD filters offer a solution for combining high-peak-power fiber laser with broad spectral bandwidth. Concurrently, high average power can be realized using large beam-width on the combining element without thermal damage or wavefront distortion. It is not unreasonable to picture 25-kW combined-power from a spectrally-combined all-fiber-laser-based system for a EUV lithography light source.

CHAPTER V

Conclusion and Future Work

In this last chapter, the key results demonstrated in the work of dissertation and their significance will be summarized. The future outlook associated with the research topics in this dissertation will also be discussed.

5.1 Contributions and Conclusions

Motivated by the urgent need for the production-worthy lithography steppers of the next-generation, the work in this dissertation focused on the development of the fiber-laser technologies for a high-power EUV-lithography light source. The research in this dissertation covered the design and the study of a pulsed-fiber-laser EUV driver; efficient EUV demonstrations using Sn targets; and the concept and the validation of a non-spatial-dispersive spectral-combining scheme to combine lasers with a concurrent MW peak power and a kW average power.

In Chapter II, using Yb-doped large-mode-area fibers, we developed a single-emitter-fiber integrated module (SEFIM), constituting the basic building block for a 25-kW fiber-laser system. Given the pulse parameters of the solid-state lasers used in a previous efficient-EUV demonstration, the 80-μm-core LMA fiber used in this study can provide the required intensity level with its MW peak power and its close-to-diffraction-limited beam quality, and therefore is the fiber-of-choice for SEFIM.

In spite of its very large mode-field area of 2750 μm^2, the output beam of the 80-μm-core fiber has a beam quality of $M^2 \approx 1.3$, achieved by careful mode-matching and tight fiber-coiling. A large mode-field-area provides higher nonlinear thresholds, allowing the output peak powers at the multi-MW level. We demonstrated a record high peak-power of 6 MW with 110-ps pulses from a gain-switched Fabry-Perot laser diode. MW peak-powers were also obtained at longer pulse durations of up to 6 ns. We found that the limitation of the peak power extraction for this fiber length is the nonlinearity of stimulated Raman scattering.

The ultimate limit of the peak power extractable from a fiber-laser amplifier is caused by catastrophic self-focusing. Our numerical analysis using the Fast-Fourier-Transform Beam-Propagation-Method showed that the beam diameter will gradually decrease as the peak power is approaching its self-focusing critical peak power in a cylindrical waveguide.

We also investigated the energy extraction and the temporal pulse deformation due to the gain-saturation from the LMA fiber experimentally and numerically using an arbitrary waveform generator. We found that the behavior of pulse-shaping in a saturated-gain amplifier can be accurately predicted with a simple numerical model based on saturation fluence. The same model can also synthesize the required input-pulse shape for a specific output-pulse shape in a multi-state cascaded-amplifier. We also found that the energy extraction, independent of the input-pulse shape, agreed well with the Frantz-Nodvick Model.

The implementation of the arbitrary waveform generator as the seed driver enabled the pulse-shaping capability. This capability can not only allow us to provide a preshaped input pulse to compensate gain saturation, it can also generate pre-pulses that will help optimize the plasma condition in the EUV-generation study. An average power of 140W is obtained from the system with a special design of forced cooling. The first atmospheric breakdown by a fiber laser is also reported using the high peak-power and the high focusability of the fiber-laser output.

In Chapter III, we verified the SEFIM we developed as being an efficient EUV driver by two experimental demonstrations. We first achieved a conversion efficiency (CE) of $\sim 1\%$ using a planar soild-Sn target at an intensity of $\sim 1.2 \times 10^{10} W/cm^2$. This result, to the best of our knowledge, is the first EUV-generation using a fiber laser. However, the debris generated from a solid-Sn target contaminated the optics quickly and make it unfeasible for long-term operation.

In a second demonstration to investigate a realistic target solution, we used the Sn-doped water-droplet targets developed by UCF in the next set of experiments. These water-droplet targets are suitable to use in a production-worthy EUV system due to their compatibility of a high-repetition-rate operation and their intrinsic debris-free characteristics. We demonstrated a conversion efficiency of $\sim 2.1\%$ at a pulse duration of 6 ns, proving that the fiber lasers are equally efficient as the solid-state lasers in EUV genration, regardless of a very different laser parameter space between the two types of lasers. The highest conversion efficiency was achieved at the intensity of $8.8 \times 10^{10} W/cm^2$, and CE declined beyond this intensity, indicating this as optimum condition for efficient EUV generation.

This study using other pulse durations revealed that conversion efficiency is highly dependent on the pulse duration; the 6-ns laser pulses generated a conversion efficiency three times higher than the CE generated by the 1.7-ns pulses, even though a higher intensity was achievable by the shorter pulses. Conversion efficiencies can also be scaled by preheating the plasma using prepulses. We found that using the 45-ns-delay and a 1-to-10-ratio prepulse will improve the conversion efficiency by a factor of two. This finding is consistent with the reported studies using the prepulses from the solid-state lasers.

The important difference of generating prepulses from the two types of lasers is that the prepulses can be generated from the same output of the fiber laser, while a wavelength- /or polarization-combining is required to generate prepulses in solid-state lasers. This successful demonstration of high conversion efficiency with relatively low energy pulses constitutes the first step on a technological path toward fiber-laser-driven high-power EUV sources for high-throughput lithography steppers.

In Chapter IV, we proposed a new high-power spectral-beam-combining scheme based on sharp-spectral-edge multilayer dielectric filters. This scheme does not use spectral spatial dispersion, and therefore, is free from constraints on the laser linewidth and the beam size inherent in conventional diffraction-grating-based beam-combining approaches. Consequently, it enables multi-kW combined powers using already-existing fiber and coating technologies with a $\sim 2nm$ spectral inter-channel separation.

We proposed two combining arrangements based on this approach, both suitable for long-pass filters or short-pass filters. The choice of the arrangement depends on the filter efficiencies. The filter sample has a measured reflectivity $> 99.7\%$, a transmission $> 95\%$ and a sharp spectral-transtion width of 1 nm, giving a potential of combining 37 equal-power-channels with a overall efficiency $> 90\%$. An experimental study of this combining scheme shows a $> 91\%$ efficient combination of three nanosecond-pulse fiber laser beams with 52-W combined power and 4.0-mJ combined energy. This scheme is particularly well-suited for high-energy-pulse power-combining due to the inherently broad bandwidth, providing an unrivaled solution to reach the power level required by an all-fiber-laser-based EUV driver.

5.2 Future Outlook

A great deal of experimental and theoretical work remains to achieve a fully integrated system for the EUV lithography source. We only listed the critical challenges foreseen during our research work in the following sections.

5.2.1 Power Scaling of SEFIM and Limitations

In Chapter II, the highest average power achieved was 140 W, and we attributed the limitation to the fiber polymer coating. This conclusion was drawn from the fact that each successive fiber damage occurred at a lower pump power level during the fiber-damage test. With improved coating process, we should be able to extract the power from the amplifier with the only limitation of the highest available pump power.

As mentioned before, with the available pump power and the demonstrated slope efficiency, we should be able to reach an average power output at 280 W. Further power scaling is also possible by having a higher pump power. However, the ultimate limitation will then be on the thermal-dissipation capability of the current thermal design. Also, one can implement dual-end pumping to have a more distributed thermal density along the fiber, alleviating the thermal design requirement imposed by single-end pumping. Free-space-coupling of the pump power was used in the power amplifications stages in the current SEFIM, which was only temporary for this experimental study.

For an industry-applicable system, it must be made monolithic to achieve the anticipated robustness. Current monolithic pump-combiner technologies allow the combination of the pump power from numbers of diode lasers to a multi-kW level. However, these combiners have only been applied to CW fiber lasers. For the pulsed fiber laser, the splice-point for this combiner will become a potential problem for very high peak power pulses, especially at the output of the final stage amplifier with MW-peak powers. One can also reduce the power through a combiner by reversing the pump direction, (i.e. co-propagating pumping), with the trade off of a longer effective length and a lower nonlinear threshold.

The use of a conventional step-index fiber merely served the purpose of the feasibility study. For a practical monolithic system, effectively single-mode LMA fibers, such as CCC fibers [59], should be implemented for a truly robust system. Moreover, a good control on the spectral properties is sought-after to reduce the channel overlapping and increase the combining efficiency as mentioned in Chapter IV. We attributed the nonlinear broadening in our system to the multiple longitudinal modes of the Fabry-Perot seed diode. Implementation of other seed sources, such as DFB or DBR diodes with very fast rise times, should provide a better spectral-width control.

5.2.2 Power Scaling of EUV Generation

In Chapter III, we achieved efficient EUV generation at a repetition rate of 1.7 kHz and an average laser power of 10 W. Higher power can be reached at a higher repetition rate and high pump power, and with the improvement of the fiber coating. Vacuum condition remains an uncertain issue for the existing experimental chamber, as a higher droplet repetition rate ($\sim$ 50 kHz required for 300 W average power) will create more vapors in the chamber and imposes the limitation on the highest repetition rate.

The debris issue at the current repetition rate limited the experiment run time to $\sim$ 30 minutes before the focusing lens was coated with debris. Running at a higher repetition rate will linearly expedite the degradation of the lens transmission.

This problem can be addressed by using a longer-focal-length lens, providing higher energy per pulse by spectral combining, or using smaller droplet targets ($\sim$20 μm to provide a better laser-to-target overlapping).

5.2.3 Power Scaling of Combining System

The novel spectral-beam-combining consisting of MLD filters in Chapter IV provided a viable solution for high-peak-power beam-combining. Further power scaling to a multi-kW-class pulsed-fiber laser should be pursued by exploiting this combining scheme.

The combining efficiency can be optimized toward the theoretical limit by having the laser channels with distinct and controlled spectral properties. This would eliminate the loss of the combining efficiency caused by the overlapping between the channels. Further improvement of efficiency can also be realized using polarization-maintaining fibers to avoid the walk off in the cutoff wavelengths of the two polarization states.

Another approach can be done by custom-making each combining filter with a design cutoff wavelength, removing the necessity on PM fibers. It is important to keep in mind that the filter used in the testing is an off-the-shelf product and was originally designed for Raman Spectroscopy. In this sense, custom filters become beneficial since their spectral characteristics can be tailored for this particular application. Sharper transition widths can be reached by having just enough bandwidth for Yb^{3+}, one order of magnitude narrower than the current filter provides. In fact, a 0.3-nm spectral-transition width is already achieved by the same filter manufacturer. A higher transmission can also be realized by having a custom anti-reflection coating for the designed wavelength range, which will greatly improve the overall efficiency and the maximum combinable channels.

For a system with a few tens of combined channels, manual alignment will become impractical and automation on the output of the individual channels and filters has to be implemented. From our experimental experiences, free-spaced end-pumping would not be ideal for this type of combining scheme, and a monolithic fiber-laser system is sought-after to be compatible with this combining system. With this proposed approach, a robust multi-kW fiber laser system with MW peak power pulses shall be accessible in the near future.

5.2.4 Self-focusing Observation and Theoretical Work

Another intriguing physical aspect that had been observed in current fiber amplifiers is the absence of self-focusing at the expected power level. One possible explanation is due to the composition and the dopant of the active fiber: the nonlinear refractive index is slightly different from that of a fused silica, yielding an increase in the self-focusing threshold. However, one should be able to observe the change in the divergence of the output beam at a peak power a few times below the self-focusing threshold, according to several theoretical works.

Using a CCD camera to observe this change in the divergence is indeed insufficient since the pulse duration is in the order of nanoseconds, which is too short for a CCD camera to resolve. One should implement a time-resolved high-resolution imaging system, e.g. a streak camera, to be able to have a time-resolved image with sub-ns resolution Otherwise, the change in the divergence will be averaged out with the background ASE.

While all previous work in self-focusing is done assuming continuous wave, it is desirable to have more sophisticated theoretical or numerical models to accurately visualize the change in the beam radius temporally. Moreover, most of the reported peak powers approaching the self-focusing limit are from the amplifiers operating in their saturated region. A dramatic change in the temporal region and possibly in the transverse shape of the pulse (since the wing of the spatial profile has a lower energy fluence, giving a less-saturated gain), one should include the temporal domain into the nonlinear Schrödiger equation. The Finite-Difference-Time-Domain method will be needed to numerically solve the problem.

Theoretical work should also consider the inclusion of the population-induced change in the refractive index. Several works in the high-speed optical switches utilizing the pump-induced refractive index change shows that the nonlinear-index is related to the population inversion. For amplifier in a saturated region, the population inversion become a function of input pulse fluence. This effect will potentially alter the transversal distribution of the nonlinear refraction index due to population inversion, hence, enhance or impede the phase modulation due to the Kerr nonlinear-effect. However, the literature has not reached a consensus on the sign of the phase change, or on the physical origins of this effect. More theoretical and experimental work will also be needed for a better understanding of the ultimate peak power limit of pulsed-fiber lasers.

BIBLIOGRAPHY

BIBLIOGRAPHY

[1] F. Jin and M. Richardson. New laser plasma source for extreme-ultraviolet lithography. *Appl. Opt.*, 34(25):5750+, 1995.

[2] Chiew-Seng Koay, Simi George, Kazutoshi Takenoshita, Robert Bernath, Etsuo Fujiwara, Martin Richardson, and Vivek Bakshi. High conversion efficiency microscopic tin-doped droplet target laser-plasma source for EUVL. volume 5751, pages 279–292. SPIE, 2005.

[3] Simi A. George, Kai-Chung Hou, Kazutoshi Takenoshita, Almantas Galvanauskas, and Martin C. Richardson. 13.5 nm EUV generation from tin-doped droplets using a fiber laser. *Opt. Express*, 15(25):16348–16356, December 2007.

[4] Emily A. Gibson, Ariel Paul, Nick Wagner, Ra'anan Tobey, David Gaudiosi, Sterling Backus, Ivan P. Christov, Andy Aquila, Eric M. Gullikson, David T. Attwood, Margaret M. Murnane, and Henry C. Kapteyn. Coherent soft x-ray generation in the water window with quasi-phase matching. *Science*, 302(5642):95–98, October 2003.

[5] David Attwood. *Soft X-Rays and Extreme Ultraviolet Radiation: Principles and Applications.* Cambridge University Press, March 2007.

[6] R. H. Stulen. 13-nm extreme ultraviolet lithography. *IEEE J. Sel. Top. Quantum Electron.*, 1(3):970–975, 1995.

[7] Alec N. Broers. Fabrication limits of electron beam lithography and of UV, X-Ray and ion-beam lithographies. *Philosophical Transactions: Physical Sciences and Engineering*, 353(1703):291–311, 1995.

[8] Takashi Ito and Shinji Okazaki. Pushing the limits of lithography. *Nature*, 406(6799):1027–1031, 2000.

[9] Banqiu Wu and Ajay Kumar. Extreme ultraviolet lithography: A review. *Journal of Vacuum Science & Technology B: Microelectronics and Nanometer Structures*, 25(6):1743–1761, 2007.

[10] C. W. Gwyn, R. Stulen, D. Sweeney, and D. Attwood. Extreme ultraviolet lithography. volume 16, pages 3142–3149. AVS, 1998.

[11] International technology roadmap for semiconductors. *available online*, 23(Makuhari Messe, Chiba, Japan):2007 ITRS Winter Public Conference, Dec 2007.

[12] R. H. Stulen. 13-nm extreme ultraviolet lithography. *IEEE J. Sel. Top. Quantum Electron.*, 1(3):970–975, 1995.

[13] Bernard Fay. Advanced optical lithography development, from UV to EUV. *Microelectronic Engineering*, 61-62:11–24, July 2002.

[14] T. Hanawa K.Moriizumi A. Nakae, K. Kamon and H. Tanabe. Improvement in optical proximity correction by optimizing second illumination source. *Jpn. J. Appl. Phys.*, 35(35):6396, January 1996.

[15] T. M. Bloomstein, M. Rothschild, R. R. Kunz, D. E. Hardy, R. B. Goodman, and S. T. Palmacci. Critical issues in 157 nm lithography. volume 16, pages 3154–3157. AVS, 1998.

[16] Toshiro Itani and Wataru Wakamiya. Progress in 157-nm lithography development for 70-nm node. *Microelectronic Engineering*, 61-62:49–55, July 2002.

[17] Walter J. Trybula. Status of 157-nm optical lithography. *Journal of Microlithography, Microfabrication, and Microsystems*, 4(1), 2005.

[18] D. Brambley, B. Martin, and P. D. Prewett. Microlithography: An overview. *Advanced Materials for Optics and Electronics*, 4(2):55–74, 1994.

[19] Mumit Khan, Geng Han, Gene Tsvid, Toyoki Kitayama, Juan Maldonado, and Franco Cerrina. Can proximity X-ray lithography print 35 nm features? yes, 2001.

[20] Stephen Y. Chou, Peter R. Krauss, and Preston J. Renstrom. Imprint of sub-25 nm vias and trenches in polymers. *Appl. Phys. Lett.*, 67(21):3114–3116, 1995.

[21] Michael D. Austin, Haixiong Ge, Wei Wu, Mingtao Li, Zhaoning Yu, D. Wasserman, S. A. Lyon, and Stephen Y. Chou. Fabrication of 5 nm linewidth and 14 nm pitch features by nanoimprint lithography. *Appl. Phys. Lett.*, 84(26):5299–5301, 2004.

[22] L. . J. Guo. Nanoimprint lithography: Methods and material requirements. *Advanced Materials*, 19(4):495–513, 2007.

[23] Peter J. Silverman. Extreme ultraviolet lithography: overview and development status. *Journal of Microlithography, Microfabrication, and Microsystems*, 4(1), 2005.

[24] Igor V. Fomenkov, David C. Brandt, Alexander N. Bykanov, Alexander I. Ershov, William N. Partlo, David W. Myers, Norbert R. Böwering, Georgiy O. Vaschenko, Oleh V. Khodykin, Jerzy R. Hoffman, Ernesto, Rodney D. Simmons, Juan A. Chavez, and Christopher P. Chrobak. Laser-produced plasma source system development. volume 6517. SPIE, 2007.

[25] A. Endo. High-average power EUV light source for the next-generation lithography by laser-produced plasma. *IEEE J. Sel. Top. Quantum Electron.*, 10(6):1298–1306, 2004.

[26] Takashi Suganuma Krzysztof Nowak Tatsuya Yanagida Takayuki Yabu Takeshi Asayama Yoshifumi Ueno Masato Moriya Masaki Nakano Hiroshi Someya Toshihiro Nishisaka Tamotsu Abe Georg Soumagne Hiroshi Komori Hakaru Mizoguchi Akira Sumitani Akira Endo, Hideo Hoshino and Koichi Toyoda. Laser produced plasma light source for HVM-EUVL. Number 6. Sematech, 2007.

[27] Simi A. George, William T. Silfvast, Kazutoshi Takenoshita, Robert T. Bernath, Chiew-Seng Koay, Gregory Shimkaveg, and Martin C. Richardson. Comparative extreme ultraviolet emission measurements for lithium and tin laser plasmas. *Opt. Lett.*, 32(8):997–999, 2007.

[28] R. C. Spitzer, T. J. Orzechowski, D. W. Phillion, R. L. Kauffman, and C. Cerjan. Conversion efficiencies from laser-produced plasmas in the extreme ultraviolet regime. *J. Appl. Phys.*, 79(5):2251–2258, 1996.

[29] P. A. C. Jansson, B. A. M. Hansson, O. Hemberg, M. Otendal, A. Holmberg, J. de Groot, and H. M. Hertz. Liquid-tin-jet laser-plasma extreme ultraviolet generation. *Appl. Phys. Lett.*, 84(13):2256–2258, 2004.

[30] Hiroki Tanaka, Atsushi Matsumoto, Kouzi Akinaga, Akihiko Takahashi, and Tatsuo Okada. Comparative study on emission characteristics of extreme ultraviolet radiation from CO_2 and Nd:YAG laser-produced tin plasmas. *Appl. Phys. Lett.*, 87(4):041503, 2005.

[31] Tsuyoshi Ando, Shinsuke Fujioka, Hiroaki Nishimura, Nobuyoshi Ueda, Yuzuri Yasuda, Keiji Nagai, Takayoshi Norimatsu, Masakatsu Murakami, Katsunobu Nishihara, Noriaki Miyanaga, Yasukazu Izawa, Kunioki Mima, and Atsushi Sunahara. Optimum laser pulse duration for efficient extreme ultraviolet light generation from laser-produced tin plasmas. *Appl. Phys. Lett.*, 89(15):151501, 2006.

[32] Tomoharu Okuno, Shinsuke Fujioka, Hiroaki Nishimura, Yezheng Tao, Keiji Nagai, Qincui Gu, Nobuyoshi Ueda, Tsuyoshi Ando, Katsunobu Nishihara, Takayoshi Norimatsu, Noriaki Miyanaga, Yasukazu Izawa, Kunioki Mima, Atsushi Sunahara, Hiroyuki Furukawa, and Akira Sasaki. Low-density tin targets for efficient extreme ultraviolet light emission from laser-produced plasmas. *Appl. Phys. Lett.*, 88(16):161501, 2006.

[33] Y. Tao, S. S. Harilal, M. S. Tillack, K. L. Sequoia, B. O'Shay, and F. Najmabadi. Effect of focal spot size on in-band 13.5 nm extreme ultraviolet emission from laser-produced Sn plasma. *Opt. Lett.*, 31(16):2492–2494, 2006.

[34] Kai-Chung Hou, Ming-Yuan Cheng, Almantas Galvanauskas, Doruk Engin, Rupak Changkakoti, and Pri Mamidipudi. Multi-MW peak power scaling of single-transverse mode pulses using 80-μm core Yb-doped LMA fibers. In *Advanced Solid-State Photonics*, page MF5. Optical Society of America, 2006.

[35] Charles J. Koester and Elias Snitzer. Amplification in a fiber laser. *Appl. Opt.*, 3(10):1182+, October 1964.

[36] L. Reekie, R. Mears, S. Poole, and D. Payne. Tunable single-mode fiber lasers. *J. Lightwave Technology*, 4(7):956–960, 1986.

[37] M. C. Farries, P. R. Morkel, and J. E. Townsend. Samarium^{3+}-doped glass laser operating at 651 nm. *Electron. Lett.*, 24(11):709–711, 1988.

[38] Makoto Yamada, Makoto Shimizu, Yasutake Ohishi, Terutoki Kanamori, Shouichi Sudo, and Jiro Temmyo. Gain characteristics of Pr^{3+}-doped fluoride fiber amplifier. *Electronics and Communications in Japan (Part II: Electronics)*, 77(4):75–87, 1994.

[39] E. Desurvire and J. R. Simpson. Amplification of spontaneous emission in erbium-doped single-mode fibers. *J. Lightwave Technology*, 7(5):835–845, 1989.

[40] M. J. F. Digonnet. Closed-form expressions for the gain in three- and four-level laser fibers. *IEEE J. Quantum Electron.*, 26(10):1788–1796, 1990.

[41] B. J. Ainslie and B. J. Ainslie. A review of the fabrication and properties of erbium-doped fibers for optical amplifiers. *J. Lightwave Technology*, 9(2):220–227, 1991.

[42] H. M. Pask, R. J. Carman, D. C. Hanna, A. C. Tropper, C. J. Mackechnie, P. R. Barber, and J. M. Dawes. Ytterbium-doped silica fiber lasers: versatile sources for the 1-1.2 μm region. *IEEE J. Sel. Top. Quantum Electron.*, 1(1):2–13, 1995.

[43] C. Ghisler, W. Luthy, and H. P. Weber. Tuning of a $Tm^{3+} : Ho^{3+}$: silica fiber laser at 2 μm. *IEEE J. Quantum Electron.*, 31(11):1877–1879, 1995.

[44] Andreas Tünnermann. High-power CW fiber lasers - present and future. *Laser Technik Journal*, 2(2):54–56, 2005.

[45] L. Zenteno. High-power double-clad fiber lasers. *J. Lightwave Technology*, 11(9):1435–1446, 1993.

[46] Philip Russell. Photonic crystal fibers. *Science*, 299(5605):358–362, January 2003.

[47] Jonathan C. Knight. Photonic crystal fibres. *Nature*, 424(6950):847–851, 2003.

[48] V. Dominic, S. MacCormack, R. Waarts, S. Sanders, S. Bicknese, R. Dohle, E. Wolak, P.S. Yeh, and E. Zucker. 110 W fibre laser. *Electron. Lett.*, 35(14):1158–1160, 1999.

[49] I. Zawischa, K. Plamann, C. Fallnich, H. Welling, H. Zellmer, and A. Tünnermann. All-solid-state neodymium-based single-frequency master-oscillator fiber power-amplifier system emitting 5.5 W of radiation at 1064 nm. *Opt. Lett.*, 24(7):469–471, April 1999.

[50] S. Höfer, A. Liem, J. Limpert, H. Zellmer, A. Tünnermann, S. Unger, S. Jetschke, H. R. Müller, and I. Freitag. Single-frequency master-oscillator fiber power amplifier system emitting 20 W of power. *Opt. Lett.*, 26(17):1326–1328, 2001.

[51] Y. Jeong, J.K. Sahu, R.B. Williams, D.J. Richardson, K. Furusawa, and J. Nilsson. Ytterbium-doped large-core fibre laser with 272-W output power. *Electron. Lett.*, 39(13):977–978, 2003.

[52] J. Limpert, A. Liem, H. Zellmer, and A. Tunnermann. 500 W continuous-wave fibre laser with excellent beam quality. *Electron. Lett.*, 39(8):645–647, 2003.

[53] Y. Jeong, J. Sahu, D. Payne, and J. Nilsson. Ytterbium-doped large-core fiber laser with 1.36 kW continuous-wave output power. *Opt. Express*, 12(25):6088–6092, December 2004.

[54] Y. Jeong, J.K. Sahu, D.N. Payne, and J. Nilsson. Ytterbium-doped large-core fibre laser with 1-kW of continuous-wave output power. *Electron. Lett.*, 40(8):470–472, 2004.

[55] Y. Jeong, J. K. Sahu, S. Baek, C. Alegria, D. B. S. Soh, C. Codemard, and J. Nilsson. Cladding-pumped ytterbium-doped large-core fiber laser with 610 W of output power. *Opt. Commun.*, 234(1-6):315–319, April 2004.

[56] C.-H. Liu, B. Doerfel, F. Heinemann, S. Carter, A. Tankala, J. K. Farroni, and A. Galvanauskas. 810 W continuous-wave and single-transverse-mode fibre laser using 20-μm core Yb-doped double-clad fibre. *Electron. Lett.*, 40(23):1471–1472, 11 Nov. 2004.

[57] S. Ramachandran, J. W. Nicholson, S. Ghalmi, M. F. Yan, P. Wisk, E. Monberg, and F. V. Dimarcello. Light propagation with ultra large modal areas in optical fibers. *Opt. Lett.*, 31(12):1797–1799, June 2006.

[58] Liang Dong, Jun Li, and Xiang Peng. Bend-resistant fundamental mode operation in ytterbium-doped leakage channel fibers with effective areas up to 3160 μm^2. *Opt. Express*, 14(24):11512–11519, November 2006.

[59] Chi-Hung Liu, Guoqing Chang, Natasha Litchinitser, Almantas Galvanauskas, Doug Guertin, Nick Jabobson, and Kanishka and Tankala. Effectively single-mode chirally-coupled core fiber. OSA Technical Digest Series (CD), pages ME2+. Optical Society of America, January 2007.

[60] T. Schmid, S. A. George, J. Cunado, S. Teerawattanasook, R. Bernath, C. Brown, K. Takenoshita, C. S. Koay, and M. Richardson. High repetition rate LPP source facility for EUVL. volume 6517. SPIE, 2007.

[61] Aghapi G. Mordovanakis, Kai-Chung Hou, Yu-Chung Chang, Ming-Yuan Cheng, John Nees, Bixue Hou, Anatoly Maksimchuk, Gerard Mourou, Almantas Galvanauskas, and Bruno Lafontaine. Demonstration of fiber-laser-produced plasma source and application to efficient extreme UV light generation. *Opt. Lett.*, 31(17):2517–2519, 2006.

[62] C. C. Ranaud, H. L. Offerhaus, J. A. Alvarez-Chavez, C. J. Nilsson, W. A. Clarkson, P. W. Turner, D. J. Richardson, and A. B. Grudinin. Characteristics of Q-switched cladding-pumped ytterbium-doped fiber lasers with different high-energy fiber designs. *IEEE J. Quantum Electron.*, 37(2):199–206, 2001.

[63] A. E. Siegman. *Lasers.* University Science Books, October 1990.

[64] S. Webster, F.C. McDonald, A. Villanger, M.J. Soileau, E.W. Van Stryland, D.J. Hagan, B. McIntosh, W. Torruellas, J. Farroni, and K. Tankala. Optical damage measurements for high peak power ytterbium doped fiber amplifiers. volume 5991, page 599115. SPIE, 2005.

[65] A. Galvanauskas. Mode-scalable fiber-based chirped pulse amplification systems. *IEEE J. Sel. Top. Quantum Electron.*, 7(4):504–517, 2001.

[66] Ming-Yuan Cheng, Yu-Chung Chang, Almantas Galvanauskas, Pri Mamidipudi, Rupak Changkakoti, and Peter Gatchell. High-energy and high-peak-power nanosecond pulsegeneration with beam quality control in 200-μm core highly multimode yb-doped fiberamplifiers. *Opt. Lett.*, 30(4):358–360, February 2005.

[67] A. Galvanauskas, M. Y. Cheng, K. C. Hou, and K. H. Liao. High peak power pulse amplification in large-core Yb-doped fiber amplifiers. *IEEE J. Sel. Top. Quantum Electron.*, 13(3):559–566, 2007.

[68] Martin E. Fermann. Single-mode excitation of multimode fibers with ultrashort pulses. *Opt. Lett.*, 23(1):52–54, January 1998.

[69] Jeffrey P. Koplow, Dahv A. Kliner, and Lew Goldberg. Single-mode operation of a coiled multimode fiber amplifier. *Opt. Lett.*, 25(7):442–444, April 2000.

[70] J. Limpert, O. Schmidt, J. Rothhardt, F. Röser, T. Schreiber, A. Tünnermann, S. Ermeneux, P. Yvernault, and F. Salin. Extended single-mode photonic crystal fiber lasers. *Opt. Express*, 14(7):2715–2720, April 2006.

[71] A. W. Snyder and J. D. Love. Reflection at a curved dielectric interface— electromagnetic tunneling. *IEEE Trans. Microwave Theory Tech.*, 23(1):134–141, 1975.

[72] A. Galvanauskas, M. Y. Cheng, K. C. Hou, and K. H. Liao. High peak power pulse amplification in large-core Yb-doped fiber amplifiers. *IEEE J. Sel. Top. Quantum Electron.*, 13(3):559–566, 2007.

[73] C. C. Ranaud, H. L. Offerhaus, J. A. Alvarez-Chavez, C. J. Nilsson, W. A. Clarkson, P. W. Turner, D. J. Richardson, and A. B. Grudinin. Characteristics of Q-switched cladding-pumped ytterbium-doped fiber lasers with different high-energy fiber designs. *IEEE J. Quantum Electron.*, 37(2):199–206, 2001.

[74] J. Nilsson, R. Paschotta, J. E. Caplen, and D. C. Hanna. Yb^{3+}-ring-doped fiber for high-energy pulse amplification. *Opt. Lett.*, 22(14):1092–1094, July 1997.

[75] Paul E. Schrader, Roger L. Farrow, Dahv A. Kliner, Jean-Philippe Fève, and Nicolas Landru. High-power fiber amplifier with widely tunable repetition rate, fixed pulse duration, and multiple output wavelengths. *Opt. Express*, 14(24):11528–11538, November 2006.

[76] Kai-Hsiu Liao, Aghapi G. Mordovanakis, Bixue Hou, Guoqing Chang, Matthew Rever, Gerard A. Mourou, John Nees, and Almantas Galvanauskas. Generation of hard X-rays using an ultrafast fiber laser system. *Opt. Express*, 15(21):13942–13948, 2007.

[77] Kai-Chung Hou, Simi George, Aghapi G. Mordovanakis, Kazutoshi Takenoshita, John Nees, Bruno Lafontaine, Martin Richardson, and Almantas Galvanauskas. High power fiber laser driver for efficient EUV lithography source with tin-doped water droplet targets. *Opt. Express*, 16(2):965–974, January 2008.

[78] Fabio D. Teodoro, Jeffrey P. Koplow, Sean W. Moore, and Dahv A. Kliner. Diffraction-limited, 300-kW peak-power pulses from a coiled multimode fiber amplifier. *Opt. Lett.*, 27(7):518–520, April 2002.

[79] Christopher Brooks and Fabio Di Teodoro. 1-mJ energy, 1-MW peak-power, 10-W average-power, spectrally narrow, diffraction-limited pulses from a photonic-crystal fiber amplifier. *Opt. Express*, 13(22):8999–9002, October 2005.

[80] Fabio Di Teodoro and Christopher D. Brooks. 1.1 mw peak-power, 7 w average-power, high-spectral-brightness, diffraction-limited pulses from a photonic crystal fiber amplifier. *Opt. Lett.*, 30(20):2694–2696, October 2005.

[81] Fabio Di Teodoro and Christopher D. Brooks. Multistage Yb-doped fiber amplifier generating megawatt peak-power, subnanosecond pulses. *Opt. Lett.*, 30(24):3299–3301, December 2005.

[82] Christopher D. Brooks and Fabio Di Teodoro. Multimegawatt peak-power, single-transverse-mode operation of a 100-μm core diameter, Yb-doped rodlike photonic crystal fiber amplifier. *Appl. Phys. Lett.*, 89(11), 2006.

[83] O. Schmidt, J. Rothhardt, F. Röser, S. Linke, T. Schreiber, K. Rademaker, J. Limpert, S. Ermeneux, P. Yvernault, F. Salin, and A. Tünnermann. Millijoule pulse energy Q-switched short-length fiber laser. *Opt. Lett.*, 32(11):1551–1553, June 2007.

[84] Govind Agrawal. *Nonlinear Fiber Optics, Fourth Edition.* Academic Press, October 2006.

[85] Martin E. Fermann, Almantas Galvanauskas, and Gregg Sucha. *Ultrafast Lasers: Technology and Applications (Optical Engineering).* CRC, October 2002.

[86] Jean-Philippe Fève. Phase-matching and mitigation of four-wave mixing in fibers with positive gain. *Opt. Express*, 15(2):577–582, January 2007.

[87] Jean-Philippe Fève, Paul E. Schrader, Roger L. Farrow, and Dahv A. Kliner. Four-wave mixing in nanosecond pulsed fiber amplifiers. *Opt. Express*, 15(8):4647–4662, April 2007.

[88] R. G. Smith. Optical power handling capacity of low loss optical fibers as determined by stimulated Raman and Brillouin scattering. *Appl. Opt.*, 11(11):2489+, November 1972.

[89] David Milam. Review and assessment of measured values of the nonlinear refractive-index coefficient of fused silica. *Appl. Opt.*, 37(3):546–550, January 1998.

[90] A. Melloni, M. Frasca, A. Garavaglia, A. Tonini, and M. Martinelli. Direct measurement of electrostriction in optical fibers. *Opt. Lett.*, 23(9):691–693, May 1998.

[91] Jesús Subías, Javier Pelayo, Rafael Alonso, Francisco Villuendas, and Carlos Heras. Electrostriction-free n_2 measurement in single-mode optical fibers based on nonlinear-polarization evolution. *J. Opt. Soc. Am. B*, 19(3):390–394, March 2002.

[92] Eric L. Buckland and Robert W. Boyd. Electrostrictive contribution to the intensity-dependent refractive index of optical fibers. *Opt. Lett.*, 21(15):1117+, 1996.

[93] Eric L. Buckland. Mode-profile dependence of the electrostrictive response in fibers. *Opt. Lett.*, 24(13):872–874, July 1999.

[94] Andrea Fellegara and Stefan Wabnitz. Electrostrictive cross-phase modulation of periodic pulse trains in optical fibers. *Opt. Lett.*, 23(17):1357–1359, 1998.

[95] Paul D. Townsend, Alistair J. Poustie, P. J. Hardman, and K. J. Blow. Measurement of the refractive-index modulation generated by electrostriction-induced acoustic waves in optical fibers. *Opt. Lett.*, 21(5):333+, March 1996.

[96] Gadi Fibich and Alexander L. Gaeta. Critical power for self-focusing in bulk media and in hollow waveguides. *Opt. Lett.*, 25(5):335–337, March 2000.

[97] Yaron Silberberg. Collapse of optical pulses. *Opt. Lett.*, 15(22):1282+, November 1990.

[98] Roger L. Farrow, Dahv A. Kliner, Ronald G. Hadley, and Arlee V. Smith. Peak-power limits on fiber amplifiers imposed by self-focusing. *Opt. Lett.*, 31(23):3423–3425, December 2006.

[99] Guoqing Chang, Herbert G. Winful, Almantas Galvanauskas, and Theodore B. Norris. Self-similar parabolic beam generation and propagation. *Phys. Rev. E: Stat. Phys., Plasmas, Fluids,*, 72(1), 2005.

[100] A. E. Siegman. Quasi fast Hankel transform. *Opt. Lett.*, 1(1):13+, July 1977.

[101] G. P. Agrawal and M. Lax. End correction in the quasi-fast hankel transform for optical-propagation problems. *Opt. Lett.*, 6(4):171+, April 1981.

[102] R. Paschotta, R. Paschotta, J. Nilsson, J. Nilsson, and A. C. Tropper. Ytterbium-doped fiber amplifiers. *IEEE J. Quantum Electron.*, 33(7):1049–1056, 1997.

[103] H. Coïc. Analytic modelling of high-gain ytterbium-doped fibre amplifiers. *J. Opt. A: Pure Appl. Opt.*, 4:120–129, March 2002.

[104] K. T. Vu, A. Malinowski, D. J. Richardson, F. Ghiringhelli, L. M. B. Hickey, and M. N. Zervas. Adaptive pulse shape control in a diode-seeded nanosecond fiber MOPA system. *Opt. Express*, 14(23):10996–11001, 2006.

[105] S. Usterer, H. Schwoerer, W. Ziegler, D. Salzmann, and R. Sauerbrey. Effects of a prepulse on laser-induced EUV radiation conversion efficiency. *Appl. Phys. B*, 76(1):17–21, January 2003.

[106] P. Dunne, G. O'Sullivan, and D. O'Reilly. Prepulse-enhanced narrow bandwidth soft x-ray emission from a low debris, subnanosecond, laser plasma source. *Appl. Phys. Lett.*, 76(1):34–36, 2000.

[107] Lee M. Frantz and John S. Nodvik. Theory of pulse propagation in a laser amplifier. *J. Appl. Phys.*, 34(8):2346–2349, 1963.

[108] W. Torruellas, Y. Chen, B. Mcintosh, J. Farroni, K. Tankala, S. Webster, D. Hagan, M. J. Soileau, M. Messerly, and J. Dawson. High peak power ytterbium-doped fiber amplifiers. volume 6102. SPIE, 2006.

[109] John M. Fini. Bend-resistant design of conventional and microstructure fibers with very large mode area. *Opt. Express*, 14(1):69–81, January 2006.

[110] Sachin Joshi, Azer P. Yalin, and Almantas Galvanauskas. Use of hollow core fibers, fiber lasers, and photonic crystal fibers for spark delivery and laser ignition in gases. *Appl. Opt.*, 46(19):4057–4064, July 2007.

[111] Tran X. Phuoc. Laser spark ignition: experimental determination of laser-induced breakdown thresholds of combustion gases. *Opt. Commun.*, 175(4-6):419–423, March 2000.

[112] S. Düsterer, H. Schwoerer, W. Ziegler, C. Ziener, and R. Sauerbrey. Optimization of EUV radiation yield from laser-produced plasma. *Appl. Phys. B*, 73(7):693–698, November 2001.

[113] Takeshi Higashiguchi, Chirag Rajyaguru, Shoichi Kubodera, Wataru Sasaki, Noboru Yugami, Takashi Kikuchi, Shigeo Kawata, and Alex Andreev. Efficient soft x-ray emission source at 13.5 nm by use of a femtosecond-laser-produced Li-based microplasma. *Appl. Phys. Lett.*, 86(23), 2005.

[114] David C. Brandt, Igor V. Fomenkov, Alex I. Ershov, William N. Partlo, David W. Myers, Norbert R. Böwering, Alexander N. Bykanov, Georgiy O. Vaschenko, Oleh V. Khodykin, Jerzy R. Hoffman, Ernesto, Rodney D. Simmons, Juan A. Chavez, and Christopher P. Chrobak. LPP EUV source development for HVM. volume 6517. SPIE, 2007.

[115] Tatsuya Ariga, Hideo Hoshino, and Akira Endo. High average power CO_2 laser MOPA system for tin target LPP EUV light source. volume 6454. SPIE, 2007.

[116] C. Rajyaguru, T. Higashiguchi, M. Koga, K. Kawasaki, M. Hamada, N. Dojyo, W. Sasaki, and S. Kubodera. Parametric optimization of a narrow-band 13.5-nm emission from a Li-based liquid-jet target using dual nano-second laser pulses. *Appl. Phys. B*, 80(4):409–412, April 2005.

[117] B. A. M. Hansson, L. Rymell, M. Berglund, and H. M. Hertz. A liquid-xenon-jet laser-plasma x-ray and EUV source. *Microelectron. Eng.*, 53(1-4):667–670, June 2000.

[118] Takeshi Higashiguchi, Naoto Dojyo, Masaya Hamada, Wataru Sasaki, and Shoichi Kubodera. Low-debris, efficient laser-produced plasma extreme ultraviolet source by use of a regenerative liquid microjet target containing tin dioxide (SnO_2) nanoparticles. *Appl. Phys. Lett.*, 88(20), 2006.

[119] Yoshinori Shimada, Hiroaki Nishimura, Kazuhisa Hashimoto, Michiteru Yamaura, Keisuke Shigemori, Mitsuo Nakai, Shinsuke Fujioka, Shigeaki Uchida, Tomoharu Okuno, Takahiro Hibino, Nobuyoshi Ueda, Ryoji Matsui, Yezheng Tao, Keiji Nagai, Takayoshi Norimatsu, Toru Kawamura, Atsushi Sunahara, Katsunobu Nishihara, Noriaki Miyanaga, Masahiro Nakatsuka, Yasukazu Izawa, and Chihiro Yamanaka. Properties of EUV emissions from laser-produced tin plasmas. volume 5374, pages 912–917. SPIE, 2004.

[120] Y. Shimada, H. Nishimura, M. Nakai, K. Hashimoto, M. Yamaura, Y. Tao, K. Shigemori, T. Okuno, K. Nishihara, T. Kawamura, A. Sunahara, T. Nishikawa, A. Sasaki, K. Nagai, T. Norimatsu, S. Fujioka, S. Uchida, N. Miyanaga, Y. Izawa, and C. Yamanaka. Characterization of extreme ultraviolet emission from laser-produced spherical tin plasma generated with multiple laser beams. *Appl. Phys. Lett.*, 86(5), 2005.

[121] T. Tomie, T. Aota, Y. Kurashima, N. Kandaka, H. Yashiro, K. Nishigori, I. Matsushima, and M. Komuro. Study of a cavity-confined plasma as a debris-less and high conversion efficiency source for EUV lithography. In *Microprocesses and Nanotechnology Conference, 2000 International*, pages 284–285, 2000.

[122] Toshihisa Tomie, Tatsuya Aota, Jing Q. Lin, Yoshifumi Ueno, Hidehiko Yashiro, Noriaki Kandaka, Hiroki Moriwaki, Gohta Niimi, Isao Matsushima, and Kentaro Nishigori. Particle-cluster tin target for a high conversion efficiency LPP source for EUVL. volume 5374, pages 383–393. SPIE, 2004.

[123] C. Rajyaguru, T. Higashiguchi, M. Koga, W. Sasaki, and S. Kubodera. Systematic optimization of the extreme ultraviolet yield from a quasi-mass-limited water-jet target. *Appl. Phys. B*, 79(6):669–672, October 2004.

[124] G. Schriever, S. Mager, A. Naweed, A. Engel, K. Bergmann, and R. Lebert. Laser-produced lithium plasma as a narrow-band extended ultraviolet radiation source for photoelectron spectroscopy. *Appl. Opt.*, 37(7):1243–1248, March 1998.

[125] Henryk Fiedorowicz, Andrzej Bartnik, Miroslaw Szczurek, Hiroyuki Daido, Noriyuki Sakaya, Viliam Kmetik, Yoshiaki Kato, Masayuki Suzuki, Masai Matsumura, Junichi Tajima, Takeyoshi Nakayama, and Thomas Wilhein. Investigation of soft x-ray emission from a gas puff target irradiated with a Nd:YAG laser. *Opt. Commun.*, 163(1-3):103–114, May 1999.

[126] Harry Shields, Steven W. Fornaca, Michael B. Petach, Mark Michaelian, Daniel R. Mcgregor, Richard H. Moyer, and Randall J. St. Pierre. Xenon target performance characteristics for laser-produced plasma EUV sources. volume 4688, pages 94–101. SPIE, 2002.

[127] Gerard D. O'Sullivan and Ronan Faulkner. Tunable narrowband soft x-ray source for projection lithography. *Optical Engineering*, 33(12):3978–3983, 1994.

[128] Feng Jin, Kai Gabel, Martin C. Richardson, Masataka Kado, Andrew F. Vasil'ev, and Daniel Salzmann. Mass-limited laser-plasma cryogenic target for 13-nm point X-ray sources for lithography. volume 2015, pages 151–159. SPIE, 1994.

[129] T. Y. Fan. Laser beam combining for high-power, high-radiance sources. *IEEE J. Sel. Top. Quantum Electron.*, 11(3):567–577, 2005.

[130] Steven J. Augst, Jinendra K. Ranka, T. Y. Fan, and Antonio Sanchez. Beam combining of ytterbium fiber amplifiers (invited). *J. Opt. Soc. Am. B*, 24(8):1707–1715, 2007.

[131] S. J. Augst, A. K. Goyal, R. L. Aggarwal, T. Y. Fan, and A. Sanchez. Wavelength beam combining of ytterbium fiber lasers. *Opt. Lett.*, 28(5):331–333, March 2003.

[132] T. H. Loftus, A. M. Thomas, P. R. Hoffman, M. Norsen, R. Royse, Anping Liu, and E. C. Honea. Spectrally beam-combined fiber lasers for high-average-power applications. *IEEE J. Sel. Top. Quantum Electron.*, 13(3):487–497, 2007.

[133] Thomas H. Loftus, Anping Liu, Paul R. Hoffman, Alison M. Thomas, Marc Norsen, Rob Royse, and Eric Honea. 522 W average power, spectrally beam-combined fiber laser with near-diffraction-limited beam quality. *Opt. Lett.*, 32(4):349–351, February 2007.

[134] Sandro Klingebiel, Fabian Röser, Bülend Orta, Jens Limpert, and Andreas Tünnermann. Spectral beam combining of Yb-doped fiber lasers with high efficiency. *J. Opt. Soc. Am. B*, 24(8):1716–1720, 2007.

[135] Igor V. Ciapurin, Leonid B. Glebov, and Vadim I. Smirnov. Spectral combining of high-power fiber laser beams using bragg grating in PTR glass. volume 5335, pages 116–124. SPIE, 2004.

[136] Steven J. Augst, T. Y. Fan, and Antonio Sanchez. Coherent beam combining and phase noise measurements of ytterbium fiber amplifiers. *Opt. Lett.*, 29(5):474–476, March 2004.

[137] Amiel Ishaaya, Liran Shimshi, Nir Davidson, and Asher Friesem. Coherent addition of spatially incoherent light beams. *Opt. Express*, 12(20):4929–4934, October 2004.

[138] Jesse Anderegg, Stephen Brosnan, Eric Cheung, Paul Epp, Dennis Hammons, Hiroshi Komine, Mark Weber, and Michael Wickham. Coherently coupled high-power fiber arrays. volume 6102. SPIE, 2006.

[139] L. Michaille, C. R. Bennett, D. M. Taylor, T. J. Shepherd, J. Broeng, H. R. Simonsen, and A. Petersson. Phase locking and supermode selection in multicore photonic crystal fiber lasers with a large doped area. *Opt. Lett.*, 30(13):1668–1670, July 2005.

[140] L. Li, A. Schülzgen, S. Chen, V. L. Temyanko, J. V. Moloney, and N. Peyghambarian. Phase locking and in-phase supermode selection in monolithic multicore fiber lasers. *Opt. Lett.*, 31(17):2577–2579, 2006.

[141] Yanming Huo, Peter Cheo, and George King. Fundamental mode operation of a 19-core phase-locked Yb-doped fiber amplifier. *Opt. Express*, 12(25):6230–6239, December 2004.

[142] Arash Mafi and Jerome V. Moloney. Phase locking in a passive multicore photonic crystal fiber. *J. Opt. Soc. Am. B*, 21(5):897–902, May 2004.

[143] E. J. Bochove. Theory of spectral beam combining of fiber lasers. *IEEE J. Quantum Electron.*, 38(5):432–445, 2002.

[144] B. C. Stuart, M. D. Feit, S. Herman, A. M. Rubenchik, B. W. Shore, and M. D. Perry. Nanosecond-to-femtosecond laser-induced breakdown in dielectrics. *Physical Review B*, 53(4):1749+, January 1996.

[145] Karl Hehl, Joerg Bischoff, Ullrich Mohaupt, Martin Palme, Bernd Schnabel, Lutz Wenke, Ragnar Bödefeld, Wolfgang Theobald, Eberhard Welsch, Roland Sauerbrey, and Hartmut Heyer. High-efficiency dielectric reflection gratings: Design, fabrication, and analysis. *Appl. Opt.*, 38(30):6257–6271, October 1999.

[146] Frederico Canova, Raphael Clady, Jean-Paul Chambaret, Manuel Flury, Svtelen Tonchev, Renate Fechner, and Olivier Parriaux. High-efficiency, broad band, high-damage threshold high-index gratings for femtosecond pulse compression. *Opt. Express*, 15(23):15324–15334, November 2007.

[147] A. F. Stewart, Samuel M. Lu, Mohammad M. Tehrani, and C. Volk. Ion beam sputtering of optical coatings. volume 2114, pages 662–677. SPIE, 1994.

[148] F. He, J. H. Price, K. T. Vu, A. Malinowski, J. K. Sahu, and D. J. Richardson. Optimisation of cascaded Yb fiber amplifier chains using numerical-modelling. *Opt. Express*, 14(26):12846–12858, December 2006.